



The FMOS-COSMOS Survey of Star-forming Galaxies at $z \sim 1.6$. VI. Redshift and Emission-line Catalog and Basic Properties of Star-forming Galaxies

Daichi Kashino¹ , John D. Silverman² , David Sanders³ , Jeyhan Kartaltepe⁴ , Emanuele Daddi⁵ , Alvio Renzini⁶ , Giulia Rodighiero⁷ , Annagrazia Puglisi^{5,6} , Francesco Valentino⁸ , Stéphanie Juneau⁹ , Nobuo Arimoto¹⁰, Tohru Nagao¹¹ ,

Olivier Ilbert¹² , Olivier Le Fèvre¹² , and Anton M. Koekemoer¹³

¹ Department of Physics, ETH Zürich, Wolfgang-Pauli-Strasse 27, CH-8093, Zürich, Switzerland; kashinod@phys.ethz.ch

² Kavli Institute for the Physics and Mathematics of the Universe, The University of Tokyo, Kashiwanoha, Kashiwa, Chiba 277-8583, (Kavli IPMU, WPI), Japan

³ Institute for Astronomy, University of Hawaii, 2680 Woodlawn Drive, Honolulu, HI 96822, USA

⁴ School of Physics and Astronomy, Rochester Institute of Technology, 84 Lomb Memorial Drive, Rochester, NY 14623, USA

⁵ Laboratoire AIM-Paris-Saclay, CEA/DSM-CNRS-Université Paris Diderot, Irfu/Service d'Astrophysique, CEA-Saclay, Service d'Astrophysique, F-91191 Gif-sur-Yvette, France

⁶ INAF Osservatorio Astronomico di Padova, vicolo dell'Osservatorio 5, I-35122 Padova, Italy

⁷ Dipartimento di Fisica e Astronomia, Università di Padova, vicolo dell'Osservatorio, 2, I-35122 Padova, Italy

⁸ Dark Cosmology Centre, Niels Bohr Institute, University of Copenhagen, Juliane Maries Vej 30, DK-2100 Copenhagen, Denmark

⁹ National Optical Astronomy Observatory, 950 North Cherry Avenue, Tucson, AZ 85719, USA

¹⁰ Astronomy Program, Department of Physics and Astronomy, Seoul National University, 599 Gwanak-ro, Gwanaku-gu, Seoul 151-742, Republic of Korea

¹¹ Graduate School of Science and Engineering, Ehime University, 2-5 Bunkyo-cho, Matsuyama 790-8577, Japan

¹² Aix Marseille Université, CNRS, LAM—Laboratoire d'Astrophysique de Marseille, 38 rue F. Joliot-Curie, F-13388 Marseille, France

¹³ Space Telescope Science Institute, 3700 San Martin Drive, Baltimore, MD 21218, USA

Received 2018 November 21; revised 2019 January 25; accepted 2019 February 11; published 2019 March 14

Abstract

We present a new data release from the Fiber Multi-Object Spectrograph (FMOS)-COSMOS survey that contains the measurements of the spectroscopic redshift and flux of rest-frame optical emission lines ($H\alpha$, [N II], [S II], $H\beta$, [O III]) for 1931 galaxies out of a total of 5484 objects observed over the 1.7 deg^2 COSMOS field. We obtained H - and J -band medium-resolution ($R \sim 3000$) spectra with FMOS mounted on the Subaru telescope, which offers an in-fiber line flux sensitivity limit of $\sim 1 \times 10^{-17} \text{ erg s}^{-1} \text{ cm}^{-2}$ for an on-source exposure time of 5 hr. The full sample contains the main population of star-forming galaxies at $z \sim 1.6$ over the stellar mass range $10^{9.5} \lesssim M_*/M_\odot \lesssim 10^{11.5}$, as well as other subsamples of infrared-luminous galaxies detected by *Spitzer* and *Herschel* at the same and lower ($z \sim 0.9$) redshifts and X-ray-emitting galaxies detected by *Chandra*. This paper presents an overview of our spectral analyses, a description of the sample characteristics, and a summary of the basic properties of emission-line galaxies. We use the larger sample to redefine the stellar mass–star formation rate relation based on the dust-corrected $H\alpha$ luminosity and find that the individual galaxies are better fit with a parameterization including a bending feature at $M_* \approx 10^{10.2} M_\odot$, and that the intrinsic scatter increases with M_* from 0.19 to 0.37 dex. We also confirm with higher confidence that the massive ($M_* \gtrsim 10^{10.5} M_\odot$) galaxies are chemically mature as much as local galaxies with the same stellar masses, and that the massive galaxies have lower [S II]/ $H\alpha$ ratios for their [O III]/ $H\beta$ as compared to local galaxies, which is indicative of enhancement in the ionization parameter.

Key words: catalogs – galaxies: evolution – galaxies: ISM

1. Introduction

Over the last decade, numerous rest-frame optical spectral data of galaxies at $1 \lesssim z \lesssim 3$ have been delivered by near-infrared spectrographs installed on 8–10 m class telescopes (e.g., Steidel et al. 2014; Kriek et al. 2015; Wisnioski et al. 2015; Harrison et al. 2016). These data sets have revolutionized our understanding of the formation and evolution of galaxies across the so-called “cosmic noon” epoch that marks the peak and the subsequent transition to the declining phase of cosmic star formation history (SFH). Before the data flood by such large near-infrared surveys, however, the relatively narrow redshift range of $1.4 < z < 1.7$ had long been dubbed the “redshift desert,” since all strong spectral features in the rest-frame optical, such as $H\alpha$, [O III], $H\beta$, and [O II], are redshifted into the infrared, while strong rest-frame UV features, such as C IV and S II absorption lines, the Lyman break, and the $\text{Ly}\alpha$ emission line, are still too blue; thus, both are out of reach of conventional optical spectrographs. This redshift interval had thus remained as the last gap to be explored by dedicated

spectroscopic surveys, even after recent deep optical spectroscopic surveys such as the VIMOS Ultra-Deep Survey (VUDS; see Figure 13 of Le Fèvre et al. 2015).

To fill in this redshift gap, we have carried out a large spectroscopic campaign, the FMOS-COSMOS survey,¹⁴ first in low-resolution mode ($R \sim 600$) over 2010 November–2012 February and then in high-resolution (HR) mode ($R \sim 3000$) over 2012 March–2016 April. The Fiber Multi-Object Spectrograph (FMOS) is a near-infrared instrument mounted on the Subaru telescope and uniquely characterized by its wide field of view (FoV; $30'$ in diameter) and high multiplicity (400 fibers), making it one of the ideal instruments to conduct a large spectroscopic survey to detect the rest-frame optical emission lines (e.g., $H\beta$, [O III], $H\alpha$, [N II], [S II]) at the redshift desert. We refer the reader to Silverman et al. (2015b) for the HR survey design and some early results and J. Kartaltepe et al. (2019, in preparation) for the details of the low-resolution survey. Spectral data sets obtained through the early runs of the

¹⁴ <http://member.ipmu.jp/fmos-cosmos/FMOS-COSMOS.html>

FMOS-COSMOS survey have allowed us to investigate various aspects of star-forming galaxies in the $1.43 \leq z \leq 1.74$ redshift range, including their dust extinction and the evolution of a so-called main sequence of star-forming galaxies (Kashino et al. 2013; Rodighiero et al. 2014); the evolution of the gas-phase metallicity and the stellar mass–metallicity relation (Zahid et al. 2014b; Kashino et al. 2017b); the excitation and ionization conditions of main-sequence galaxies (Kashino et al. 2017b); the properties of far-IR-luminous galaxies (Kartalpepe et al. 2015), heavily dust-obscured starburst galaxies (Puglisi et al. 2017), and Type I active galactic nuclei (AGNs; Matsuoka et al. 2013; Schulze et al. 2018); the spatial clustering of host dark matter halos (Kashino et al. 2017a); and the number counts of $H\alpha$ -emitting galaxies (Valentino et al. 2017). Complementary efforts for the follow-up measurement of the $[O\ II] \lambda\lambda 3726, 3729$ emission lines with Keck/DEIMOS have constrained the electron density (Kaasinen et al. 2017) and ionization parameter (Kaasinen et al. 2018) for a subset of the FMOS-COSMOS galaxies. Furthermore, HR molecular-line intensity and kinematic mapping have been obtained with ALMA for an FMOS sample of starburst galaxies, which have revealed their high efficiency of converting gas into stars (Silverman et al. 2015a, 2018b). Our ALMA follow-up observations also discovered a very unique system, where a pair of two galaxies are colliding, and revealed their high gas mass and highly enhanced star formation efficiency (Silverman et al. 2018a).

In this paper, we present the final catalog of the full sample from the FMOS HR observations over the COSMOS field, which includes measurements of spectroscopic redshifts and fluxes of strong emission lines. This catalog includes observations done after 2014 February that were not reported in our previous papers. Based on the latest catalog, we present the basic characteristics of emission-line galaxies, evaluate the possible biases of the FMOS sample with an $H\alpha$ detection, and, with substantially improved statistics, revisit the properties of star-forming galaxies at $z \sim 1.6$, including dust extinction, the stellar mass–star formation rate (SFR) relation, and the properties of the interstellar medium (ISM) using the emission-line diagnostics.

The paper is organized as follows. In Sections 2 and 3, we give an overview of the survey and galaxy samples in the FMOS-COSMOS survey. In Section 4, we describe spectral analyses, emission-line flux measurements, flux calibration, and aperture correction. In Section 5, we summarize the detections of the emission lines and spectroscopic redshift measurements. In Sections 6 and 7, we present the basic measurements of the emission lines and assess the quality of the redshift and flux measurements. In Section 8, we reevaluate the characteristics of our FMOS sample relative to the current COSMOS photometric catalog (COSMOS2015; Laigle et al. 2016). In Section 9, we describe our spectral energy distribution (SED) fitting procedure for the stellar mass estimation and derive SFRs from the rest-frame UV emission and observed $H\alpha$ fluxes, with correction for dust extinction. In Section 10, we measure the relation between stellar mass and SFR at $z \sim 1.6$ and discuss the behavior and intrinsic scatter of the relation. In Section 11, we revisit the ionization and excitation conditions of the ionized nebulae by using key emission-line ratio diagnostics and redefine the $M_{*}-[N\ II]/H\alpha$ relation. In Section 12, we compare the $H\alpha$ - and $[O\ III]$ -emitter samples and discuss possible biases induced by the use of the

Table 1
Summary of Subaru/FMOS HR Observations (2012 March–2014 February)

Date (Local Time)	Program ID	Pointing	Mode	Total Exp. Time (hr)
2012 Mar 12	UH-B3	HR4	<i>H</i> -long	5
2012 Mar 13	S12A-096	HR1	<i>H</i> -long	5
2012 Mar 14	S12A-096	HR2	<i>H</i> -long	4.5
2012 Mar 15	S12A-096	HR1	<i>H</i> -long	5
2012 Mar 16	S12A-096	HR3	<i>H</i> -long	4
2012 Mar 17	S12A-096	HR1	<i>H</i> -short	4
2012 Mar 18	UH-B5	HR1	<i>J</i> -long	4.5
2012 Dec 28	UH-18A	HR2	<i>J</i> -long	3.5
2013 Jan 18	S12B-045I	HR3	<i>H</i> -long	3
2013 Jan 19	S12B-045I	HR4	<i>H</i> -long	3.5
2013 Jan 20	UH-18A	HR3	<i>J</i> -long	4.5
2013 Jan 21	UH-18A	HR4	<i>J</i> -long	3.5
2013 Dec 28	S12B-045I	HR2	<i>H</i> -long	4.25
2014 Jan 21	UH-11A	EXT1	<i>H</i> -long	2.25
2014 Jan 23	UH-11A	EXT2	<i>H</i> -long	2
2014 Jan 24	S12B-045I	HR3	<i>H</i> -long	1.5
2014 Jan 25	S12B-045I	HR1	<i>H</i> -long	5.25
2014 Jan 26	S12B-045I	HR4	<i>H</i> -long	5
2014 Feb 7	S12B-045I	HR1	<i>J</i> -long	4.5
2014 Feb 8 ^a	S12B-045I	HR4	<i>J</i> -long	5.5
2014 Feb 9 ^a	S12B-045I	HR4	<i>J</i> -long	5
2014 Feb 10	UH-38A	EXT3	<i>H</i> -long	5.5

Note.

^a These two *J*-long observations were conducted with the same fiber allocation design (i.e., the same galaxies were observed in total 10.5 hr in the two nights).

$[O\ III]$ line as a galaxy tracer. We give a summary of this paper in Section 13. This paper and the catalog use a standard flat cosmology ($h = 0.7$, $\Omega_{\Lambda} = 0.7$, $\Omega_{M} = 0.3$), AB magnitudes, and a Chabrier (2003) initial mass function (IMF).

2. The FMOS-COSMOS Observations

Here we present a summary of our FMOS observing runs in the HR mode. The HR mode offers five spectral bands, namely, *J*-short/-long and *H*-short/-short-prime/-long. It is stated in Silverman et al. (2015b) that the FMOS spectrographs have four HR gratings, one for each of four HR modes of *J*-short/long and *H*-short/long. We note that this is not fully accurate, and in fact, the spectrographs each contain a single reflective grating, and the spectral window is selected by changing the position of the camera. Our program mainly employed the *J*-long and *H*-long modes. The survey design, observations, and data analysis have been described in our previous papers (e.g., Silverman et al. 2015b).

Tables 1 and 2 summarize all observing runs in the HR mode from 2012 March to 2016 April, with Table 1 referring to runs that produced the data used in our previous papers and Table 2 listing the observations afterward. Observing runs with a program ID starting with “S” were conducted within the Subaru Japan time (PI: John Silverman), while runs with a program ID with “UH” were carried out through the time slots allocated to the University of Hawaii (PI: David Sanders). Although the intended exposure time was 5 hr for all runs, in some runs, it was reduced due to the observing conditions. We also note that observations from 2014 December to 2015 April were conducted using only a single FMOS spectrograph (IRS1) due to an instrumental problem with the second spectrograph (IRS2); thus,

Table 2
Summary of Subaru/FMOS HR observations (2014 March–2016 April)

Date (Local Time)	Program ID	Pointing	Mode	Total Exp. Time (hr)
2014 Mar 6	UH-38A	EXT1	<i>J</i> -long	5.5
2014 Dec 2 ^a	UH-25A	HR4E	<i>H</i> -long	2.25
2015 Feb 8 ^a	S15A-134I	HR7	<i>H</i> -long	4.5
2015 Feb 11 ^a	UH-22A	HR7	<i>H</i> -long	5
2015 Feb 12 ^a	UH-22A	HR6	<i>H</i> -long	3.5
2015 Apr 10 ^a	UH-22A	HR5	<i>H</i> -long	4
2015 Apr 11 ^a	UH-22A	HR5	<i>H</i> -long	1.5
2016 Jan 15	S15A-134I	HR8E	<i>H</i> -long	4.5
2016 Jan 16	S15A-134I	HR4E	<i>H</i> -long	4.5
2016 Jan 17	S15A-134I	HR1E	<i>H</i> -long	4.5
2016 Jan 18	UH-24A	HRC0	<i>H</i> -long	5
2016 Jan 19	UH-24A	HR6	<i>H</i> -long	5
2016 Jan 20	UH-24A	HR7	<i>J</i> -long	5
2016 Mar 24	UH-11A	HR1	<i>J</i> -long	3.5
2016 Mar 26	S16A-054I	HR2	<i>J</i> -long	4.5
2016 Mar 27	S16A-054I	HR4	<i>J</i> -long	4.5
2016 Mar 29	S16A-054I	HR3	<i>J</i> -long	4
2016 Mar 30	S16A-054I	HR7E	<i>H</i> -long	4
2016 Apr 19	UH-11A	HR1E	<i>J</i> -long	3.25
2016 Apr 20	UH-11A	HR6E	<i>J</i> -long	3.5
2016 Apr 21– first half	S16A-054I	HR1	<i>J</i> -long	3.5 (3.0 in IRS2)
2016 Apr 22– first half	S16A-054I	HR3	<i>J</i> -long	3.5
2016 Apr 23– first half	S16A-054I	HR2	<i>J</i> -long	3.25
2016 Apr 24– first half	S16A-054I	HR8E	<i>J</i> -long	3

Notes.

^a Observations from 2014 December to 2015 April were conducted using only a single spectrograph, IRS1.

the number of targets per run was correspondingly reduced by half, while in all other runs, ~ 200 targets were observed simultaneously using the two spectrographs with the cross-beam switching mode, in which two fibers are allocated for a single target.

Figure 1 shows the complete FMOS-COSMOS pawprint over the *Hubble Space Telescope* (*HST*) Advanced Camera for Surveys (ACS) mosaic image in the COSMOS field (upper panel; Koekemoer et al. 2007; Massey et al. 2010) and with the individual objects in the FMOS-COSMOS catalog (lower panel). Each circle with a radius of $16''.5$ corresponds to the FMOS FoV, and their positions are reported in Table 3. The *H*-long spectroscopy has been conducted one or more times at all positions, while the *J*-long observations have been conducted only at eight out of 13 positions due to the reduction of the observing time for bad weather or instrumental troubles. These eight FoVs are highlighted in the lower panel of Figure 1. As clearly shown in the lower panel, the sampling rate is not uniform across the whole survey area due to the difference in the number of pointings and the presence of overlapping regions. In particular, the central area covered by four FoVs (HR1, HR2, HR3, and HR4) has a higher sampling rate with a larger number of repeat pointings relative to the outer region. The full FMOS-COSMOS area is 1.70 deg^2 , and the central area covered by the four FoVs is 0.81 deg^2 .

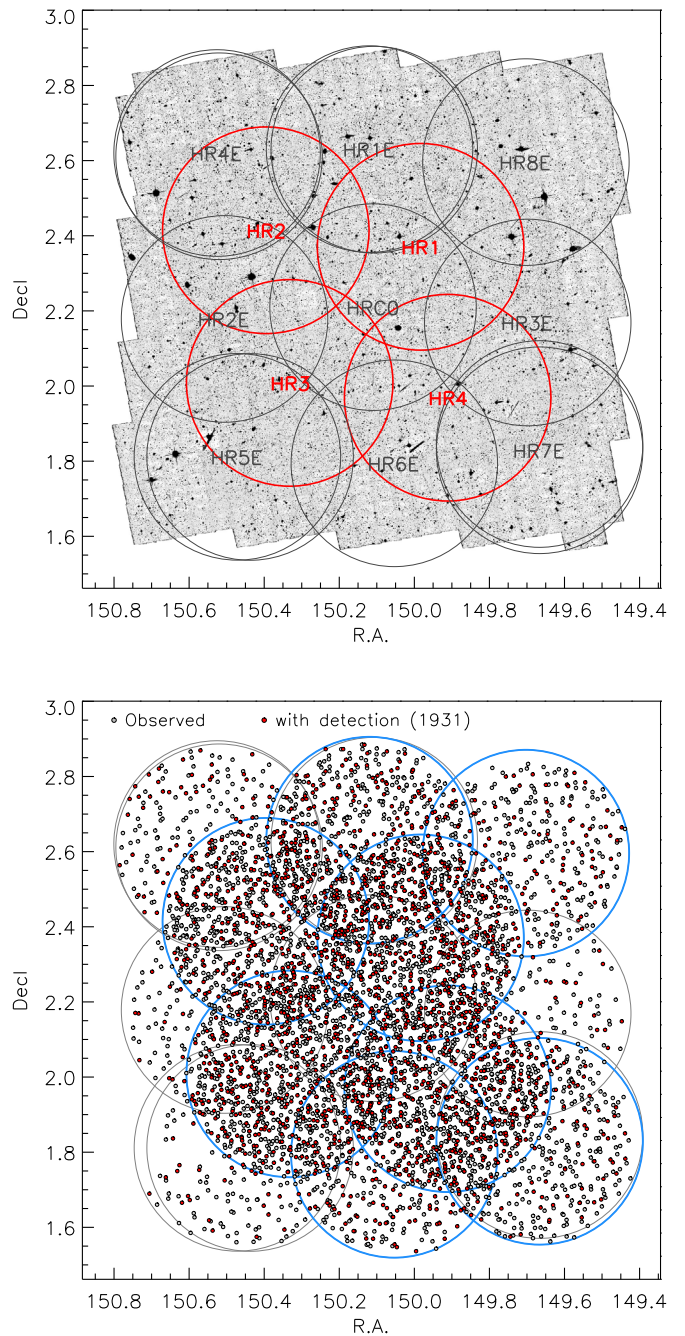


Figure 1. Upper panel: FMOS pawprint overlaid on the *HST*/ACS mosaic of the COSMOS field (Koekemoer et al. 2007; Massey et al. 2010). Large circles show the FoV of each FMOS pointing. The central area of 0.81 deg^2 covered by four FoVs (HR1–HR4) are highlighted by red. Lower panel: on-sky distribution of all galaxies in the FMOS-COSMOS catalog (gray circles). Red circles indicate those with any spectroscopic redshift measurement (1931 objects with $z_{\text{Flag}} \geq 1$; see Section 5). The pawprints visited in the *J*-long mode are highlighted by thick blue circles.

3. Galaxies in the FMOS-COSMOS Catalog

3.1. Star-forming Galaxies at $z \sim 1.6$

Our main galaxy sample is based on the COSMOS photometric catalogs (Capak et al. 2007; Ilbert et al. 2010, 2013; McCracken et al. 2010, 2012) that include the UltraVISTA/VIRCam photometry. For observations after February 2015, we used the updated photometric catalog from Ilbert et al. (2015). For each galaxy in these catalogs, the global properties, such as photometric

Table 3
Location of the FMOS Pawprints

Name	R.A. (J2000)	Decl. (J2000)	N_{visits} H -long	N_{visits} J -long
HR1	09:59:56.0	+02:22:14	3 (+1) ^a	4
HR2	10:01:35.0	+02:24:52	2	3
HR3	10:01:19.7	+02:00:29	3	3
HR4	09:59:38.7	+01:58:08	3	3 ^b
HR1E	10:00:28.6	+02:37:49	1	1
HR2E	10:02:01.4	+02:10:42	1	0
HR3E	09:58:48.2	+02:10:21	1	0
HR4E	10:02:06.1	+02:37:12	2 ^c	0
HR5E	10:01:51.1	+01:48:41	2 ^c	0
HR6E	10:00:12.8	+01:47:39	2 ^c	1
HR7E	09:58:28.6	+01:49:24	3 ^c	1
HR8E	09:58:38.1	+02:35:45	1	1
HRC0	10:00:26.4	+02:12:36	1	0
Full area ^d	1.70 deg ²			
HR1-4 ^e	0.81 deg ²			

Notes.

^a Here “+1” denotes an additional H -short observation.

^b Two of the three J -long observations in HR4 were conducted with the same fiber allocation (i.e., observed the same galaxies in total 10.5 hr in two nights; see Table 1).

^c Observations from 2014 December to 2015 April were conducted with only a single spectrograph, IRS1 (see Table 2).

^d Area of the full FMOS-COSMOS survey field.

^e Area covered by the central four FMOS pawprints (HR1–HR4).

redshift, stellar mass, SFR, and level of extinction, are estimated from SED fits to the broad- and intermediate-band photometry using LePhare (Arnouts et al. 2002; Ilbert et al. 2006). We refer the reader to Ilbert et al. (2010, 2013, 2015) for further details. For the target selection, we computed the predicted flux of the $H\alpha$ emission line from the intrinsic SFR and extinction estimated from our own SED fitting adopting a constant SFH (see Silverman et al. 2015b).

For the FMOS H -long spectroscopy, we preferentially selected galaxies that satisfy the criteria listed below.

1. $K_S \leq 23.5$, a magnitude limit on the UltraVISTA K_S -band photometry (auto magnitude).
2. $1.46 \leq z_{\text{phot}} \leq 1.72$, a range for which $H\alpha$ falls within the FMOS H -long spectral window.
3. $M_* \geq 10^{9.77} M_\odot$ (for a Chabrier IMF)
4. Predicted total (not in-fiber) $H\alpha$ flux $F_{H\alpha}^{\text{pred}} \geq 1 \times 10^{-16} \text{ erg s}^{-1} \text{ cm}^{-2}$.

We refer to those satisfying all of the above criteria as *Primary* objects. From the COSMOS photometric catalog, 3876 objects are identified as meeting the above criteria (the *Primary-parent* sample), and 1582 objects were observed in the H -long mode (the *Primary-HL* sample).

Figure 2 shows the SFR as a function of M_* for the *Primary-parent* sample (red contours) and the *Primary-HL* sample (blue circles). The observed objects trace the so-called main sequence (e.g., Noeske et al. 2007) of star-forming galaxies over two orders of magnitude in stellar mass. However, the limit on the predicted $H\alpha$ flux removed a substantial fraction (60%) of potential targets selected only with the K_S and M_* criteria (shown by black dashed contours). In Figure 2, we indicate median SFRs in bins of M_* separately for the parent

galaxies limited with and without the limit on the predicted $H\alpha$ flux. It is shown that the limit on $F_{H\alpha}^{\text{pred}}$ results in the observed sample being biased ~ 0.2 dex higher in the average SFR at all stellar masses. We found that the *Primary-HL* sample includes 70 objects detected by *Chandra* X-ray observations (see Section 3.3) by checking counterparts. These X-ray-detected objects are excluded for studies of the properties of a pure star-forming population.

In addition to the *Primary* sample, the FMOS-COSMOS catalog contains a substantial number of star-forming galaxies at $z \sim 1.6$ not satisfying all of the criteria described above. This is because the criteria were loosened down to $M_* \geq 10^{9.57} M_\odot$ and/or $F_{H\alpha}^{\text{pred}} \geq 4 \times 10^{-17} \text{ erg s}^{-1} \text{ cm}^{-2}$ for a part of the runs, and we also allocated a substantial number of fibers through the program to those at $z \sim 1.6$ identified in the photometric catalog but not satisfying all of the criteria for the *Primary* objects. We refer to these objects observed in the H -long mode as the *Secondary-HL* sample, which contains 1242 objects. In Figure 3, we show the distributions of galaxy properties for both the *Primary-HL* and the *Primary+Secondary-HL* objects. The *Secondary-HL* sample includes objects with lower or higher z_{phot} and/or lower M_* outside the limits, while the majority are those with $F_{H\alpha}^{\text{pred}}$ lower than the threshold.

In Figure 4, we show the *Primary-HL* and *Secondary-HL* objects in the $(B - z)$ versus $(z - K)$ diagram. These colors are based on the photometric measurements (Subaru B and z^{++} and UltraVISTA K_S) given in the COSMOS2015 catalog (Laigle et al. 2016). It is demonstrated that the majority (95%) of the *Primary+Secondary-HL* sample match the so-called *sBzK* selection (Daddi et al. 2004).

3.2. Far-IR Sources from the Herschel-PACS Evolutionary Probe Survey

Herschel-PACS observations cover the COSMOS field at 100 and 160 μm down to 5σ detection limits of ~ 8 and ~ 17 mJy, respectively (Lutz et al. 2011). These limits correspond to an SFR of roughly $100 M_\odot \text{ yr}^{-1}$ at $z \sim 1.6$. We allocated fibers to these far-IR-luminous objects for particular studies of starburst and dust-rich galaxies (e.g., Kartaltepe et al. 2015; Puglisi et al. 2017) also in view of their follow-up with ALMA (Silverman et al. 2015a, 2018a, 2018b). The objects were selected by cross-matching between the *Herschel*-PACS Evolutionary Probe (PEP) survey catalog and the IRAC-selected catalog of Ilbert et al. (2010), and their stellar mass and SFR are derived from SED fits (further detailed in Rodighiero et al. 2011). For these objects, a higher priority with respect to fiber allocation had to be made, since these objects are rare and would not be sufficiently targeted otherwise.

Our parent sample of the PACS sources contains 231 objects in the range $1.44 \leq z_{\text{phot}} \leq 1.72$, and 116 objects were selected for FMOS H -long spectroscopy. We refer to these objects as the PACS-HL sample. Figure 2 shows the distribution of the *Herschel*-PACS sample in the M_* -versus-SFR plot. It is shown that these objects are limited to be above an SFR of $\sim 100 M_\odot \text{ yr}^{-1}$. Further analyses of this subsample are presented in companion papers (Puglisi et al. 2017; J. Kartaltepe et al. 2019, in preparation).

3.3. Chandra X-Ray Sources

We have dedicated a fraction of FMOS fibers to obtaining spectra for optical/near-infrared counterparts to X-ray sources

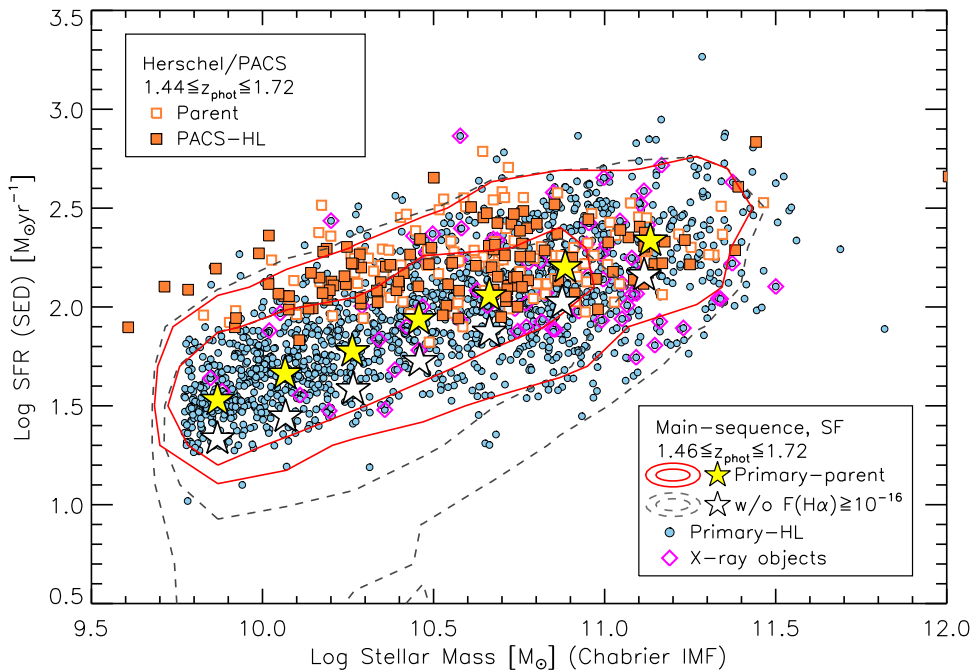


Figure 2. The M_* vs. SFR (from SED fits) for the target samples at $z \sim 1.6$ in the FMOS-COSMOS survey. Red solid and black dashed contours show the distribution (containing 68% and 90%) of the parent galaxies limited with (i.e., Primary-parent sample) and without the threshold $F_{\text{H}\alpha}^{\text{pred}} \geq 1 \times 10^{-16} \text{ erg s}^{-1} \text{ cm}^{-2}$. Correspondingly, yellow and white stars indicate the median SFRs in bins of M_* , respectively, for the parent galaxies with and without the limit on the predicted H α flux. Objects in the Primary-HL sample are indicated by blue circles, with X-ray-detected objects marked by magenta diamonds. Orange open and filled squares indicate the PACS-parent and PACS-HL samples (Section 3.2).

from the *Chandra* COSMOS Legacy survey (Elvis et al. 2009; Civano et al. 2016). The FMOS-COSMOS catalog includes 84 X-ray-selected objects intentionally targeted as compulsory. However, there are many X-ray sources other than those that have been targeted as star-forming galaxies (i.e., the Primary/Secondary-HL sample) or infrared galaxies. We thus performed position matching between the full FMOS-COSMOS catalog and the full *Chandra* COSMOS Legacy catalog.¹⁵ In total, we found an X-ray counterpart for 742 (including the intended 84 objects) of the FMOS extragalactic objects. Most of these X-ray-detected objects are probably AGN-hosting galaxies. These objects are not included in the analyses presented in the rest of this paper, but studies of these X-ray sources are presented in companion papers (Schulze et al. 2018; D. Kashino et al. 2019, in preparation).

3.4. Additional Infrared Galaxies

We also allocated a substantial number of fibers to observing lower-redshift ($0.7 \lesssim z \lesssim 1.1$, where H α falls in the *J*-long window) infrared galaxies selected from S-COSMOS *Spitzer*-MIPS observations (Sanders et al. 2007) and *Herschel*-PACS and SPIRE from the PEP (Lutz et al. 2011) and HerMES (Oliver et al. 2012) surveys, respectively. We used the photometric redshifts of Salvato et al. (2011, for X-ray-detected AGNs) and Ilbert et al. (2015) and for the source selection. We derived the total IR luminosity, calculated from the best-fit IR template using the SED fitting code LePhare and integrating from 8 to 1000 μm . These luminosities are in the range $10^{11} \lesssim L_{\text{IR}}/L_{\odot} \lesssim 10^{12.5}$, spanning the luminosity regime of luminous and ultraluminous infrared galaxies (LIRGs and ULIRGs; see review by Sanders & Mirabel 1996). Our parent

sample includes 1818 objects in the range $0.66 \leq z_{\text{phot}} \leq 1.06$. Of these, we observed 344 in the *J*-long mode. Further analysis of this particular subsample will be presented in a future paper (J. Kartaltepe et al. 2019, in preparation).

4. Flux Measurement and Calibration

4.1. Observed Spectra and Noise

The collected spectral data have been processed with the standard reduction pipeline, FIBRE-pac (Iwamuro et al. 2012), generating one- and two-dimensional (1D and 2D, respectively) spectra for each object. The relevant noise and squared-noise spectra are also provided by the pipeline. The noise level is estimated from the pixel variance between the observed frames. Examples of these spectra are shown in Silverman et al. (2015b; see Figure 10). We first visually inspected all 1D and 2D spectra to search for the presence of the emission lines using the graphical interface SpecPro¹⁶ (Masters & Capak 2011), and then we performed emission-line fitting to the 1D spectra as described in Section 4.2.

The FMOS spectrographs are equipped with a mask mirror to block the light at the wavelengths of bright OH airglow lines to avoid the saturation (Kimura et al. 2010). Thus, the OH mask effectively reduces the spectral coverage. The observed spectra are quite noisy at the wavelengths of the OH mask and unmasked sky lines. Correspondingly, the noise spectra show sudden increases in the noise level at these wavelengths. As described below, these wavelengths are removed for the emission-line fitting and continuum flux measurements (see Figures 11 and 14 of Silverman et al. 2015b).

The amount of wavelength coverage lost by the OH mask and residual sky lines should be taken into account to evaluate

¹⁵ The *Chandra* catalogs are available here: <http://cosmos.astro.caltech.edu/page/xray>.

¹⁶ <http://specpro.caltech.edu>

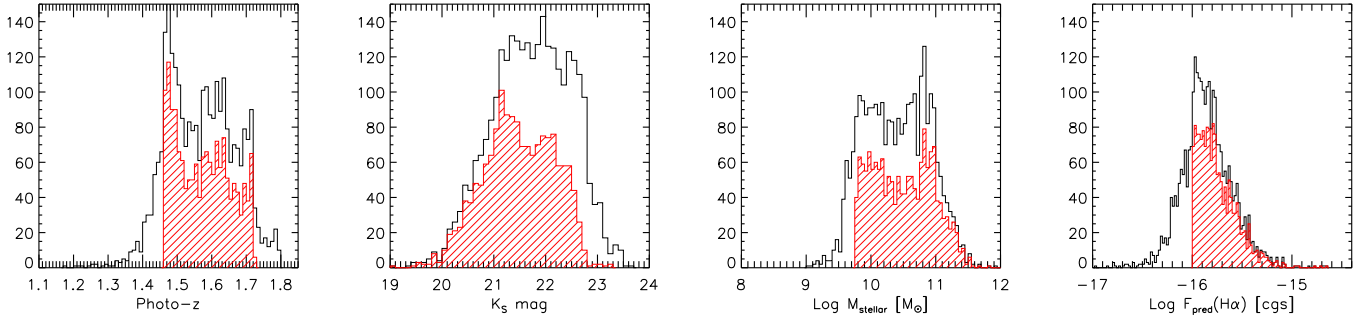


Figure 3. From left to right, distributions of z_{phot} , K_S magnitude, M_* , and predicted $F_{\text{H}\alpha}$ for the Primary-HL (red hatched histograms) and Secondary-HL (plus Primary-HL) sample (black open histograms).

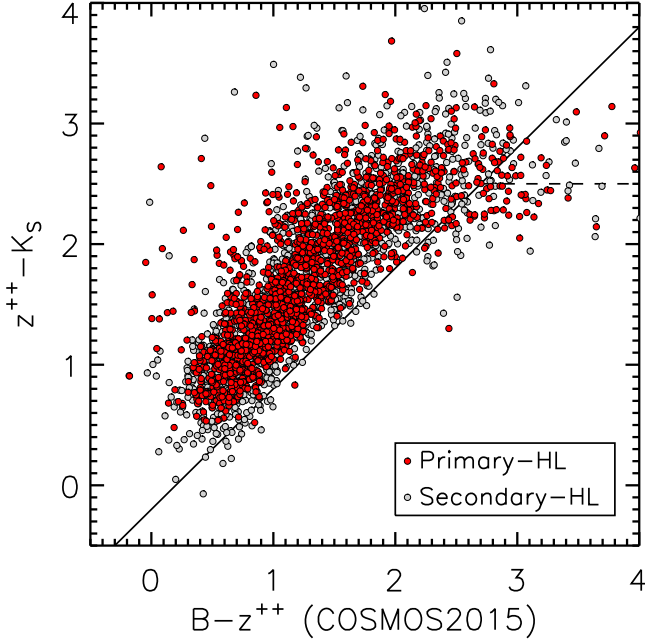


Figure 4. Primary-HL (red circles) and Secondary-HL (gray circles) samples in the BzK diagram. The solid and dashed lines indicate the boundaries for distinguishing $z > 1.4$ star-forming, $z > 1.4$ quiescent, and $z < 1.4$ galaxies, defined by Daddi et al. (2004).

the success rate of the observations (see Section 5.1). To estimate the fraction of the lost coverage, we should keep in mind that the original IRS1 OH mask was replaced with a copy of the mask used in IRS2 in mid-2012. Thus, our first seven runs conducted in 2012 March were carried out with the old mask (see Table 1), while subsequent observations were conducted with the newer one. This change was intended to homogenize the performance between the two spectrographs and reduce the amount of wavelength coverage lost by the rather conservative mask originally implemented in IRS1. Furthermore, for a period of the H -long observations in 2012 March, the OH mask was misaligned in IRS2; thus, some additional pixels at OH-free wavelengths were masked out. This problem was fixed for the latter observations. In the H -long mode, the typical fraction of wavelength coverage lost by the OH mask and residual sky lines is ≈ 0.30 , on average, throughout the project. In 2012 March, however, this fraction was elevated to 0.40 (IRS1) and 0.34 (IRS2) due to using the old mask mirror and the misalignment, respectively. In the J -long mode, the typical lost fraction is ≈ 0.27 , being elevated to 0.35 (only IRS1) in a single run conducted in 2012 March.

4.2. Emission-line Fitting

Our procedure for emission-line fitting makes use of the IDL package MPFIT (Markwardt 2009). Candidate emission lines were modeled with a Gaussian profile after subtracting the continuum. The $\text{H}\alpha$ and $[\text{N II}]$ or $\text{H}\beta$ and $[\text{O III}]$ lines were fit simultaneously while fixing the velocity widths to be the same and allowing no relative offset for the line centroids. The flux ratios of the doublets $[\text{N II}] \lambda 6584/6548$ and $[\text{O III}] \lambda 5007/4959$ were fixed to be 2.96 and 2.98, respectively (Storey & Zeppen 2000).

The spectral data processed with FIBRE-pac are given in units of μJy , which were converted into flux density per unit wavelength, i.e., $\text{erg s}^{-1} \text{cm}^{-2} \text{\AA}^{-1}$, before fitting. The observed flux density $F_{\lambda,i}$, where i denotes the pixel index, was fit with weights defined as the inverse of the squared-noise spectra output by the pipeline. The weights W_i were set to zero for the pixels impacted by the OH mask or sky residuals.

We assessed the quality of the fitting results based on the signal-to-noise ratio (S/N) calculated from the formal errors on the model parameters returned by the MPFITFUN code. We emphasize that these S/Ns do not include the uncertainties on the absolute flux calibration described in later sections. In addition, we have also estimated the fraction of flux lost by bad pixels (i.e., pixels with $W_i = 0$). For all lines, we define the “bad-pixel loss” as the fraction of the contribution occupied by the bad pixels to the total integral of the Gaussian profile,

$$f_{\text{badpix}} = \frac{\sum_{i|W_i=0} P_i}{\sum_i P_i}, \quad (1)$$

where P_i is the flux density of the best-fit Gaussian profile at the i th pixel (not the observed spectrum). We disregard any tentative line detections if $f_{\text{badpix}} > 0.7$.

The goodness of the line fits is given by the reduced χ^2 statistic, χ^2/dof , where dof is the degrees of freedom in the fits. Figure 5 shows the resultant χ^2/dof values as a function of line strength (upper panel) and S/N (lower panel) separately for $\text{H}\alpha + [\text{N II}]$ in H -long and $\text{H}\beta + [\text{O III}]$ in J -long. The distribution of the reduced χ^2 statistics clearly peaks at $\chi^2/\text{dof} \approx 1$, with no significant trends with either line strength or S/N.

In relatively few cases, a prominent broad emission-line component was present, and we included a secondary broad component for $\text{H}\alpha$ or $\text{H}\beta$. Furthermore, we also added a secondary narrow $\text{H}\alpha + [\text{N II}]$ (or $\text{H}\beta + [\text{O III}]$) component with a centroid and width different from the primary component, when necessary (e.g., a case in which there is a prominent blueshifted component of the $[\text{O III}]$ line, possibly attributed to

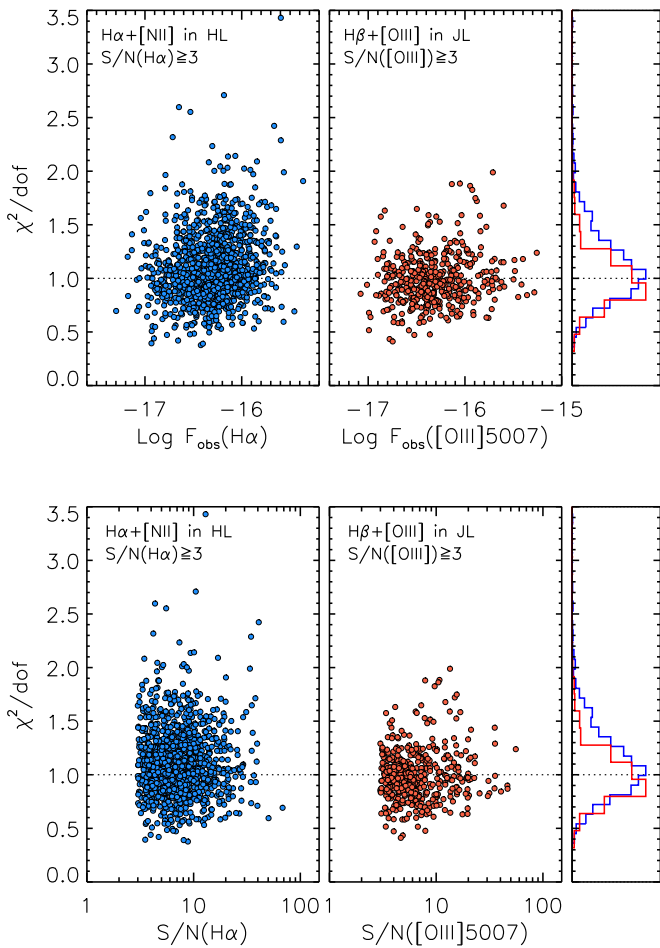


Figure 5. Reduced χ^2 statistic (χ^2/dof) as a function of observed line flux (upper panel) and S/N (lower panel). The left and middle panels show the results of fits to $H\alpha + [N\text{II}]$ in the H -long band and $H\beta + [\text{OIII}]$ in the J -long band, respectively. The right panels show the corresponding normalized distributions of the χ^2/dof values.

an outflow). Such exceptional handling was applied for only 5% of the whole sample (108 out of 1931 objects with a line detection). Most of these objects are X-ray-detected, and we postpone a detailed analysis of these objects to a future paper while focusing here on the basic properties of normal star-forming galaxies.

4.3. Upper Limits

For nondetections of emission lines of interest, we estimate upper limits on their in-fiber fluxes if we have a spectroscopic redshift measurement from any other detected lines in the FMOS spectra and the spectral coverage for undetected lines. The S/N of an emission line depends not only on the flux and the typical noise level of the spectrum but also on the amount of loss due to bad pixels. These effects have been considered on a case-by-case basis by performing dedicated Monte Carlo simulations for each spectrum.

For each object with a measurement of spectroscopic redshift, we created $N_{\text{sim}} = 500$ spectra containing an artificial emission line with a Gaussian profile at a specific observed-frame wavelength of undetected lines based on the spectroscopic redshift. The line width was fixed to a typical FWHM of 300 km s^{-1} (Section 6.1), and Gaussian noise was added to these artificial spectra based on the processed noise spectrum.

In doing so, we mimicked the impact of the OH lines and the masks. We then performed a fitting procedure for these artificial spectra with various amplitudes in the same manner as the data and estimated the 2σ upper limit for each undetected line by linearly fitting the sets of simulated fluxes and the associated S/Ns.

4.4. Integrated Flux Density

In addition to the line fluxes, we also measured the average flux density within the spectral window for individual objects regardless of the presence or absence of a line detection. The average flux density $\langle f_\nu \rangle$ and the associated errors were derived by integrating the extracted 1D spectrum of each galaxy as follows:

$$\langle f_\nu \rangle = \frac{\sum_i f_{\nu,i} W_i R_i}{\sum_i W_i R_i d\lambda}, \quad (2)$$

$$\Delta \langle f_\nu \rangle = \frac{\sqrt{\sum_i (N_{\nu,i} W_i R_i d\lambda)^2}}{\sum_i W_i R_i d\lambda}, \quad (3)$$

where $d\lambda = 1.25 \text{ \AA}$ is the wavelength pixel resolution, N_i is the associated noise spectrum, and R_i is a response curve.

Beside being used to estimate the equivalent widths of detected emission lines, these quantities can also allow for absolute flux calibration by comparing them with the ground-based H - or J -band photometry. For comparison, we use the fixed $3''$ aperture magnitudes $H(J)\text{-MAG_APER3}$ from the UltraVISTA-DR2 survey (McCracken et al. 2012) provided in the COSMOS2015 catalog (Laigle et al. 2016), applying the recommended offset from the aperture to total magnitudes (see the Appendix of Laigle et al. 2016). For comparison with the reference photometry, we define R_i in the above equations based on the response curve of the VISTA/VIRCam H - or J -band filters,¹⁷ and flux densities were then converted to (AB) magnitudes. In the calculation of these equations, we did not exclude the detected emission lines because our primary purpose is to compare these to the ground-based broadband photometry, which, in principle, includes the emission-line flux.¹⁸ We disregard the measurements with $S/N < 5$ and also exclude objects whose A- and/or B-position spectrum (obtained through the ABAB telescope nodding) falls on the detector next to those of flux standard stars, since these spectra may be contaminated by leakage from the neighbor bright star spectrum. Finally, we successfully measured the flux density for 2456 objects observed in the H -long mode and 1700 objects observed in J -long.

In Figure 6, we compare the observed magnitudes H_{AB} from the FMOS H -long spectra with the UltraVISTA H -band magnitudes separately for the two spectrographs (IRS1 and IRS2) of FMOS. Here the observed values were computed from spectra produced by the standard reduction pipeline, and we refer to these as the “raw” magnitude. Data points from a single observing run (2013 December 28) are highlighted for reference. It is clear that there is a global offset of ~ 1 mag in the observed magnitudes relative to the reference UltraVISTA magnitudes. This reflects the loss flux falling outside the fiber

¹⁷ The data for the filter response curves are available here: <http://www.eso.org/sci/facilities/paranal/instruments/vircam/inst.html>.

¹⁸ For estimating the emission-line equivalent widths, we excluded the emission-line components (Section 6.1).

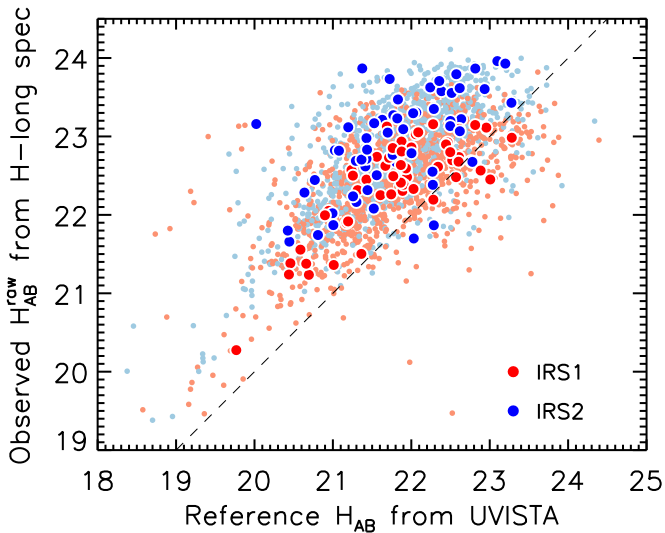


Figure 6. Observed “raw” H_{AB} from the H -long spectra vs. reference H_{AB} from UltraVISTA. Red and blue points correspond to the measurements with the two spectrographs, IRS1 and IRS2, respectively. Data points from a single observing run (2013 December 28) are highlighted with large symbols. A global offset of ~ 1 mag from the one-to-one relation (dashed line) reflects the average aperture loss, while an offset of ~ 0.5 mag between IRS1 (red) and IRS2 (blue) is due to the differential total throughput of these spectrographs.

aperture. In addition, we can also see that an ~ 0.5 mag systematic offset exists between the two spectrographs. This offset is due to the difference in the total efficiency of the two spectrographs. Prior to the aperture correction, we first corrected for this offset between IRS1 and IRS2, as follows:

$$H_{\text{IRS1}} = H_{\text{IRS1}}^{\text{raw}} + (\langle \Delta H_{\text{IRS2}}^{\text{raw}} \rangle - \langle \Delta H_{\text{IRS1}}^{\text{raw}} \rangle) / 2, \quad (4)$$

$$H_{\text{IRS2}} = H_{\text{IRS2}}^{\text{raw}} - (\langle \Delta H_{\text{IRS2}}^{\text{raw}} \rangle - \langle \Delta H_{\text{IRS1}}^{\text{raw}} \rangle) / 2, \quad (5)$$

where $\langle \Delta H_{\text{IRS}i}^{\text{raw}} \rangle$ is the median offset of the observed magnitude relative to the reference magnitude. This correction has been done for each observing run independently. We did the same for the J -band observations as well.

Figure 7 shows the observed magnitudes after correcting for the offset between IRS1 and IRS2. The magnitudes from the H -long (left panel) and J -long (right panel) spectra are shown as a function of S/Ns separately for each spectrograph. The correlations are in good agreement between the two spectrographs and between the spectral windows. The threshold S/N = 5 corresponds to ≈ 23.5 ABmag for both H and J .

We emphasize that in the rest of the paper, as well as in our emission-line catalog, the correction for the differential throughput between the two IRSs is applied for all observed quantities, including emission-line fluxes, formal errors, and upper limits on the line fluxes. Therefore, catalog users do not need to care about this instrumental issue. Meanwhile, the fluxes in the catalog denote the in-fiber values; hence, the aperture correction should be applied using the correction factors given in the catalog, if necessary (see the next subsection for details).

4.5. Aperture Correction

As already mentioned, the emission-line and broadband fluxes measured from observed FMOS spectra arise only from the regions of each target falling within the $1''.2$ diameter aperture of the FMOS fibers. Therefore, it is necessary to correct for flux falling outside the fiber aperture to obtain the

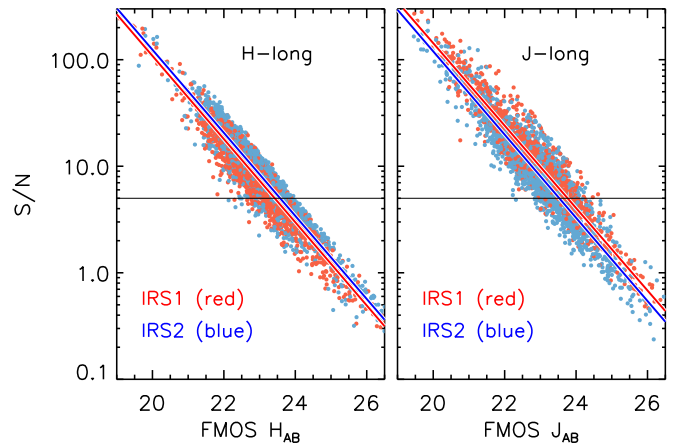


Figure 7. Observed magnitude from the FMOS H -long (left panel) and J -long (right panel) spectra vs. the estimated S/N. The data from IRS1 and IRS2 are shown separately with red and blue, respectively. The solid lines are linear fits to the data, and the horizontal lines indicate the threshold S/N = 5.

total emission-line flux of each galaxy. The amount of aperture loss depends on both the intrinsic size of each galaxy and the conditions of the observation, which include variable seeing size and fluctuations of the fiber positions (typically less than $0''.2$; Kimura et al. 2010). We define three methods for aperture correction.

First, the aperture correction can be determined by simply comparing the observed H (or J) flux density obtained by integrating the FMOS spectra to the reference broadband magnitude for individual objects. This method can be utilized for moderately luminous objects for which we have a good measurement of the integrated flux from the FMOS spectra (observed $H_{AB} \lesssim 22.5$). This method cannot be applied for objects with poor continuum detection and suffering from flux leakage from bright objects.

Second, we can use the average offset of the observed magnitude relative to the reference magnitude for each observing run. This method can be applied to fainter objects and those with insecure continuum measurements (e.g., impacted by leakage from a bright star) for correcting the emission-line fluxes.

Lastly, we determine the aperture correction based on HR imaging data. In the COSMOS field, we can utilize images taken by the HST/ACS (Koekemoer et al. 2007; Massey et al. 2010) that almost entirely cover the FMOS field and offer a high spatial resolution. The advantage of this method is that we can determine the aperture correction object by object, taking into account their size properties and a specific seeing size of the observing night. Hereafter, we describe this third method in detail (see also Kashino et al. 2013; Silverman et al. 2015b).

For each galaxy, the aperture correction is determined from the HST/ACS I_{F814W} -band images (Koekemoer et al. 2007). In doing so, we implicitly assume that the difference between the on-sky spatial distributions of the rest-frame optical continuum (i.e., stellar radiation) and nebular emission is negligible under typical seeing conditions ($\gtrsim 0''.5$ in FWHM). This assumption is reasonable for the majority of the galaxies in our sample, in particular, those at $z > 1$, whose typical size is $< 1''$.

We performed photometry on the ACS images of the FMOS galaxies using SExtractor version 2.19.5 (Bertin & Arnouts 1996). The flux measurement was performed with a fixed aperture size at the positions of the best-matched objects in the

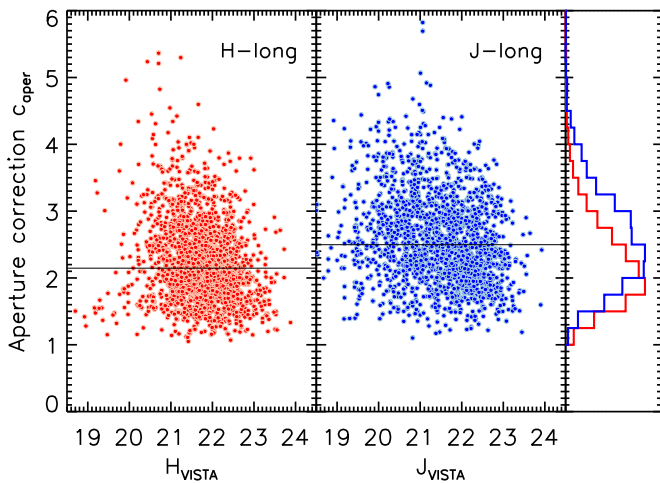


Figure 8. Derived aperture correction factors c_{aper} as a function of the reference H or J magnitudes (Laigle et al. 2016). The horizontal solid lines mark the median values. Histograms show the distribution of c_{aper} separately for the H -long (red) and J -long (blue) bands.

COSMOS2015 catalog, if it exists, otherwise at the position of the fiber pointing. For the majority of the sample, we used the measurements in the $2''$ diameter aperture (FLUX_APER2) but employed the $3''$ aperture (FLUX_APER3) for a small fraction of the sample if the size of the object extends significantly beyond the $2''$ aperture and, consequently, the ratio FLUX_APER3/FLUX_APER2 is $\gtrsim 1.3$ ¹⁹. We visually inspected the ACS images to check for the presence of significant contamination by nearby objects, flagging such cases in the catalog.

Next, we smoothed the ACS images by convolving with a Gaussian point-spread function (PSF) for the effective seeing size. We then performed aperture photometry with SExtractor to measure the flux in the fixed FMOS fiber aperture FLUX_APER_FIB and computed the correction factor as $c_{\text{aper}} = \text{FLUX_APER2}(3) / \text{FLUX_APER_FIB}$. The size of the smoothing Gaussian kernel (i.e., the effective seeing size) was retroactively determined for each observing run to minimize the average offset relative to the reference UltraVISTA broadband magnitudes (McCracken et al. 2012) from Laigle et al. (2016; see Section 4.4). We note that the effective seeing sizes determined are in broad agreement with the actual seeing conditions during the observing runs ($\sim 0''.5$ – $1''.4$ in FWHM) that were measured from the observed PSF of the guide stars. We note that the effective seeing size determined here includes the effect of the positioning errors of the FMOS fibers ($\lesssim 0''.2$). The scatter in the flux measurement caused by fluctuations of the aperture positions of $\sigma = 0''.2$ is ~ 0.03 dex (for an object of an effective radius of $0''.5$ with an effective seeing of $0''.7$). Therefore, the effect of the fiber positioning errors should be negligible in the entire uncertainty of the flux measurements (see below).

Figure 8 shows the derived aperture correction factors as a function of the reference magnitude separately for the H and J bands. We excluded insecure estimates of aperture correction,

¹⁹ In our previous studies (Kashino et al. 2013; Silverman et al. 2015b), the pseudo-total Kron flux FLUX_AUTO was used as the total I_{F814W} -band flux, rather than the fixed aperture flux used in this paper. Although the conclusions are not affected by the choice, the use of the fixed aperture gives better reproducibility of photometry, as the Kron flux measurement is more sensitive to the configuration to execute the SExtractor photometry.

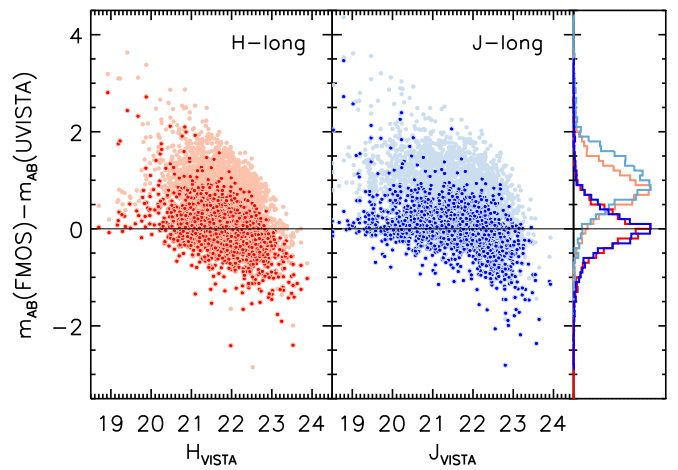


Figure 9. Difference between the observed (FMOS) and reference (UltraVISTA; Laigle et al. 2016) magnitudes for the H and J bands. The pale and bright color points correspond, respectively, to before and after the aperture correction was applied. The histograms show the distribution of the differential magnitudes separately for each band, as well as for before/after the correction.

which includes cases where the blending or contamination from other objects is significant. The aperture correction factors range from ~ 1.2 to ~ 4.5 , and the median values are 2.1 and 2.5 for the H and J bands, respectively. This small offset between the two bands is due to the fact that seeing is worse for shorter wavelengths under the same condition. Note that the formal error on the correction factor that comes from the aperture photometry on the ACS image (e.g., FLUXERR_APER2) is small (typically $< 5\%$), and thus the scatter seen in Figure 8 is real, reflecting both variations in the intrinsic sizes of galaxies and the seeing conditions of observing nights.

Figure 9 shows offsets between the observed and reference magnitudes, before and after correcting for aperture losses, as a function of the reference magnitudes. The average magnitude offset is mitigated by applying the aperture correction. After aperture correction, we found the standard deviation of the magnitude offsets to be 0.42 (0.50) mag, after (before) taking into account the individual measurement errors in both $\langle f_{\nu} \rangle$ of the observed FMOS spectra and the reference magnitude. There is no significant difference between H and J . Note that this comparison also provides a sense of testing agreement between the first method of aperture correction estimation, described above, that relies on the direct comparison between the observed flux density on the FMOS spectra and the reference magnitude.

In the catalog, we provide the best estimate of aperture correction for each of the galaxies, regardless of the presence or absence of a spectroscopic redshift measurement. For 67% of the sample observed in the H -long spectral window and 80% in J -long, the best aperture correction is based on the HST/ACS image described above. However, for the remaining objects, the estimates with this method are not robust due to blending, significant contamination from other sources, or any other troubles on the pixels of the ACS images. Otherwise, there is no ACS coverage for some of those falling outside the area (see Figure 1). For such cases, we provide as the best aperture correction an alternative estimate based on the second method that uses the average offset of all objects observed together in the same night. When applying the aperture correction from this second method for all objects, the agreement between the aperture-corrected observed flux density and the reference

magnitude is slightly worse, with an estimated intrinsic scatter of ≈ 0.57 mag for both H - and J -long, than that based on the ACS image-based aperture correction.

In the following, we use these best estimates of aperture correction without being aware of which method is used. Throughout the paper, when any aperture-corrected values, such as total luminosity and SFRs, are shown, the error includes in quadrature a common factor of 1.5 (or 0.17 dex) in addition to the formal error on the observed emission-line flux to account for the intrinsic uncertainty of aperture correction. Lastly, we emphasize that the aperture correction is determined for all of the individual objects using the independent observations (i.e., *HST*/ACS and UltraVISTA photometry) and just average information of the FMOS observations (i.e., mean offset), but not relying on the individual FMOS measurements. This ensures that the uncertainty of aperture correction is independent of the individual FMOS measurements.

5. Line Detection and Redshift Estimation

The full FMOS-COSMOS catalog contains 5247 extragalactic objects that were observed in any of the H -long, J -long, or H -short bands.²⁰ The majority of the survey was conducted in the H -long mode, collecting spectra of 4052 objects. The second effort was dedicated to observations in the J -long band, including follow-up of objects for which $H\alpha$ was detected in H -long to detect other lines (i.e., $H\beta$ and [O III]) and observations for lower-redshift objects to detect $H\alpha$. A single night was used for observation in the H -short mode (see Table 1). In this section, we report the spectroscopic redshift measurements and success rates.

5.1. Spectroscopic Redshift Measurements

Out of the full sample, we obtained spectroscopic redshift measurements for 1931 objects. The determination of spectroscopic redshift is based on the detection of at least a single emission line, expected to be either $H\alpha$, [N II], $H\beta$, or [O III]. For our initial target selection, galaxies were selected based on the photometric redshift z_{phot} , so $H\alpha$ + [N II] and $H\beta$ + [O III] are expected in either the H -long or J -long spectral window. For the majority of the sample, we identified the detected line as $H\alpha$ or [O III] according to their z_{phot} . However, this is not the case for a small number of objects for which we found a clear combination of $H\alpha$ + [N II] or the [O III] doublet (+ $H\beta$) in a spectral window not expected from the z_{phot} . For objects observed in both the H and J bands, we checked whether their independent redshift measurements were consistent. If not, we reexamined the spectra to search for any features that could solve the discrepancy between the spectral windows. Otherwise, we disregarded line detections of lower S/N. For objects observed two or more times, we adopted a spectrum with the highest S/N of the line flux. For objects with consistent line detections in the two spectral windows (i.e., $H\alpha$ + [N II] in H -long and $H\beta$ + [O III] in J -long), we regarded a redshift estimate based on higher-S/N detection as the best estimate (z_{best}). There are also objects that were observed two or more times in the same spectral window. In particular, the repeat J -long observations have been carried out to build up exposure

²⁰ The full FMOS-COSMOS catalog is available here: <http://member.ipmu.jp/fmos-cosmos/FMOS-COSMOS.html>. Please refer to the README file distributed with the catalog for more information.

Table 4
Summary of the Acquisition of Spectra and Successful Redshift

Spectral Band	Wavelength Range	N_{obs}	$z\text{Flag} =$			
			1	=2	=3	=4
Total	...	5247	140	389	507	895
H -long	1.60–1.80 μm	4052	117	314	384	694
H -short	1.40–1.60 μm	163	3	12	18	34
J -long	1.11–1.35 μm	2599	77	304	388	807
HL+HS	...	108	3	9	13	28
HL+JL	...	1441	54	229	266	607
HS+JL	...	81	1	11	16	33
HL	...	63	1	8	12	28
+HS+JL						

time to detect faint $H\beta$ at higher S/N. In the catalog presented in this paper, however, we adopted a single observation with detections of the highest S/N, instead of stacking spectra taken on different observing runs.²¹

We assign a quality flag ($z\text{Flag}$) to each redshift measurement based on the number of detected lines and the associated S/N as follows (see Section 4.2 for details of the detection criteria).

$z\text{Flag}$ 0: No emission line detected.

$z\text{Flag}$ 1: Presence of a single emission line detected at $1.5 \leq S/N < 3$.

$z\text{Flag}$ 2: One emission line detected at $3 \leq S/N < 5$.

$z\text{Flag}$ 3: One emission line detected at $S/N \geq 5$.

$z\text{Flag}$ 4: One emission line at $S/N \geq 5$ and a second line at $S/N \geq 3$ that confirms the redshift.

The criteria have been slightly modified from those used in Silverman et al. (2015b; where $\text{Flag} = 4$ if a second line is detected at $S/N \geq 1.5$). Note that objects with $z\text{Flag} = 1$ are not used for scientific analyses in the rest of the paper.

In Table 4, we summarize the numbers of observed galaxies and the redshift measurements with the corresponding quality flags. In the second through fourth rows, the numbers of galaxies observed in each spectral band are reported, while the numbers of galaxies observed in two or three bands are reported in the last four rows. Table 5 summarizes the number of galaxies with detections of each of four emission lines.

In the top panel of Figure 10, we display the distribution of all galaxies with a spectroscopic redshift measurement split by the quality flag. There are three redshift ranges, corresponding to possible combinations of the detected emission lines and the spectral ranges, as summarized in Table 5. In the middle panel, we compare the distribution of the FMOS-COSMOS galaxies to the redshift distribution from the VUDS observations (Le Fèvre et al. 2015). It is clear that our FMOS survey constructed a complementary spectroscopic sample that fills the redshift gap seen in the recent deep optical spectroscopic survey. In the bottom panel of Figure 10, we show objects for which $H\alpha$ is detected in the H -long band with the positions of OH airglow lines. The wavelengths of the OH lines are converted into redshifts based on the wavelength of the $H\alpha$ emission line as $z_{\text{OH}} = \lambda_{\text{OH}}/6564.6\text{\AA} - 1$. It is clear that the number of successful detections of $H\alpha$ is suppressed near the bright OH airglow lines, shown by gray stripes. This is because pixels at

²¹ The measurements based on coadded spectra are provided in an ancillary catalog.

Table 5
Summary of the Emission-line Detection

Line	$z_{\min}-z_{\max}$	$1.5 \leq S/N < 3$	$3 \leq S/N < 5$	$S/N \geq 5$
<i>H</i> -long				
H α	1.43–1.74	111	305	909
[N II]	1.43–1.73	298	274	247
H β	2.32–2.59	9	13	14
[O III]	2.21–2.59	5	8	58
<i>H</i> -short				
H α	1.26–1.46	2	1	21
[N II]	1.31–1.46	2	5	6
H β	2.15–2.15	1	0	0
[O III]	2.15–2.15	0	0	1
<i>J</i> -long				
H α	0.70–1.05	13	50	267
[N II]	0.70–1.04	44	74	134
H β	1.31–1.74	139	160	100
[O III]	1.30–1.69	49	160	296

these wavelengths are lost due to high noise caused by the OH mask and residual sky lines. The fraction of lost pixels achieves approximately 30% of the spectral coverage of the *H*-long band. Note that this fraction is slightly increased for observations in 2012 March (see Section 4.1). This reduces the success rate of the line detection.

Based on the full sample, we have a 37% (1931/5247) overall success rate for acquiring a spectroscopic redshift with a quality flag $z\text{Flag} \geq 1$, including all galaxies observed in any of the FMOS spectral windows. We note that, given that only $\sim 70\%$ of the *H*-long band is available for line detection due to the OH masks, the effective success rate can be evaluated to be $\sim 37/0.7 = 53\%$. The full catalog, however, contains various galaxy populations selected by different criteria, and many galaxies may satisfy criteria for different selections; i.e., the subsamples overlap each other. In later subsections, we thus focus our attention separately on each of the specific subsamples of galaxies as described in Section 3. In Table 6, we summarize the successful redshift measurements for each subsample.

5.2. The Primary Sample of Star-forming Galaxies at $z \sim 1.6$

The Primary-HL sample includes galaxies selected from the COSMOS photometric catalog, as described in Section 3.1. For these objects, our line identification assumed that the strongest line detected in the *H*-long band is the H α emission line, although, for some cases, only the [N II] line was measured, and H α was disregarded due to significant contamination on H α . For other cases with no detections in the *H*-long window, the strongest line detection in the *J*-long spectra was assumed to be the [O III] $\lambda 5007$ line. We observed 1582 galaxies that satisfy the criteria given in Section 3.1 in the *H*-long mode and successfully obtained redshift measurements with $z\text{Flag} \geq 1$ for 749 (47%) of them. The measured redshifts are in the range $1.36 \leq z_{\text{spec}} \leq 1.74$. Focusing on the detection of the H α line in the *H*-long mode, we successfully detected it for 712 (643) at $\geq 1.5\sigma$ ($\geq 3\sigma$). We note that the remaining 37 objects include [N II] detections in the *H*-long mode and H β and/or [O III] detections in the *J*-long mode. In addition to the Primary objects, we also observed another 1242 star-forming galaxies at

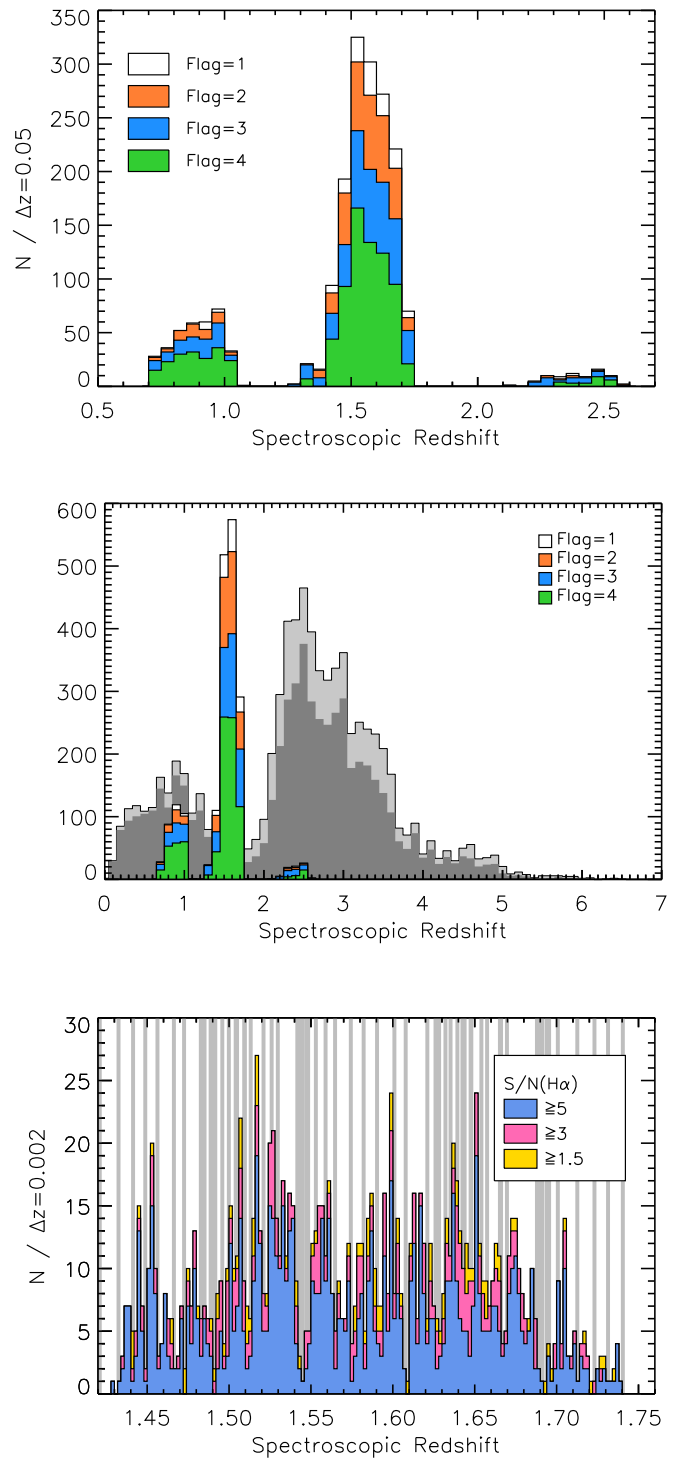


Figure 10. Distribution of spectroscopic redshift measurements for all objects in the full FMOS-COSMOS catalog, split by their quality flags. The FMOS z_{spec} distribution is compared with VUDS (Le Fèvre et al. 2015; gray histograms) in the middle panel. The bottom panel shows a zoom-in of the range $1.42 \leq z \leq 1.76$ with a finer bin size ($\Delta z = 0.002$) for objects with an H α detection in the *H*-long band. Histograms are color-coded by $S/N(\text{H}\alpha)$ as labeled. The gray stripes indicate the positions of the OH airglow lines, which are converted to redshift with the wavelength of H α .

$z \sim 1.6$ that do not match all of the criteria for the Primary target (the Secondary-HL sample; see Section 3.1). In Table 6, we summarize the number of redshift measurements for the Primary-HL and Secondary-HL samples, as well as for the subset after removing the X-ray-detected objects.

Table 6
Summary of the H α Detection for the Main Subsamples

Subsample	N_{obs}	H α Detection			Redshift Quality Flags			
		$1.5 \leq S/N < 3$	$3 \leq S/N < 5$	$S/N \geq 5$	$zF = 1$	$zF = 2$	$zF = 3$	$zF = 4$
Primary-HL	1582	69	168	475	66	162	171	350
Primary-HL (X-ray removed)	1514	67	161	454	65	155	165	330
Secondary-HL	1242	34	91	255	32	96	109	182
Secondary-HL (X-ray removed)	1201	33	87	253	29	91	107	181
<i>Herschel</i> /PACS-HL	116	5	10	38	4	10	10	32
Low- z IR galaxies	344	3	20	149	5	24	35	124
<i>Chandra</i> X-ray objects	742	12	40	144	18	57	77	129

In Figure 11, we compare the spectroscopic redshifts with the photometric redshifts used for the target selection from the photometric catalogs (Ilbert et al. 2013, 2015) for the Primary-HL sample. For those with $z\text{Flag} \geq 2$ (i.e., $\geq 3\sigma$), the median and standard deviation σ_{std} of $(z_{\text{phot}} - z_{\text{spec}})/(1 + z_{\text{spec}})$ are -0.0099 (-0.0064) and 0.028 (0.024), respectively, after (before) taking into account the effects of limiting the range of photometric redshifts ($1.46 \leq z_{\text{phot}} \leq 1.72$). To account for the edge effects, we adopted a number of sets of the median offset and σ_{std} to simulate the photometric redshift for each z_{spec} measurement, then determined the plausible values of the intrinsic median and σ_{std} that could reproduce the observed median offset and σ_{std} of $(z_{\text{phot}} - z_{\text{spec}})/(1 + z_{\text{spec}})$ after applying the limit of $1.46 \leq z_{\text{phot}} \leq 1.72$.

5.3. The *Herschel*-PACS Subsample at $z \sim 1.6$

The PACS-HL sample include 116 objects in the range $1.44 \leq z_{\text{phot}} \leq 1.72$ detected in the *Herschel*-PACS observations (Section 3.2). We successfully measured spectroscopic redshifts for 56 (43%) objects with $z\text{Flag} \geq 1$, including 32 (28%) secure measurements ($z\text{Flag} = 4$). These measurements include 43 (3, 2) detections of H α ($\geq 3\sigma$) in the H -long (H -short, J -long) band, as well as a single higher- z object with a possible detection of the [O III] doublet in the H -long band ($z_{\text{spec}} = 2.26$).

5.4. Lower-redshift Sample of IR-luminous Galaxies

In the J -long band, we observed 344 lower-redshift galaxies selected from the infrared data (see Section 3.4) and succeeded in measuring a spectroscopic redshift with $z\text{Flag} \geq 1$ for 188 objects (55%). We detected the H α emission line at $S/N \geq 1.5$ (≥ 3.0) for 172 (169) objects. We note that six objects have a detection of H β + [O III] in the J -long and are thus not within the lower-redshift window.

5.5. *Chandra* X-Ray Sample

We observed a total of 742 objects detected in the X-ray from the *Chandra* COSMOS Legacy survey (Elvis et al. 2009; Civano et al. 2016). Of these, 385 and 533 objects were observed in the H -long and J -long modes, respectively, while 177 were observed with both of these. We obtained a redshift measurement for 281 (263) objects with $z\text{Flag} \geq 1$ (≥ 2). The entire sample of X-ray objects includes 75 lower-redshift ($0.72 \leq z_{\text{spec}} \leq 1.1$) objects with a detection of H α + [N II] in the J -long band and 29 (1) higher-redshift ($2.1 \leq z_{\text{spec}} \leq 2.6$) objects with a detection of H β + [O III] in the H -long (H -short). The remaining majority of the sample are those at intermediate-redshift range with

detections of H α + [N II] in the H -long band and/or H β + [O III] in the J -long band.

6. Basic Properties of the Emission Lines

6.1. Observed Properties of H α

In Figure 12, we plot the observed in-fiber H α flux $F_{\text{H}\alpha}$ (corrected for neither dust extinction nor aperture loss) as a function of associated S/N for each galaxy in our sample, split by the spectral window. As naturally expected, there is a correlation between $F_{\text{H}\alpha}$ and S/N but with large scatter in $F_{\text{H}\alpha}$ at fixed S/N. This is mainly due to the presence of “bad pixels” impacted by OH masks and residual sky emission (see Section 4.2). The figure indicates that, in the H -long band, the best sensitivity achieves $F_{\text{H}\alpha} \sim 10^{-17}$ erg s $^{-1}$ cm $^{-2}$ at $S/N = 3$, while the average is $\sim 3 \times 10^{-17}$ erg s $^{-1}$ cm $^{-2}$.

In Figure 13, we show the correlation between $F_{\text{H}\alpha}$ (corrected for aperture but not for dust) and the FWHM of the H α line in velocity units for galaxies with an H α detection ($\geq 3.0\sigma$) in the H -long band ($1.43 \leq z_{\text{spec}} \leq 1.74$). The emission-line widths are not deconvolved for the instrumental velocity resolution (≈ 45 km s $^{-1}$ at $z \sim 1.6$). Although there is a weak correlation between these quantities, the line width becomes nearly constant at $F_{\text{H}\alpha} \gtrsim 1 \times 10^{-16}$ erg s $^{-1}$ cm $^{-2}$. The central 90th percentile of the observed FWHM is 108–537 km s $^{-1}$, with a median at 247 km s $^{-1}$. Limiting to those with $F_{\text{H}\alpha} \geq 1 \times 10^{-16}$ erg s $^{-1}$ cm $^{-2}$, the median is 292 km s $^{-1}$.

In Figure 14, we show the rest-frame equivalent width (EW_0) of the H α emission line as a function of aperture-corrected continuum flux density $\langle f_{\lambda, \text{con}} \rangle$ averaged across the H -long spectral window. The continuum flux density was computed with Equation (2), excluding the emission-line components. The equivalent widths were not corrected for differential extinction between the stellar continuum and nebular emission. The 759 objects shown here are limited to a detection of H α at $\geq 3\sigma$ in H -long and a secure measurement of the continuum level ($\geq 5\sigma$). The observed $\text{EW}_0(\text{H}\alpha)$ ranges from ≈ 10 to 300 Å, with a median $\langle \text{EW}_0(\text{H}\alpha) \rangle = 71.7$ Å. The sample shows a clear negative correlation between $\langle f_{\lambda, \text{con}} \rangle$ and $\text{EW}_0(\text{H}\alpha)$. The continuum and H α flux reflect, respectively, M_* and SFR. Thus, this correlation may be shaped by the fact that specific SFR ($\text{sSFR} = \text{SFR}/M_*$) decreases, on average, with M_* .

In Figure 15, we plot the observed H α luminosity, $L_{\text{H}\alpha}$ (corrected for aperture loss but not for dust extinction), as a function of redshift separately in the two redshift ranges that correspond to where H α is detected (J -long or H -long/short). The observed $L_{\text{H}\alpha}$ is a weak function of redshift, increasing

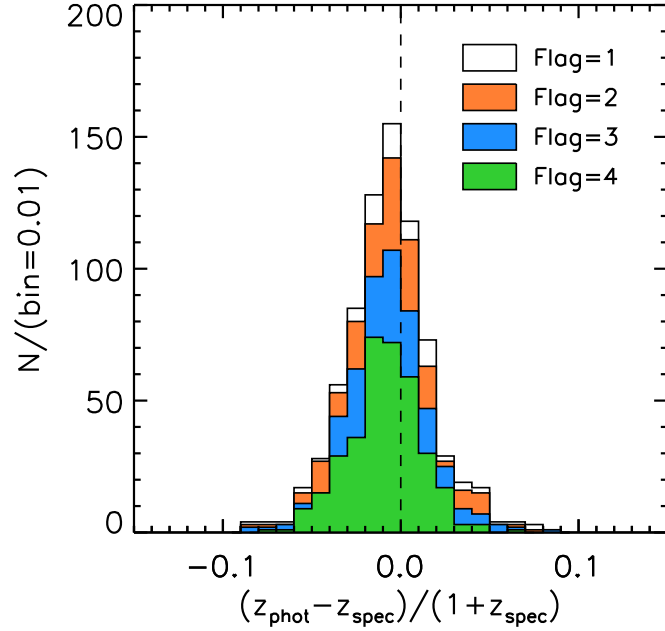
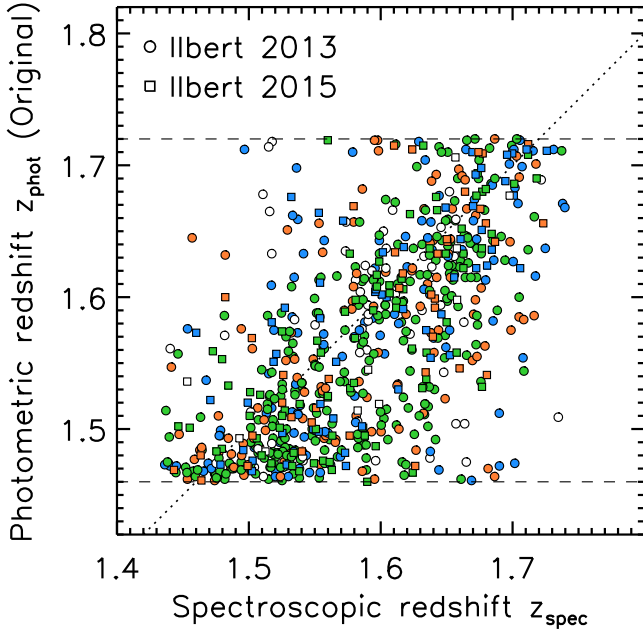


Figure 11. Upper panel: comparison between z_{spec} and z_{phot} for the Primary-HL sample. Each point is color-coded by the quality flag of the redshift measurement, as labeled in the lower panel. Circles indicate the FMOS objects selected based on the photometric redshift from Ilbert et al. (2013), while squares indicate the objects based on Ilbert et al. (2015). Lower panel: distribution of the differences between the spectroscopic redshifts from FMOS and the photometric redshifts.

toward higher redshift, as shown by the linear regression that is derived in each range. This trend is almost negligible compared to the range spanned by the sample ($\Delta z \approx 0.4$ each). For objects with an $H\alpha$ detection ($\geq 3\sigma$) in the *H*-long spectral window, the central 90th percentile of $L_{H\alpha}$ is $10^{41.7}$ – $10^{42.7}$ erg s $^{-1}$ with a median $\langle L_{H\alpha} \rangle = 10^{42.25}$ erg s $^{-1}$.

6.2. Sulfur Emission Lines

The sulfur emission lines [S II] $\lambda\lambda 6717, 6731$ fall in the *H*-long (*J*-long) spectral window, together with $H\alpha$ at

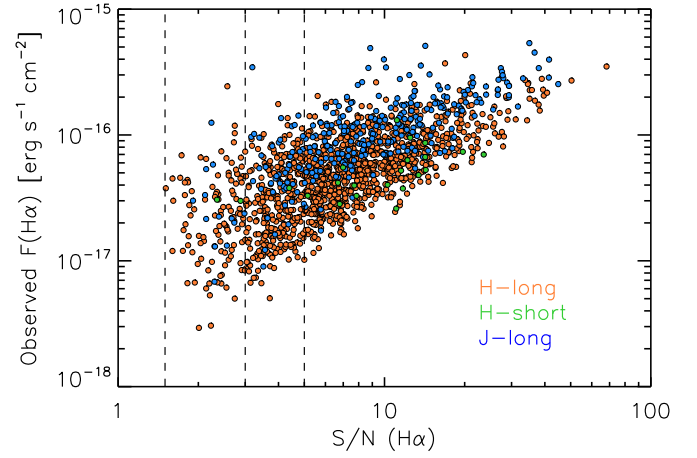


Figure 12. Observed $H\alpha$ flux (corrected for neither aperture loss nor extinction) as a function of observed formal S/N for individual galaxies, shown separately for each spectral window as labeled. Vertical dashed lines indicate S/N = 1.5 (limit for detection), 3 (limit for $z_{\text{Flag}} = 2$), and 5 (limit for $z_{\text{Flag}} = 3$).

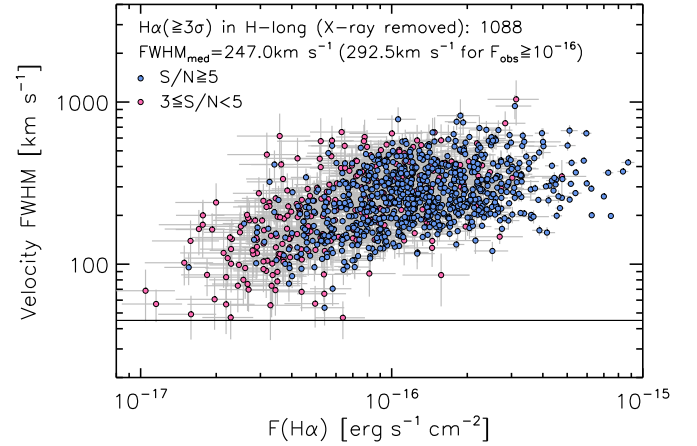


Figure 13. Correlation between aperture-corrected $H\alpha$ flux (not corrected for dust) and line width (FWHM) in velocity units. The sample shown here is restricted to those with an $H\alpha$ detection at $3 \leq S/N < 5$ (magenta) and $S/N \geq 5$ (blue) in *H*-long ($1.43 \leq z \leq 1.74$). The horizontal line indicates the velocity resolution limit (45 km s $^{-1}$).

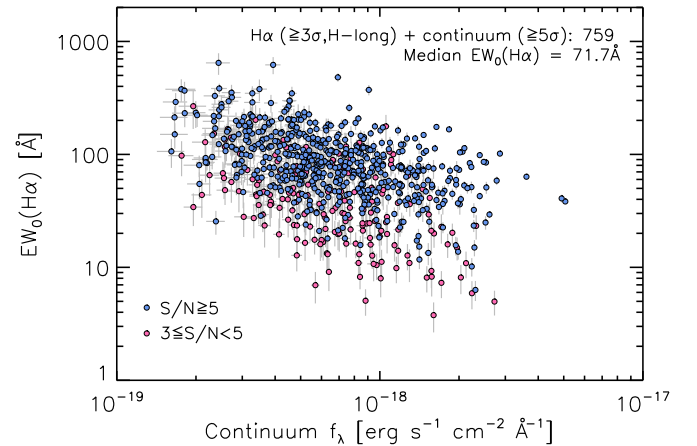


Figure 14. Rest-frame equivalent width $EW_0(H\alpha)$ as a function of aperture-corrected, average continuum flux density ($f_{\lambda, \text{con}}$). Objects shown are limited to having both $H\alpha$ detection ($\geq 3\sigma$) and reliable continuum detection ($\geq 5\sigma$). Symbols are the same as in Figure 13.

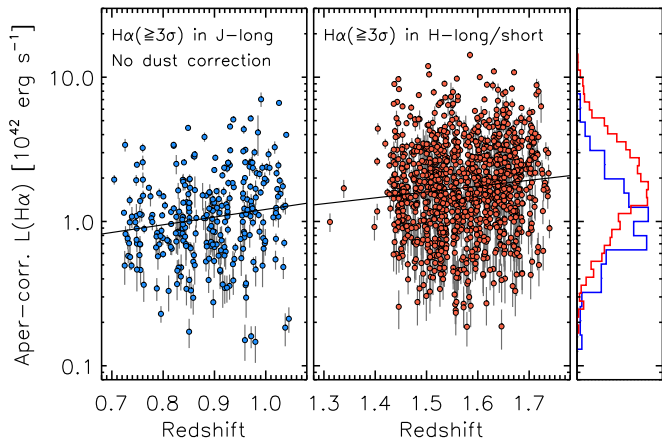


Figure 15. Observed $H\alpha$ luminosity (corrected for aperture loss but not for dust extinction) as a function of redshift in the two redshift ranges, corresponding to the $H\alpha$ detection in J -long (left panel) and H -long/short (middle panel). The solid lines indicate the linear regression being fitted independently in each redshift range. The histograms show the normalized distribution of $L_{H\alpha}$ for each redshift range as color-coded (right panel).

$1.43 < z < 1.68$ ($0.70 < z < 1.00$). For those with a detection of $H\alpha$ and/or $[N II]$, we fit the $[S II]$ lines at the fixed spectroscopic redshift determined from $H\alpha + [N II]$, as described in Kashino et al. (2017b).

We successfully detected the $[S II]$ lines for a substantial fraction of the sample. Table 7 summarizes the detections of the $[S II]$ lines. In total, we detected $[S II] \lambda 6717$ and $[S II] \lambda 6731$ at $\geq 3\sigma$ for 146 and 111 objects, respectively, with 55 with both detections at $\geq 3\sigma$ (see the top row in Table 7). Limiting those to have an $H\alpha$ detection ($> 3\sigma$) in H -long, we detected $[S II] \lambda 6717$ for 84, $[S II] \lambda 6731$ for 54, and both for 22 objects (all at $\geq 3\sigma$). In Figure 16, we show the observed fluxes of $[S II] \lambda 6717$ and $[S II] \lambda 6731$ as a function of observed $H\alpha$ flux, corrected for neither dust nor aperture loss. The observed flux of the single $[S II]$ line is, on average, $\approx 1/5$ times the observed $H\alpha$ flux, ranging from $F_{[S II]} \approx 4 \times 10^{-18}$ to 8×10^{-17} $\text{erg s}^{-1} \text{cm}^{-2}$.

7. Assessment of the Redshift and Flux Measurements

7.1. Redshift Accuracy

To evaluate the accuracy of our redshift measurements, we compared spectroscopic redshifts measured from $H\alpha + [N II]$ detected in the H -long spectra and those measured from $H\beta + [O III]$ in the J -long spectra. In the top panel of Figure 17, we show the distribution of $(z_H - z_J)/(1 + z_{\text{best}})$ for 350 galaxies with independent line detections ($\geq 3\sigma$) in both H -long and J -long. Of these, 172 objects have detections both at $\geq 5\sigma$. Here the best estimate of redshift z_{best} is based on a detection with a higher S/N between the two spectral windows. The standard deviation σ_{std} of $dz/(1+z)$ is 3.3×10^{-4} for objects with $\geq 3\sigma$ detection ($\sigma_{\text{std}} = 2.2 \times 10^{-4}$ for $\geq 5\sigma$), with a negligibly small median offset (2.6×10^{-5}). The estimated redshift accuracy $\sigma_{\text{std}}/\sqrt{2}$ is thus $\approx 70 \text{ km s}^{-1}$.

An alternative check of redshift accuracy can be done using objects that have been observed two or more times in the same spectral band on different nights. For these objects, we have selected the best spectrum to construct the line measurement catalog. However, the “secondary” measurements can be used to evaluate the “primary” ones. In the lower panel of Figure 17, we show the distribution of the difference between the primary (z_{prim}) and the second-best ($z_{2\text{nd}}$) redshift measurements,

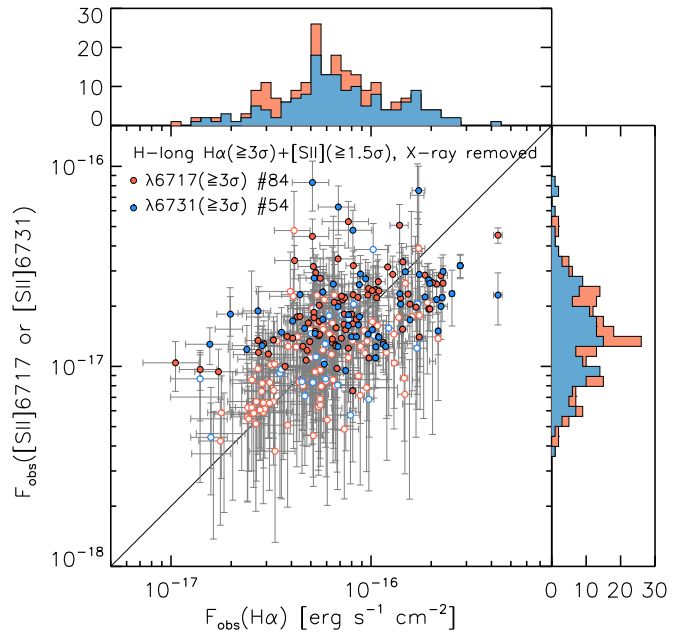


Figure 16. Correlation between observed $H\alpha$ and $[S II]$ fluxes detected in the H -long band, corrected for neither aperture loss nor extinction. Red and blue filled (open) circles indicate the $[S II] \lambda 6717$ and $[S II] \lambda 6731$ fluxes with $S/N \geq 3$ ($1.5 \leq S/N < 3$), respectively. The diagonal solid line indicates the relation of $F_{[S II]} = F_{H\alpha}/5$.

Table 7

Summary of the Detections ($\geq 3\sigma$) of the $[S II] \lambda\lambda 6717, 6731$ Lines

Subsample Criteria	$[S II] \lambda 6717$	$[S II] \lambda 6731$	Both
Any	146	111	55
In H -long	98	72	30
In J -long	47	39	25
With $H\alpha$ ($\geq 3\sigma$) in HL	84	54	22

separately for measurements obtained in H -long (29 objects) and J -long (113). Objects are limited to those with $\geq 3\sigma$ detection in the primary and secondary spectra. The standard deviation σ_{std} of $(z_{2\text{nd}} - z_{\text{prim}})/(1 + z_{\text{best}})$, reported in the figure for both H -long ($\sigma_{\text{std}} = 3.5 \times 10^{-4}$) and J -long ($\sigma_{\text{std}} = 3.3 \times 10^{-4}$) observations, is similar to that estimated by comparing the H -long and J -long measurements.

7.2. Flux Accuracy Using Repeat Observations

The secondary measurements can also be used to evaluate the accuracy of emission-line flux measurements. In Figure 18, we compare the primary and secondary measurements of the $H\alpha$ flux in the H -long window (upper panel; 24 objects) and in the $H\beta$ (middle panel; 58 objects) and $[O III] \lambda 5007$ fluxes (lower panel; 109 objects) in the J -long window. Because the two measurements are based on spectra taken under different seeing conditions, the aperture correction needs to be applied for comparison. We remind readers that the aperture correction is evaluated once for each object and observing night. It is shown that the primary and secondary measurements are in good agreement, as well as that aperture correction improves their agreement, as shown by histograms in the inset panels. We found the intrinsic scatter of these correlations to be 0.19, 0.21, and 0.19 dex for $H\alpha$, $H\beta$, and $[O III]$, respectively, after taking into account the effects of the individual formal errors of

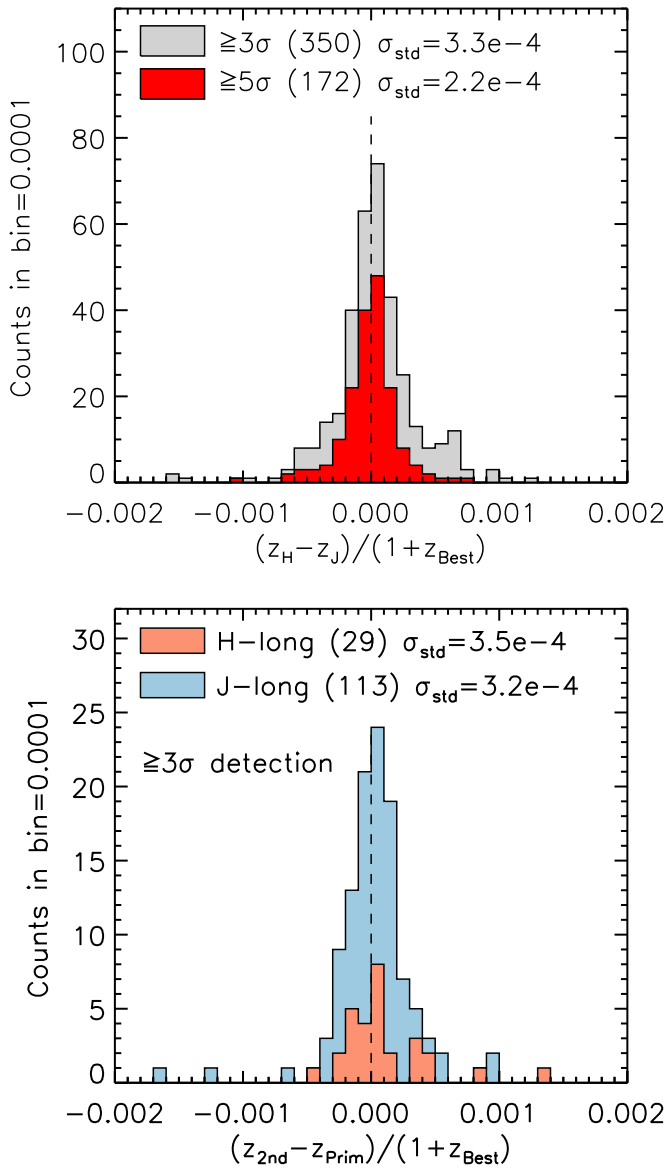


Figure 17. Upper panel: distribution of $(z_H - z_J)/(1 + z_{\text{Best}})$, the difference between spectroscopic redshifts measured from $H\alpha + [N\text{ II}]$ detected in the H -long and $H\beta + [\text{O III}]$ in the J -long spectra. The red histogram represents the subsample with a $\geq 5\sigma$ detection in both H -long and J -long spectra. Lower panel: distribution of $(z_{2\text{nd}} - z_{\text{prim}})/(1 + z_{\text{Best}})$ (see text). Red and blue histograms correspond to the measurements in the H -long and J -long, respectively. Here the line detections are limited to be $\geq 3\sigma$. In each panel, the values of standard deviation are denoted.

the observed fluxes. These intrinsic scatters should be attributed to the uncertainties of the aperture corrections and, indeed, similar to the estimates made in Section 4.5 (see Figure 9).

7.3. Comparison with MOSDEF

Some of our FMOS-COSMOS targets were observed in the MOSFIRE Deep Evolution Field (MOSDEF) survey (Kriek et al. 2015). The latest public MOSDEF catalog, released on 2018 March 11, contains 616 objects in the COSMOS field. Cross-matching with the FMOS catalog, we found 45 sources included in both catalogs, and of these, 15 objects have redshift measurements in both surveys.

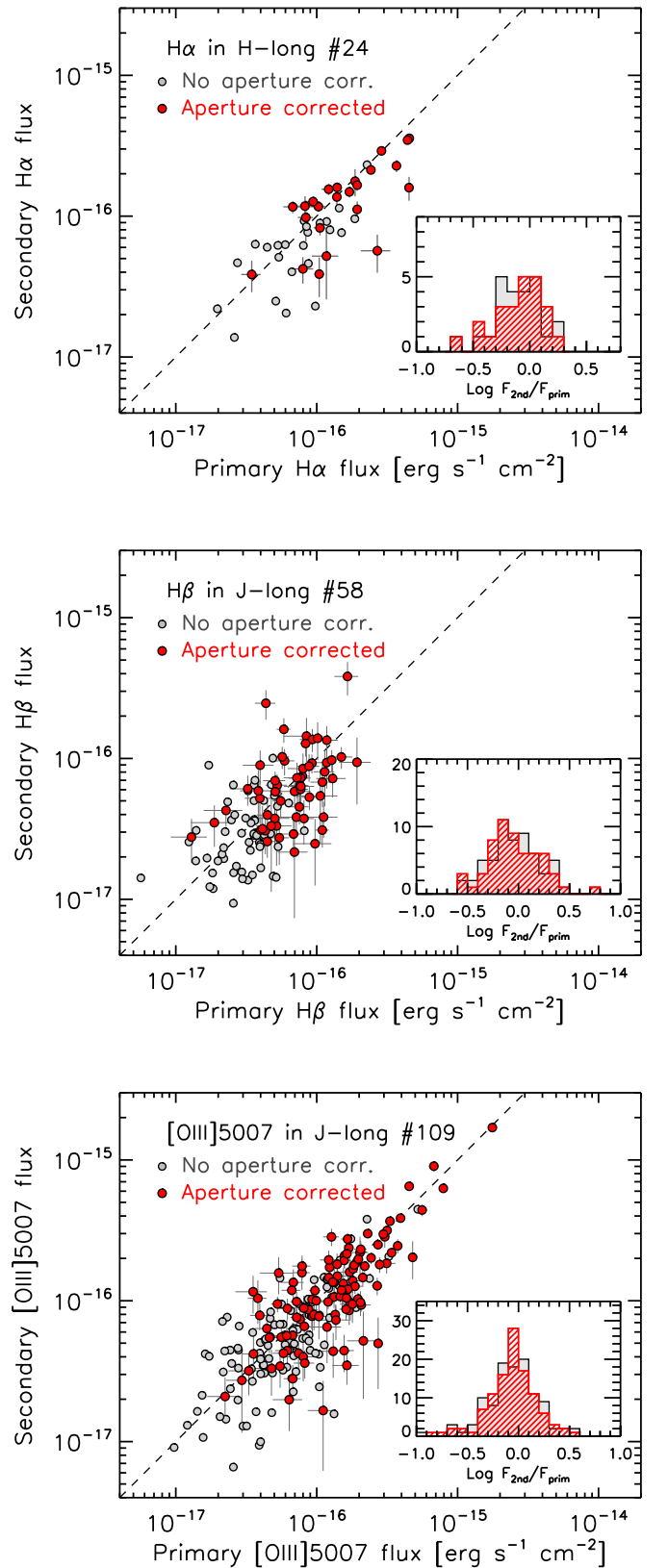


Figure 18. Comparison of the best (primary) and second-best (secondary) measurements of the $H\alpha$ flux in the H -long (top panel) and in the $H\beta$ and $[\text{O III}] \lambda 5007$ fluxes in the J -long window (middle and bottom panels) for the repeated objects. Red and gray circles indicate the observed fluxes with and without aperture correction. Inset panels show the distribution of the flux ratios $\log(F_{\text{second}}/F_{\text{primary}})$ before (gray histogram) and after (red hatched histogram) aperture correction.

Among the matching objects, all 11 FMOS measurements with $z_{\text{Flag}} = 4$ and a single $z_{\text{Flag}} = 3$ agree with the MOSDEF measurements, which all have a quality flag ($Z_{\text{MOSFIRE_ZQUAL}}$) of 7 (based on multiple emission lines at $S/N \geq 2$). The three inconsistent measurements are as follows. An object ($z_{\text{FMOS}} = 1.515$ with $z_{\text{Flag}} = 3$) has an [O III] detection at $>5\sigma$, with a possible consistent detection of $H\alpha$, in the FMOS spectra, while the MOSDEF measurement is $z = 2.101$ with a flag of 7. The photometric redshift $z_{\text{phot}} = 1.674$ (Laigle et al. 2016) prefers the FMOS measurement. For the remaining two (FMOS/MOSDEF measurements (flags) are $z_{\text{FMOS/MOSDEF}} = 1.581/2.555$ (2/6) and $z_{\text{FMOS/MOSDEF}} = 1.584/2.100$ (1/7), respectively), the detections of $H\alpha$ on the FMOS spectra are not robust, both being significantly affected by the OH mask. The photometric redshift prefers z_{MOSDEF} for the former ($z_{\text{phot}} = 2.612$) and z_{FMOS} for the latter ($z_{\text{phot}} = 1.458$). We note that there are moderately bright OH lines at 1.5088, 1.5518, and 2.0339 μm , which would perfectly conspire to emulate $H\beta$ [O III] $\lambda 5007$ and $H\alpha$ at $z = 2.099$. The two $z_{\text{MOSDEF}} = 2.10$ measurements may be affected by this circumstance.

The redshift range of the MOSDEF survey is $1 \lesssim z \lesssim 3.5$ but has a higher sampling rate at $2 < z < 2.6$. Therefore, it is not straightforward to estimate the failure rate in our survey, which could be overestimated. The small sample size of the matching objects also makes it difficult. However, we could conclude that, for objects with $z_{\text{Flag}} = 3$ and 4, the failure rate should be below 10% ($1/13 = 7.7\%$).

For these 12 consistent measurements, we found the median offset and standard deviation of $(z_{\text{FMOS}} - z_{\text{MOSDEF}})/(1 + z_{\text{MOSDEF}})$ to be -1.63×10^{-5} (4.9 km s^{-1}) and 2.57×10^{-4} (77 km s^{-1}). This indicates that there is no significant systematic offset in the wavelength calibration of the FMOS survey relative to the MOSDEF survey.

7.4. Comparison with 3D-HST

A part of the CANDELS-COSMOS field (Grogin et al. 2011; Koekemoer et al. 2011) is covered by the 3D-HST survey (Brammer et al. 2012), which is a slitless spectroscopic survey using the *HST*/WFC3 G141 grism to obtain near-infrared spectra from 1.10 to 1.65 μm . This configuration yields detections of $H\alpha$ and [O III] lines for those matched to the FMOS catalog. For redshift and flux comparisons with our measurements, we employed the public “linematched” catalogs (ver. 4.1.5) for the COSMOS field (Momcheva et al. 2016), in which the spectra extracted from the grism images were matched to photometric targets (Skelton et al. 2014).²² Cross-matching the 3D-HST and FMOS catalogs, we found 78 objects that have redshift measurements from both surveys. We divided these objects into two classes according to the quality flags in the 3D-HST catalog (flag1 and flag2). The “good” class contains 67 objects with both $\text{flag1} = 0$ and $\text{flag2} = 0$, while the remaining 11 objects are classified in the “warning” class.

In Figure 19, we compare our FMOS redshift measurements to those from 3D-HST for the 78 matching sources. The colors indicate the quality flags of the FMOS measurements (see Section 5.1), and the symbols correspond to the quality classes of the 3D-HST measurements as defined above. In the inset, we show the distribution of $(z_{\text{FMOS}} - z_{\text{3DHST}})/(1 + z_{\text{3DHST}})$ for all objects along the diagonal one-to-one line (gray histogram) for

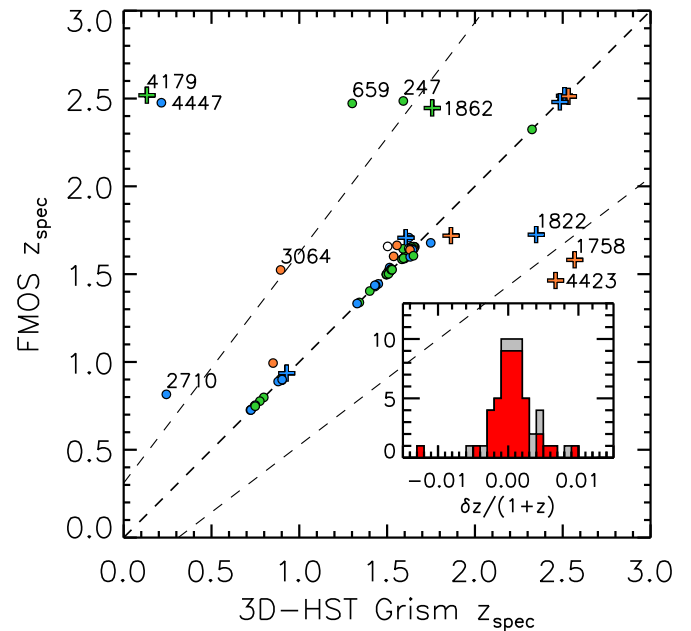


Figure 19. Comparison between spectroscopic redshift measurements from FMOS and 3D-HST. Colors indicate the quality flag of the FMOS estimation: $z_{\text{Flag}} = 1$ (white), 2 (red), 3 (blue), and 4 (green). Circles and cross symbols correspond to the “good” and “warning” classes, respectively, according to the 3D-HST flags (see text). The middle dashed line indicates the one-to-one relation, while the other two dashed lines correspond to cases where, assuming the 3D-HST measurements are correct, the $H\alpha$ line is misidentified as [O III] $\lambda 5007$ (upper line) or [O III] is misidentified as $H\alpha$. Some objects are labeled (see text).

the subsample with FMOS $z_{\text{Flag}} \geq 3$ and in the 3D-HST “good” class (red histogram). We find that an average offset of $dz/(1+z) = 0.0009$ and a standard deviation of $\sigma_{\text{std}} = 0.0029$ (0.0022 for the “good” sample) after 3σ clipping, which corresponds to 870 km s^{-1} , is consistent with the typical accuracy of the redshift determination in 3D-HST (Momcheva et al. 2016).

We further examine the possible line misidentification for the 10 cases where two spectroscopic redshifts are inconsistent (labeled in Figure 19). Of these objects, we found that the FMOS z_{spec} is quite robust for three $z_{\text{Flag}} = 4$ objects (IDs 247, 659, and 4179) and one $z_{\text{Flag}} = 3$ object (ID 4447). A single $z_{\text{Flag}} = 3$ object (ID 2710; $z_{\text{spec}} = 0.815$) has a clear detection of a single line. If this line is [S III] $\lambda 9531$ in reality, the corresponding redshift agrees with that from 3D-HST. For the other five objects, our FMOS measurements are not fully robust, including a single $z_{\text{Flag}} = 4$ object (ID 1862), while four of these are flagged as “warning” in 3D-HST. We thus would conclude that the possibility of line misidentification (including fake detections) is equal to or less than $6/67 = 9\%$, even down to $z_{\text{Flag}} \geq 2$. A similar estimate of the possibility ($\lesssim 10\%$) has been obtained from a comparison with the zCOSMOS-Deep survey (Lilly et al. 2007) for matching objects (see Silverman et al. 2015b).

Next, we compare our flux measurements to those in 3D-HST for the matching sample. In contrast to fiber spectroscopy, slitless grism spectroscopy is less affected by aperture losses and therefore offers an opportunity to check our measurements with aperture correction. Objects used for this comparison are limited to have a detection of $H\alpha$ or [O III] at $\geq 3\sigma$ in both FMOS and 3D-HST and a consistent redshift estimation ($|dz|/(1+z) \leq 0.01$). In the top panel of Figure 20, we compare

²² Available here: <http://3dhst.research.yale.edu/Home.html>.

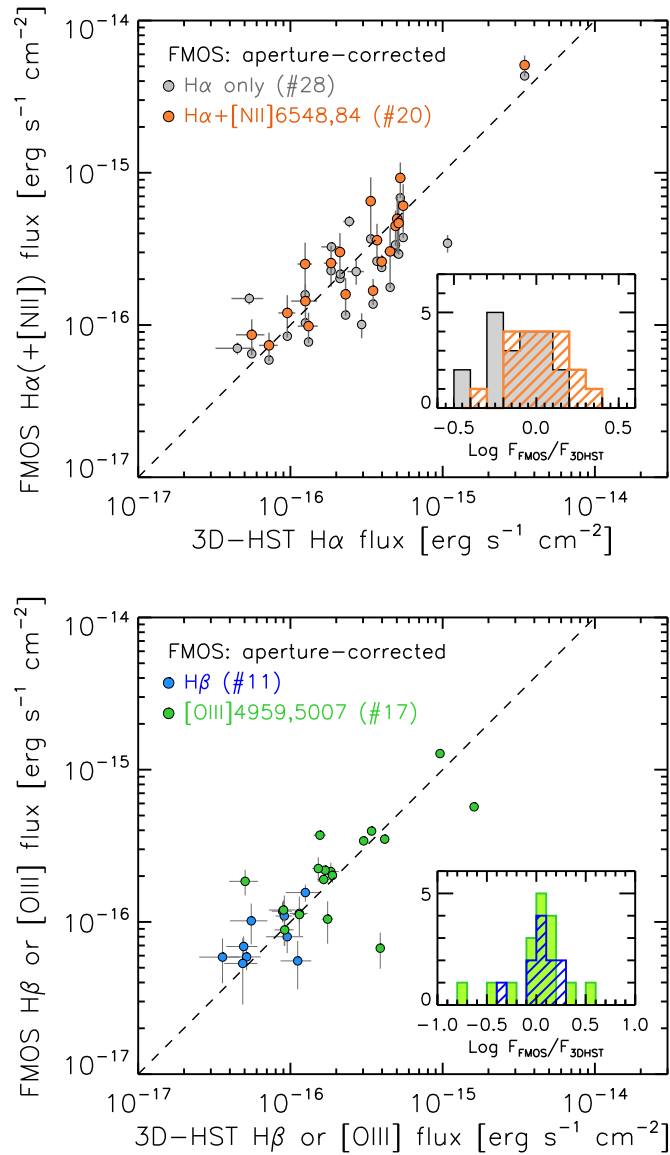


Figure 20. Comparison of the fluxes of H α (+[N II]) (upper panel) and H β and [O III] (lower panel) measured by FMOS and 3D-*HST*. The FMOS measurements are corrected for aperture loss. Gray circles indicate the H α fluxes measured by FMOS, while orange circles indicate the H α + [N II] $\lambda\lambda$ 6548, 6584 fluxes to match the 3D-*HST* measurements, in which the H α and [N II] lines are blended. Blue and green circles indicate H β and [O III] $\lambda\lambda$ 4959, 5007 fluxes, respectively. Dashed lines indicate a one-to-one relation. Insets show the distribution of the FMOS-to-3D-*HST* flux ratios, color-coded the same as the symbols.

H α fluxes measured from FMOS (corrected for aperture loss) with those from 3D-*HST* for 28 objects. Here the H α fluxes from 3D-*HST* include the contribution from [N II] $\lambda\lambda$ 6548, 6584 because these lines are blended with H α due to the low spectral resolution ($R \sim 100$). Therefore, we also show the total fluxes of H α and [N II] $\lambda\lambda$ 6548, 6584 for the FMOS measurements (orange circles). Eight of the 28 objects have no detection of [N II]. Even with no inclusion of [N II], good agreement is seen between the measurements of both programs, with a median offset of -0.09 dex and an rms scatter of 0.23 dex. As naturally expected, the inclusion of [N II] lines further improves the agreement, resulting in an offset of 0.02 dex and a scatter of 0.17 dex.

The bottom panel of Figure 20 shows the comparisons of observed H β and [O III] fluxes. We show the total fluxes of

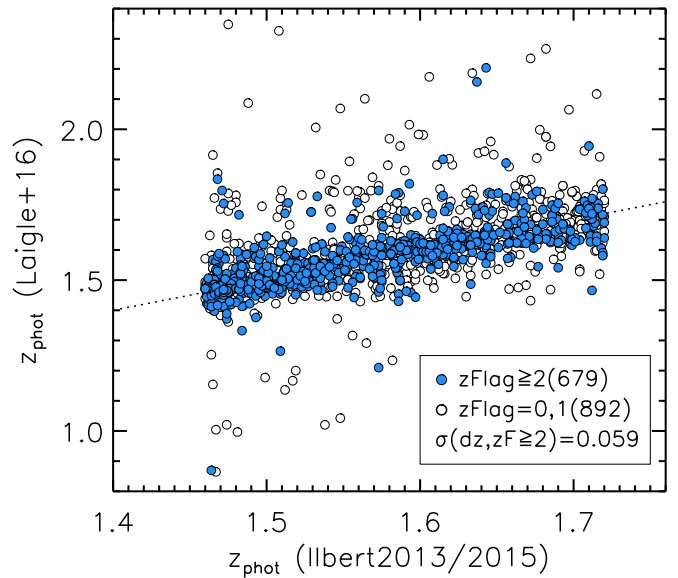


Figure 21. Comparison between the photometric redshifts from our original parent catalog based on Ilbert et al. (2013, 2015) and the COSMOS2015 catalog (Laigle et al. 2016). White and blue circles indicate objects with zFlag = 0 and 1 and those with zFlag ≥ 2 , respectively. The dotted line indicates a one-to-one relation.

[O III] $\lambda\lambda$ 4959, 5007 for the FMOS measurements because 3D-*HST* does not resolve the [O III] doublet. Similar to H α , there is good agreement between flux measurements for these lines with little average offset (<0.1 dex) and small scatter (<0.2 dex).

The agreement of our flux measurements with the slitless measurements from 3D-*HST* indicates the success of our absolute flux calibration including aperture correction. The scatter found in the comparisons (~ 0.2 dex) is equivalent to that found in comparisons using repeat observation (Section 7.2), as well as to the typical uncertainty in the aperture correction (Section 4.5).

8. Retroactive Evaluation of the FMOS-COSMOS Sample

The master catalog of our FMOS survey contains various galaxy populations selected in different ways, as described above. Even for the primary population of star-forming galaxies at $z \sim 1.6$, whose H α is expected to be detected in the *H*-long spectral window, the quantities used for the selection, such as photometric redshift, stellar mass, and predicted H α fluxes, had been updated during the period of the project. Therefore, it is useful to reevaluate the FMOS sample using a single latest photometric catalog as a base, in which galaxy properties are derived in a consistent way. For the retroactive characterization of the sample, we rely on the COSMOS2015 catalog (Laigle et al. 2016), which contains an updated version of the photometry and photometric redshifts, as well as estimates of the stellar mass and SFR, for objects across the full area of the COSMOS field.

In Figure 21, we compare the photometric redshifts in the COSMOS2015 catalog with those originally used for target selection. Here we show FMOS objects that are included in the Primary-HL sample defined in Section 3.1 and matched in the COSMOS2015 catalog. It is clear that the photometric redshift estimates from the different versions of the COSMOS photometric catalogs are in good agreement. The standard

deviation of dz for the $z\text{Flag} \geq 2$ objects is $\sigma(dz) = 0.059$ after 5σ clipping, which is in good agreement with the typical errors of the photometric redshifts relative to the spectroscopic redshifts (see Section 5.2).

8.1. Sample Construction

In this section, we focus our attention on the star-forming population at $z \sim 1.6$, in particular, with a detection of $H\alpha$ at $\geq 3\sigma$. Therefore, we limit this discussion to those that were observed in the H -long band. We exclude X-ray objects identified in the *Chandra* COSMOS Legacy catalog (see Section 3.3).

We first construct a broad sample from COSMOS2015, named *Broad-L16*, to be sufficiently deep relative to the FMOS sample. We limit the sample to be flagged as a galaxy ($\text{TYPE} = 0$), being within the strictly defined 2 deg^2 COSMOS field ($\text{FLAG_COSMOS} = 1$), inside the UltraVISTA field ($\text{FLAG_HJMCC} = 0$), inside the good area (not masked area) of the optical broadband data ($\text{FLAG_PETER} = 0$), and inside the FMOS area covered by all of the pawprints (see Figure 1). As a consequence, the effective area used for this evaluation is 1.35 deg^2 , after removing the masked regions.²³ For details of these flags, we refer the reader to Laigle et al. (2016).

We further impose a limit on the photometric redshift $1.3 \leq z_{\text{phot}} \leq 1.9$ and the UltraVISTA K_S -band magnitude $K_S \leq 24.0$, where we use the $3''$ aperture magnitude ($K_{S_MAG_APER3}$). This limiting magnitude corresponds to the 3σ limit in the UltraVISTA deep layer and $\geq 5\sigma$ for the ultra-deep layer. Finally, we find 39,435 galaxies satisfying these criteria. We then performed the position matching between the H -long sample and the COSMOS2015 catalog with a maximum position error of $1''.0$, yielding the matched sample that consists of 2878 objects ($\text{Broad-L16} \cap \text{FMOS HL}$).²⁴ The fraction with respect to the Broad-L16 sample is 7.3%, and we detected $H\alpha$ at $\geq 3\sigma$ for 1014 of these; thus, the success rate is 35% (1014/2878).

Next, we imposed additional limits on the Broad-L16 sample while simultaneously trying to keep the sampling rate as high as possible and not lose $H\alpha$ -detected objects. For this purpose, we use the stellar mass and SFR estimates from SED fitting given in the COSMOS2015 catalog. We computed predicted $H\alpha$ fluxes as follows:

$$F_{H\alpha}^{\text{pred}} = \frac{1}{4\pi d_L(z_{\text{phot}})^2} \frac{\text{SFR}/(M_{\odot} \text{ yr}^{-1})}{4.6 \times 10^{-42}} \times 10^{-0.4A_{H\alpha}}. \quad (6)$$

This is the modified version of Equation (2) of Kennicutt (1998) for the use of a Chabrier (2003) IMF. Dust extinction is taken into account with $A_{H\alpha} = k_{H\alpha} E(B - V)/f_{\text{neb}}$, where $k_{H\alpha} = 2.54$ is the wavelength dependence of extinction (Cardelli et al. 1989). The extinction $E(B - V)$ is taken from the COSMOS2015 catalog²⁵ and is multiplied by a factor of

$1/f_{\text{neb}} = 1/0.5$ to account for enhancement of extinction toward nebular lines (see Section 9.3).²⁶ Finally, we define the *Selected-L16* sample by imposing the criteria $K_S \leq 23.0$, $1.43 \leq z_{\text{phot}} \leq 1.74$, $\log M_*/M_{\odot} \geq 9.6$, and the predicted $H\alpha$ flux $F_{H\alpha}^{\text{pred}} \geq 1 \times 10^{-16} \text{ erg s}^{-1} \text{ cm}^{-2}$, in addition to the criteria on the Broad-L16 sample. As a consequence, the Selected-L16 sample includes 3714 objects.

Cross-matching the Selected-L16 sample with the FMOS H -long sample, we find 1209 objects, and 628 of these have a successful detection of $H\alpha$ ($\geq 3\sigma$) in the H -long spectra. Thus, the sampling rate is 33% (1209/3714), and the success rate is 52% (628/1209). It is worth noting that the rate of failure detection can be reasonably explained: if the redshift distribution is uniform, approximately 20% of those within $1.43 \leq z_{\text{phot}} \leq 1.74$ may fall outside the redshift range covered by the H -long window for their uncertainty on the photometric redshift ($\delta z_{\text{phot}} \approx 0.06$; see below). Moreover, $\approx 35\%$ of the potential objects may be lost due to severe contamination by OH skylines (see Figure 10). In Table 8, we summarize the selection and the sizes of the samples defined in this section. We note that it is not guaranteed that all objects in the Selected-L16 sample were included in the input sample for the fiber allocation software.

8.2. Sampling and Detection Biases

We investigate possible biases in the FMOS sample as functions of the properties of galaxies. In Figure 22, we show the distribution of the SED-based quantities (z_{phot} , K_S , M_* , SFR, and $F_{H\alpha}^{\text{pred}}$ from left to right) for galaxies matched in the Broad-L16 sample. As shown in the top panels of Figure 22, the sampling rates of both the observed and $H\alpha$ -detected sample depend on these quantities. We note that the nonuniform sampling in terms of z_{phot} is trivial because we preferentially selected galaxies within a narrower range of z_{phot} ($1.46 \leq z_{\text{phot}} \leq 1.72$), within which the sampling is nearly uniform. In the middle panel in each column, we show the success rate, which is the fraction of the $H\alpha$ -detected objects relative to the observed objects at a given x -axis value. It is also clear that the success rate depends significantly on these galaxy properties, e.g., as shown by the trends with K_S and $F_{H\alpha}^{\text{pred}}$.

Next, we show the Selected-L16 sample in the same manner in Figure 23. At first glance, the distribution of the observed/ $H\alpha$ -detected FMOS objects is more similar to that of the parent sample. Correspondingly, it is also clear that the sampling rate is now more uniform against any quantity of these than those of the Broad-L16 sample shown in Figure 22. However, the sampling rate still varies substantially as a function of some of these galactic properties. In particular, the sampling rate increases rapidly around $\log M_*/M_{\odot} \approx 10^{10.5}$. Given a tight correlation between M_* and K_S magnitude, this trend with M_* corresponds to the decrease in the sampling rate with increasing K_S . This is partially because the latter part of our observations was especially dedicated to increasing the sampling rate of most massive galaxies. However, the success rate shows no significant trend as a function of M_* and K_S -band magnitude. As opposed to M_* (or K_S), not only the sampling rate but also the success rate appears to increase as $F_{H\alpha}^{\text{pred}}$ increases (right panels). This is naturally expected because stronger lines are

²³ The DS9 format region files for the outlines and masked regions are available online: <http://cosmos.astro.caltech.edu/page/photom>.

²⁴ We note that, from matching the full FMOS-COSMOS catalog to the full COSMOS2015 catalog, we find a best-matched counterpart for 5157 extragalactic objects. The public FMOS-COSMOS catalog contains the best-matched ID for objects in the COSMOS2015 catalog for each FMOS object (a column `ID_LAIGLE16`).

²⁵ Although we here assume a single attenuation curve for nebular emission from Cardelli et al. (1989), different attenuation curves for stellar emission have been applied for different objects in the COSMOS2015 catalog, which induces systematic uncertainties in the estimates of $E(B - V)$.

²⁶ This factor makes the value of $k_{H\alpha}/f_{\text{neb}}$ nearly the same as that with the Calzetti et al. (2000) law ($k_{H\alpha} = 3.325$) and $f_{\text{neb}} = 0.66$, as used in our target selection and past papers.

Table 8
Summary of the Sampling and Success Rates

Sample	Selection	N_{galaxies}	Fraction
Broad-L16	In the FMOS field (1.35 deg ²) And TYPE = 0 (flagged as a galaxy) And FLAG_COSMOS = 1 And FLAG_HJMCC = 0 And FLAG_PETER = 0 And $K_S \leq 24.0$ and $1.3 \leq z_{\text{phot}} \leq 1.9$	39,435	
\cap FMOS HL	And observed in the H -long	2878	7.3% (2878/39,435)
\cap FMOS HL + H α	And H α detection (3σ) in the H -long	1014	35.2% (1014/2878)
Selected-L16	Criteria for Broad-L16 And $K_S \leq 23.0$ and $1.43 \leq z_{\text{phot}} \leq 1.74$ And $\log M_*/M_\odot \geq 9.6$ And $F_{\text{H}\alpha}^{\text{pred}} \geq 1 \times 10^{-16}$ erg s ⁻¹ cm ⁻²	3714	
\cap FMOS HL	And observed in the H -long	1209	32.6% (1209/3714)
\cap FMOS HL + H α	And H α detection (3σ) in the H -long	628	51.9% (628/1209)

more easily detected. From these results, we conclude that the spectroscopic sample (even after applying the criteria defined in this section) is biased toward massive galaxies and having higher $F_{\text{H}\alpha}^{\text{pred}}$.

To quantify these trends, we show in Figure 24 the cumulative sampling and success rates as a function of M_* (upper panel) and predicted H α flux (lower panel). The cumulative sampling rate is defined as the fraction of observed and/or H α -detected galaxies above a given M_* or $F_{\text{H}\alpha}^{\text{pred}}$ with respect to the Selected-L16 sample but without the limit on the quantity corresponding to the x -axis. The cumulative success rate is defined in the same manner between the H α -detected and observed galaxy samples. In the upper panel, it is shown that the cumulative sampling rate of the observed galaxies (\cap FMOS HL; red line) increases at $M_* \geq 10^{10} M_\odot$ and reaches a level of $\approx 60\%$ ($\approx 35\%$) at $M_* = 10^{10.7} M_\odot$. The cumulative sampling rate of the H α -detected subsample (green line) shows a similar trend, increasing monotonically with M_* from 17% at the lower M_* limit to 35% at $10^{11} M_\odot$. In contrast, the cumulative success rate (purple line) is nearly uniform across the entire M_* range. In the lower panel of Figure 24, the cumulative sampling rate for the H α -detected subsample (green line) increases from $\sim 10\%$ at $F_{\text{H}\alpha}^{\text{pred}} < 10^{-16}$ erg s⁻¹ cm⁻² to 35%. The cumulative success rate (purple line) also increases slowly from 40% to 70% as the threshold $F_{\text{H}\alpha}^{\text{pred}}$ increases.

8.3. Comparison with the Spectroscopic Measurements

We compare our spectroscopic measurements with those based on the SED fits from COSMOS2015. In Figure 25, we compare the spectroscopic redshifts with the photometric redshifts. Limiting those in the Selected-L16 sample (red circles and red histogram), we find that the median and the standard deviation of $(z_{\text{phot}} - z_{\text{spec}})/(1 + z_{\text{spec}})$ are -0.0112 (-0.0086) and 0.0264 (0.0237), respectively, after (before) taking into account the effect of limiting the range of photometric redshifts ($1.43 \leq z_{\text{phot}} \leq 1.74$). The level of the uncertainties in the photometric redshifts is very similar to that in the older version (Ilbert et al. 2013), as described in Section 5.2. Because there is only a little systematic offset in our z_{spec} measurements in comparison with the MOSDEF and 3D-*HST* surveys (Section 7), the median offset between z_{spec}

and z_{phot} , which is significant compared to the scatter, should be regarded as the systematic uncertainty in the photometric redshifts.

Next, in Figure 26, we compare the observed H α fluxes to the predicted H α fluxes. The observed fluxes are converted to the total fluxes by applying the aperture correction (see Section 4.5). Note that the observed fluxes are not corrected for extinction, while the predicted fluxes include the reduction due to extinction. It is shown that the observed fluxes are in broad agreement with the predicted values. Limiting those in the Selected-L16 sample (red circles), we found a small systematic offset of $\log F_{\text{H}\alpha}^{\text{obs}}/F_{\text{H}\alpha}^{\text{pred}} = -0.16$ dex (median). This offset may be attributed to the application of inaccurate dust extinction. We revisit the dust extinction by using the new estimates of galaxy properties with spectroscopic redshifts in Section 9.3.

9. Stellar Mass and SFR Estimation

9.1. SED Fitting with LePhare

For FMOS galaxies with a spectroscopic redshift based on an emission-line detection, we rederived the stellar masses based on SED fitting using LePhare (Arnouts et al. 2002; Ilbert et al. 2006). The stellar mass is defined as the total mass contained in stars at the considered age without the mass returned to the ISM. Our procedure follows the same method as in Ilbert et al. (2015) and Laigle et al. (2016); i.e., our estimation is consistent with the COSMOS2015 catalog. The SED library contains synthetic spectra generated using the population synthesis model of Bruzual & Charlot (2003), assuming a Chabrier (2003) IMF. We considered 12 models combining the exponentially declining SFH ($e^{-t/\tau}$ with $\tau/\text{Gyr} = \{0.1:30\}$) and delayed SFH ($te^{-t/\tau}$ with $\tau = 1$ and 3 Gyr) with two metallicities (solar and half solar) applied. We considered two attenuation laws, including the Calzetti et al. (2000) law and a curve $k(\lambda) = 3.1(\lambda/5500 \text{ \AA})^{-0.9}$, with $E(B - V)$ being allowed to take values as high as 0.7.

For the SED fitting, we used photometry from the COSMOS2015 catalog measured with 30 broad-, intermediate-, and narrowband filters from *GALEX* NUV to *Spitzer*/*IRAC* ch2 (4.5 μm), as listed in Table 3 of Laigle et al. (2016).

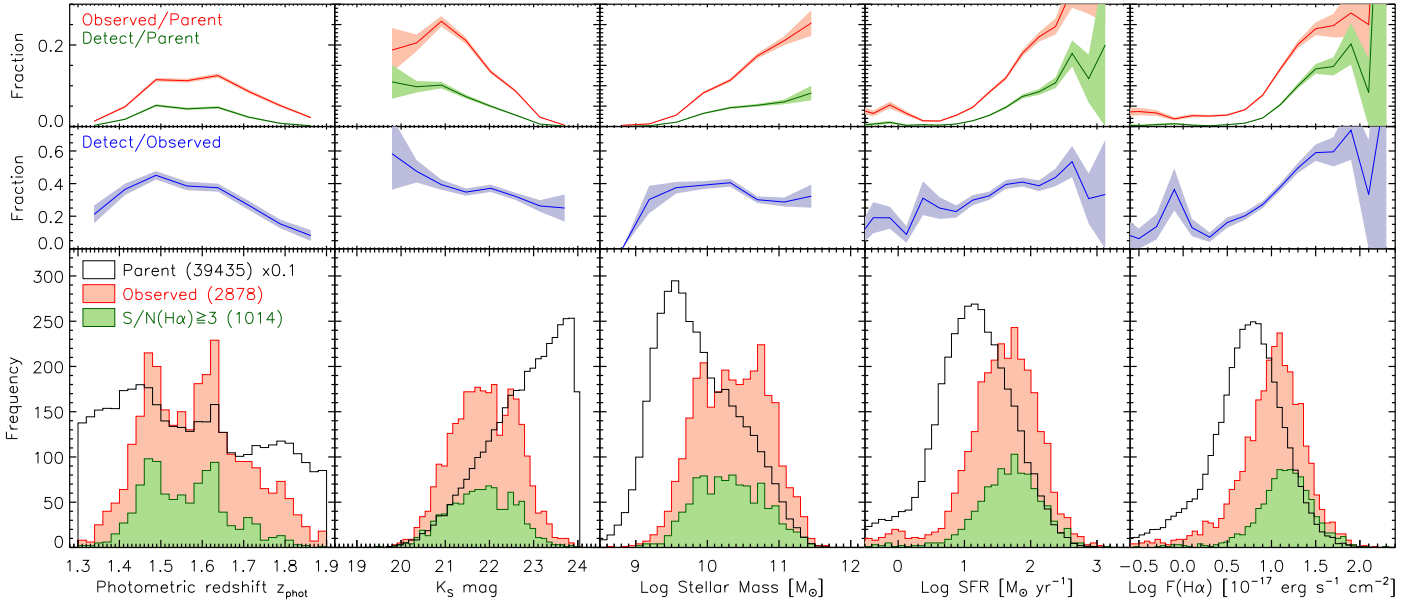


Figure 22. Distribution of the SED-based photometric redshifts, K_S magnitudes, stellar masses, SFRs, and predicted $H\alpha$ fluxes (left to right). The open histograms show the distributions of the parent Broad-L16 sample ($N = 39,435$), scaled by a factor of 0.1, while the filled red and green histograms indicate the observed (\cap FMOS HL; $N = 2878$) and $H\alpha$ -detected (\cap FMOS HL + $H\alpha$; $N = 1014$) samples (see Table 8). In the top panels, the fraction of the observed and $H\alpha$ -detected samples relative to the parent sample is shown for each quantity. In the middle panels, the fraction of the $H\alpha$ -detected sample to the observed sample is shown. In the top and middle panels, the shaded regions indicate the Poisson errors in each bin.

Note that IRAC ch3 and ch4 were excluded, since the photometry in these bands may be affected by the PAH emissions, which are not modeled in our templates. For CFHT, Subaru, and UltraVISTA photometry, we used measurements in $3''$ aperture fluxes and applied the offsets provided in the catalog to convert them to the total fluxes.

In Figure 27, we show the histograms of the resulting χ^2/N_{band} values (where N_{band} is the number of bandpasses that were used for fitting) for the best-fit SEDs separately for non-X-ray and X-ray-detected sources (see Section 3.3). It is shown that the χ^2/N_{band} values are concentrated around $\chi^2/N_{\text{band}} = 1$ for non-X-ray star-forming galaxies, which indicates that the fitting has reasonably succeeded for the majority of the sample. In contrast, the fitting may be unreasonable for many of the X-ray sources, as indicated by their χ^2/N_{band} distribution, which is widely spread out to $\chi^2/N_{\text{band}} \sim 100$. The main reason for such lower goodness-of-fit is the additional emission from an AGN at the rest-frame UV and near-to-mid-IR wavelengths. The derivation of SED properties for X-ray sources, accounting for the AGN emission component, is postponed to a future companion paper (D. Kashino et al. 2019, in preparation). Throughout the paper, we disregard the LePhare estimates for all X-ray-detected sources and those with $\chi^2/N_{\text{band}} \geq 6$.

9.2. SFRs from the UV Luminosity

We estimated the total SFR of our sample galaxies directly from the UV continuum luminosity in order to compare with those estimated from $H\alpha$ luminosity. Dust extinction is accounted for based on the slope β_{UV} of the rest-frame UV continuum spectrum (e.g., Meurer et al. 1999). The UV slope β_{UV} is defined as $f_{\lambda} \propto \lambda^{\beta_{\text{UV}}}$. We measured the rest-frame FUV (1600 \AA) flux density and β_{UV} by fitting a power-law function to the broad- and intermediate-band fluxes within $1200 \text{ \AA} \leq \lambda_{\text{eff}}/(1+z) \leq 2600 \text{ \AA}$, where λ_{eff} is the effective wavelength

of the corresponding filters. The slope β_{UV} is converted to the FUV extinction, A_{1600} , as well as to the reddening value, $E_{\text{star}}(B-V)$, with the following relations from Calzetti et al. (2000):

$$A_{1600} = 4.85 + 2.31 \beta_{\text{UV}}, \quad (7)$$

$$E_{\text{star}}(B-V) = A_{1600}/k_{1600}, \quad (8)$$

where $k_{1600} = 10.0$. We set the lower and upper limits to be $E_{\text{star}}(B-V) = 0$ and 0.8, respectively. The extinction-corrected UV luminosity, L_{1600} , is then converted to SFR using a relation from Daddi et al. (2004),

$$\text{SFR}_{\text{UV}}(M_{\odot} \text{ yr}^{-1}) = \frac{L_{1600}(\text{erg s}^{-1} \text{ Hz}^{-1})}{1.7 \times 8.85 \times 10^{27}}, \quad (9)$$

where a factor of $1/1.7$ is applied to convert from a Salpeter (1955) IMF to a Chabrier (2003) IMF. We disregard the measurements with poor constraints of either the UV luminosity ($<5\sigma$) or the UV slope $\sigma(\beta_{\text{UV}}) > 0.5$ (only 6% of the sample of $H\alpha$ -detected ($\geq 3\sigma$) galaxies).

In the upper panel of Figure 28, we show the distributions of the estimates of M_* and UV-based SFR for the entire FMOS sample, removing those with a resultant $\chi/N_{\text{band}}^2 \geq 6$ and X-ray objects. Objects are shown in the figure separated into three redshift ranges, as labeled. In the lower panel of Figure 28, we show the reddening $E_{\text{star}}(B-V)$, estimated from β_{UV} , as a function of M_* for the same objects shown in the upper panel. It is clear that the average and scatter in $E_{\text{star}}(B-V)$ increase with increasing M_* .

9.3. $H\alpha$ -based SFR and Extinction Correction

Next, we compute the intrinsic SFR from the observed $H\alpha$ flux, applying a correction for aperture loss and dust extinction,

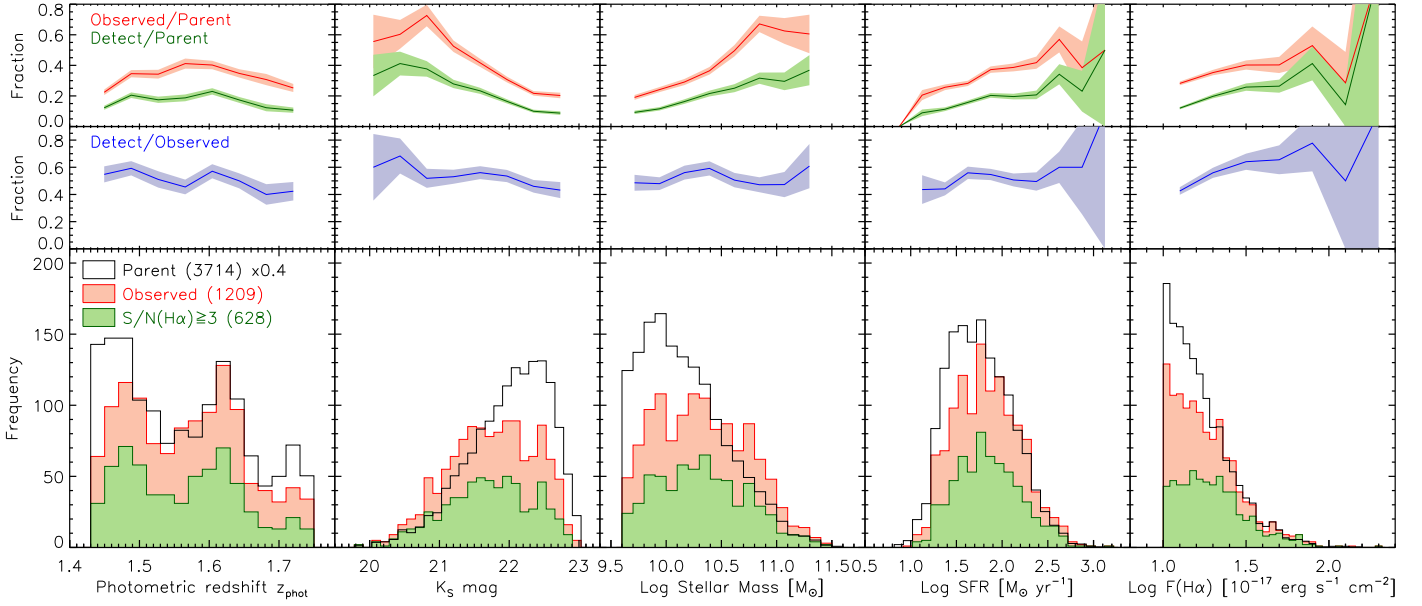


Figure 23. Same as Figure 22 but for the Selected-L16 sample ($N = 3714$) and the corresponding “ \cap FMOS HL” ($N = 1209$) and H α -detected (\cap FMOS HL + H α ; $N = 628$) samples (see Table 8). The open histograms are scaled by a factor of 0.4.

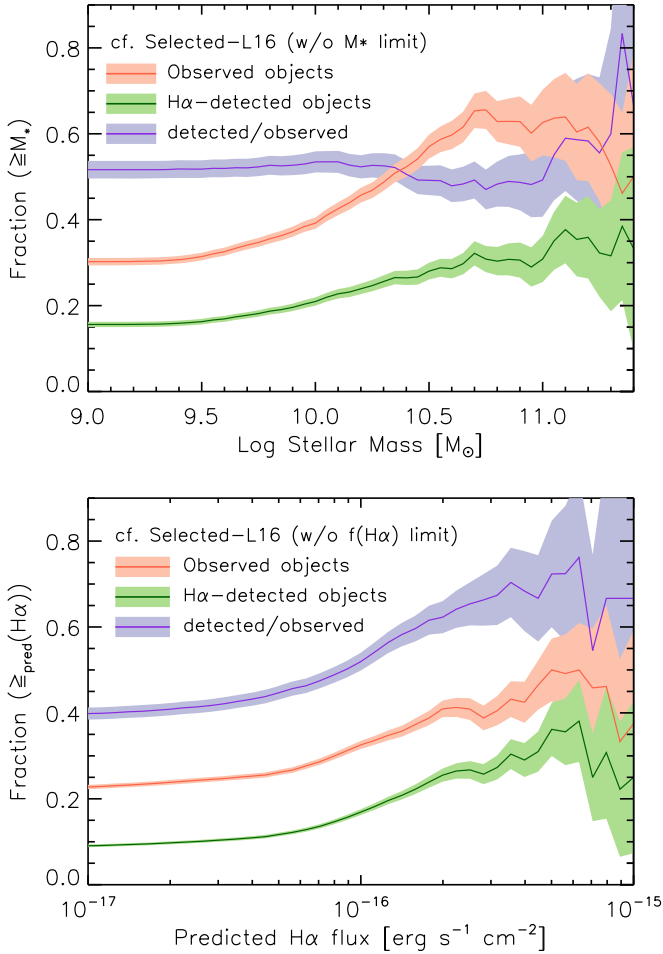


Figure 24. Cumulative sampling rate and success rate above a given M_* (upper panel) and predicted H α flux (lower panel). The red line indicates the sampling fraction of galaxies within the Selected-L16 sample but without the limit on the x -axis value in each panel. The green line indicates the fractions of the H α -detected objects with respect to the Selected-L16 sample. The purple line indicates the cumulative success rate, which is the fraction of H α -detected objects with respect to the observed galaxies above a given value.

through Equation (6). It is known that the extinction of the nebular emission is enhanced, on average, relative to the extinction toward the stellar component, which is expressed with a factor f_{neb} as $E_{\text{neb}}(B - V) = E_{\text{star}}(B - V)/f_{\text{neb}}$. In the local universe, a factor $f_{\text{neb}} = 0.44$, derived by Calzetti et al. (2000), has been widely applied, whereas observations at higher redshifts have measured larger values (~ 0.5 – 1 ; e.g., Kashino et al. 2013; Price et al. 2014). There remain large uncertainties in the constraints on the f_{neb} factor because these results may depend on the method used to determine the level of extinction and the extinction laws applied. In the remainder of the paper, we adopt the Cardelli et al. (1989; $R_V = 3.1$) and Calzetti et al. (2000; $R_V = 4.05$) extinction laws, respectively, for the nebular and stellar extinction, following the analysis in the original work of Calzetti et al. (2000), where they used a similar law by Fitzpatrick (1999) for the nebular emission.

We here determine the f_{neb} by comparing the SFRs estimated from the observed H α and UV luminosities, both uncorrected for dust extinction, as in Kashino et al. (2013). For this investigation, we limit our sample to 702 galaxies having H α detection ($\geq 5\sigma$) and estimates of M_* , SFR_{UV} , and $E_{\text{star}}(B - V)$ (see Section 9). We excluded all X-ray-detected objects and possible AGNs flagged by the emission-line width of $\geq 1000 \text{ km s}^{-1}$ and/or their emission-line ratios of [O III] $\lambda 5007/\text{H}\beta$ and [N II] $\lambda 6584/\text{H}\alpha$ (see Kashino et al. 2017b for details).

Assuming that the appropriate dust correction equalizes the UV- and H α -based SFRs, the dust-uncorrected ratio $\text{SFR}_{\text{H}\alpha}^{\text{uncorr}}/\text{SFR}_{\text{UV}}^{\text{uncorr}}$ is expressed as a function of $E_{\text{star}}(B - V)$ with a parameter f_{neb} as follows:

$$\log \left(\frac{\text{SFR}_{\text{H}\alpha}^{\text{uncorr}}}{\text{SFR}_{\text{UV}}^{\text{uncorr}}} \right) = -0.4 E_{\text{star}}(B - V) \times \left(\frac{k_{\text{H}\alpha}}{f_{\text{neb}}} - k_{1600} \right), \quad (10)$$

where $k_{1600} = 10.0$ (Calzetti et al. 2000) and $k_{\text{H}\alpha} = 2.54$ (Cardelli et al. 1989). The observed H α flux is converted to

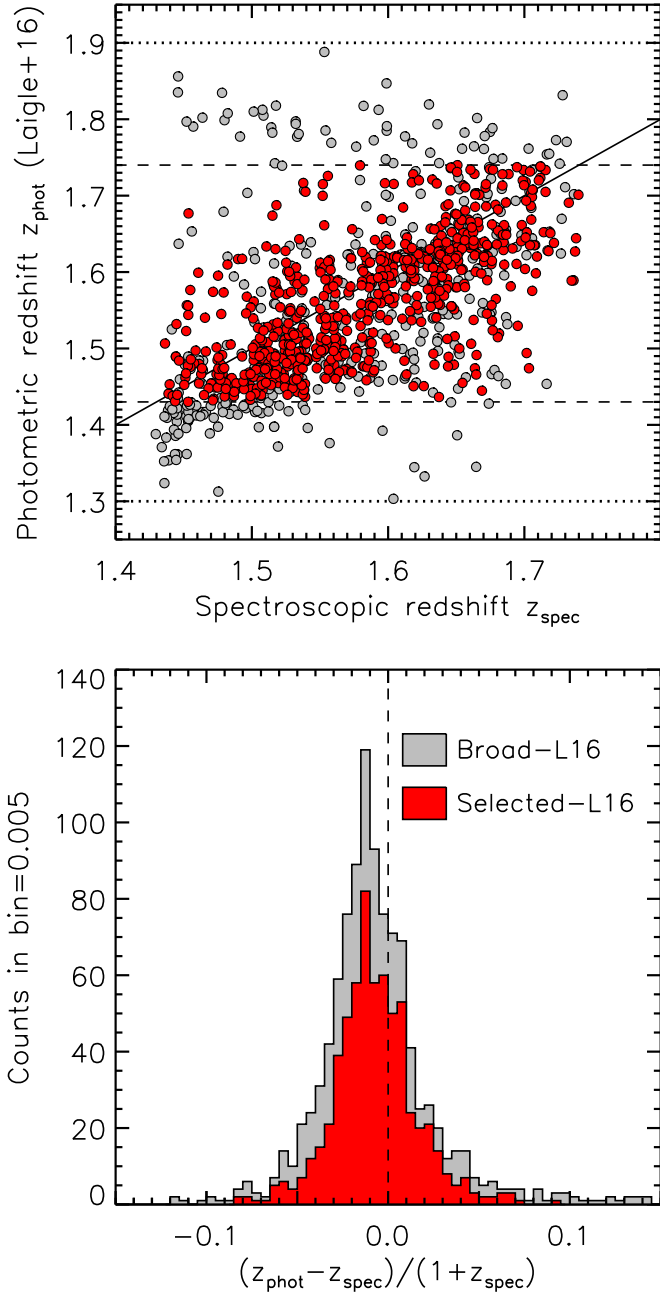


Figure 25. Upper panel: comparison of spectroscopic and photometric redshifts. Gray circles indicate the objects in the Broad-L16 sample, while red circles indicate the objects in the Selected-L16 sample. The solid line indicates the one-to-one relation. Horizontal dotted and dashed lines indicate the imposed limits on the photometric redshifts: $1.3 \leq z_{\text{phot}} \leq 1.9$ for Broad-L16 and $1.43 \leq z_{\text{phot}} \leq 1.74$ for Selected-L16. Lower panel: distribution of $(z_{\text{phot}} - z_{\text{spec}})/(1 + z_{\text{spec}})$ from the upper panel. Gray and red histograms indicate the objects from the Broad-L16 and Selected-L16 samples, respectively.

$\text{SFR}_{\text{H}\alpha}^{\text{uncorr}}$ following Equation (6) without the extinction term, and aperture correction is applied. The values of $E_{\text{star}}(B - V)$ were estimated from the UV slope β_{UV} using the Calzetti et al. (2000) law (Section 9.2).

In Figure 29, we plot the ratio $\text{SFR}_{\text{H}\alpha}^{\text{uncorr}}/\text{SFR}_{\text{UV}}^{\text{uncorr}}$ as a function of $E_{\text{star}}(B - V)$. There is a clear correlation between the SFR ratio and reddening. It is apparent that more than half the data points fall above the line with the conventional value

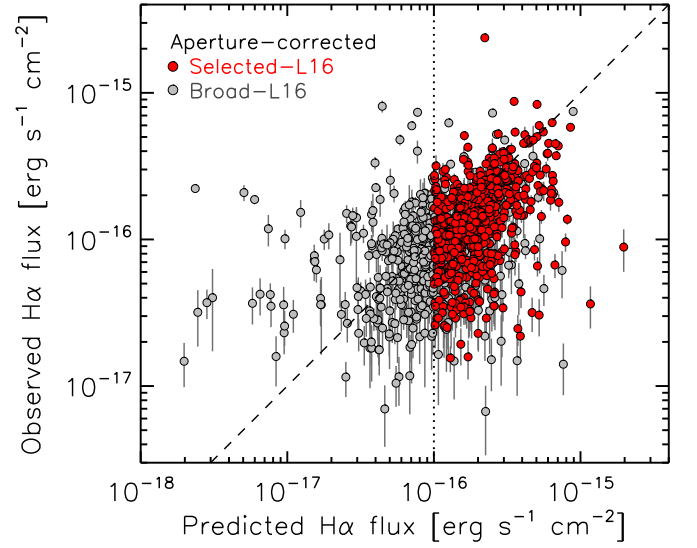


Figure 26. Observed (aperture-corrected) vs. predicted $\text{H}\alpha$ flux. Gray circles indicate objects in the Broad-L16 sample, while red circles indicate objects in the Selected-L16 sample. No error estimates are given for the predicted $\text{H}\alpha$ flux. The vertical dotted line indicates the threshold $F_{\text{H}\alpha}^{\text{pred}} = 10^{-16} \text{ erg s}^{-1} \text{ cm}^{-2}$ for the Selected-L16 sample, and the dashed line indicates the one-to-one relation.

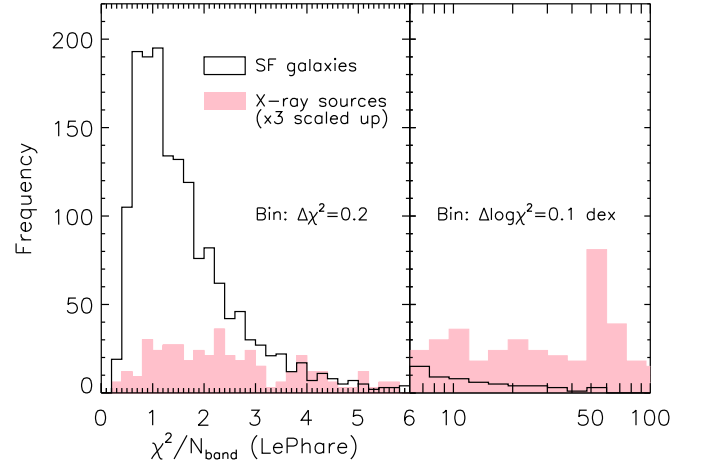


Figure 27. Histograms of χ^2/N_{band} values for the best-fit SEDs. For non-X-ray sources, the values are concentrated around $\chi^2/N_{\text{band}} = 1$ (open histogram), indicating that the fitting is successful for the majority of the sample. In contrast, for X-ray sources, the values are widely spread out to ~ 100 (filled histogram; $\times 3$ scaled up for display purpose), indicating a large fraction of those for which the fitting has failed (see text).

$f_{\text{neb}} = 0.44$ for local galaxies. We found that the best fit of Equation (10) yields a value of $f_{\text{neb}} = 0.53 \pm 0.01$, with a scatter of 0.15 dex after accounting for the individual errors. Using the Calzetti et al. (2000) curve for both stellar and nebular reddening (i.e., replacing $k_{\text{H}\alpha}$ with 3.33) results in a higher value ($f_{\text{neb}} = 0.69$), which is in agreement with Kashino et al. (2013), where we did so.

Lastly, we compare in Figure 30 the different SFR indicators: the rest-frame UV, $\text{H}\alpha$, and those obtained from the SED fitting (i.e., the same procedure with LePhare as for the stellar mass). Because the f_{neb} factor is adjusted so that the $\text{H}\alpha$ -based SFR matches the UV-based SFR, on average, these two SFRs show good agreement. In contrast, we find a systematic offset (median 0.4 dex) in comparison with the SFR

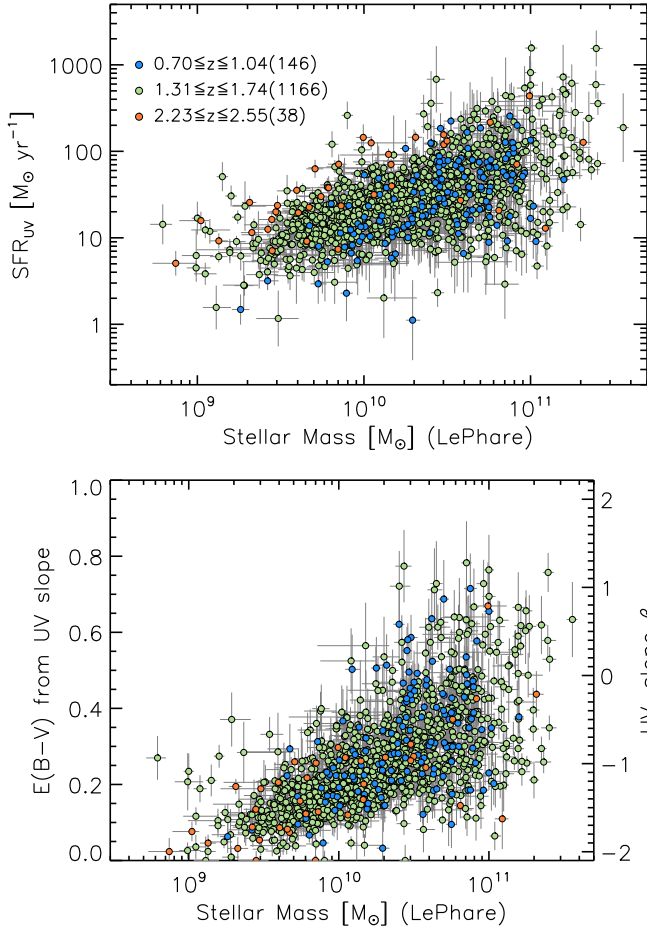


Figure 28. The M_* vs. SFR_{UV} (upper panel) and $E_{\text{star}}(B - V)$ (lower panel) estimated from the rest-frame UV continuum. The FMOS galaxies are divided into three redshift intervals, as labeled. The numbers of objects shown here are indicated in parentheses.

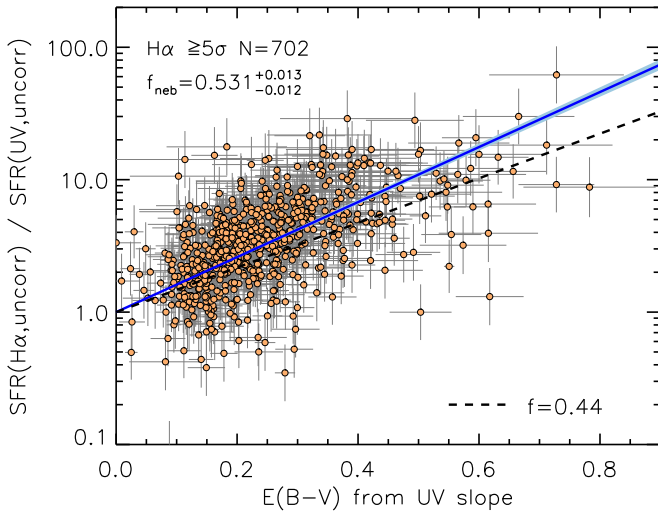


Figure 29. Ratio of $\text{H}\alpha$ - and UV-based dust-uncorrected SFRs as a function of $E_{\text{star}}(B - V)$. The $\text{H}\alpha$ -based SFRs are corrected for aperture loss. The solid line indicates the best-fit regression expressed by Equation (10) with $f_{\text{neb}}^{\text{best}} = 0.53 \pm 0.01$. The dashed line indicates the relation with $f_{\text{neb}} = 0.44$.

through the SED fitting. Similarly, some bias (~ 0.25 dex) was found by Ilbert et al. (2015) from a comparison with SFR from IR+UV flux.

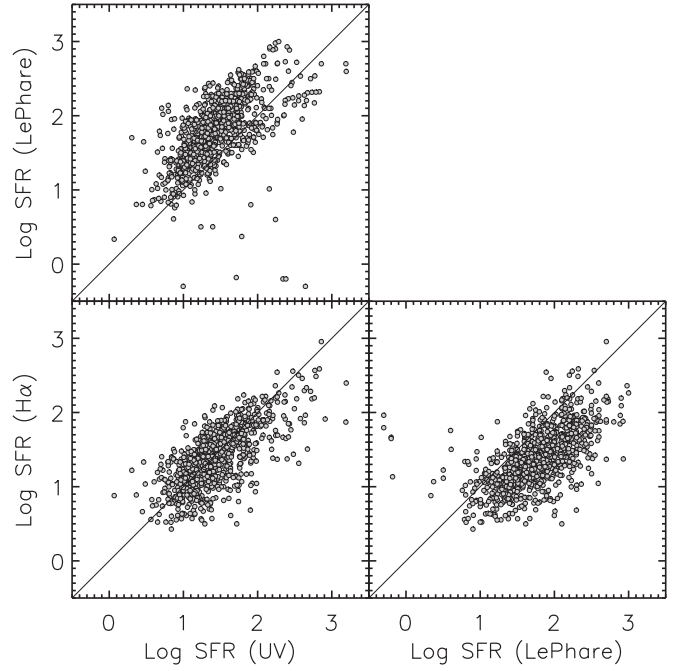


Figure 30. Comparison of SFR estimates obtained from the rest-frame UV luminosity, $\text{H}\alpha$ luminosity, and through the SED fitting with LePhare. Diagonal lines indicate a one-to-one relation.

10. The Stellar Mass–SFR Relation, Revisited

Star-forming galaxies are known to form a tight sequence in the M_* –SFR plane, which is referred to as the main sequence of star-forming galaxies (Noeske et al. 2007). It has been established that the normalization of the sequence increases with increasing redshift up to $z \sim 4$ or more (e.g., Speagle et al. 2014). However, the normalization and slope vary from one study to another, depending on the sample selection and the methodology of the M_* and SFR estimation (e.g., Rodighiero et al. 2014). Moreover, there have also been studies of a possible bending feature seen at $\log(M_*/M_\odot) \approx 10$ – 10.5 (e.g., Karim et al. 2011; Whitaker et al. 2014; Lee et al. 2015; Schreiber et al. 2015).

In Kashino et al. (2013), we established the main sequence at $z \sim 1.6$ based on the $\text{H}\alpha$ -based SFRs using 271 *sBzK*-selected galaxies, a subset of the FMOS-COSMOS galaxy sample. In this section, we redefine the main sequence based on the $\text{H}\alpha$ -based SFRs by using the complete FMOS-COSMOS sample and discuss the bending feature and the intrinsic scatter of the main sequence.

10.1. Stellar Mass versus $\text{H}\alpha$ -based SFR

In Figure 31, we show 907 galaxies with an $\text{H}\alpha$ detection ($\geq 3\sigma$) in the H -long spectral window. Of them, 702 galaxies have an $\text{H}\alpha$ detection at $\geq 5\sigma$ (cyan circles). Observed $\text{H}\alpha$ fluxes are corrected for dust extinction by using $A_{\text{H}\alpha} = 2.54E_{\text{star}}(B - V)/0.53$ (see Section 9.3). Vertical error bars include in quadrature the individual formal errors on the flux measurements (i.e., errors from line fitting) and a common uncertainty of 0.17 dex for aperture correction (see Section 4.5), as well as individual measurement errors on $E_{\text{star}}(B - V)$, while not including any systematic uncertainty in the extinction law. The average detection limit is estimated by assuming the 3σ detection limit of $\text{H}\alpha$ flux of $6 \times 10^{-18} \text{ erg s}^{-1} \text{ cm}^{-2}$ (see Figure 12) and taking into account the M_* -dependent aperture

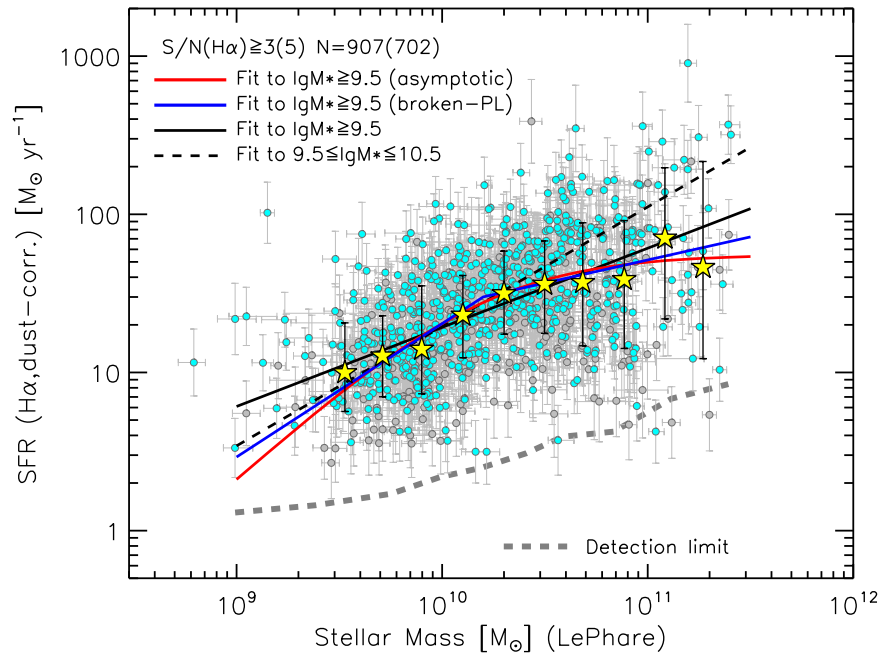


Figure 31. Stellar mass vs. SFR from the observed $H\alpha$ fluxes corrected for dust extinction and aperture loss. Shown are 907 objects with a detection of $H\alpha$ ($\geq 3\sigma$) in the FMOS H -long, separated by their S/N (gray circles, $3.0 \leq S/N < 5.0$; cyan circles, $S/N \geq 5.0$ ($N = 702$); X-ray objects are excluded). Yellow stars indicate the median $H\alpha$ -based SFRs in M_* bins from $10^{9.4}$ to $10^{11.4} M_\odot$ with a constant interval of 0.2 dex, with the central 68th percentiles indicated by the vertical error bars. Black solid and dashed lines indicate a linear regression of our data limited to $M_* \geq 10^{9.5} M_\odot$ and $10^{9.5} \leq M_*/M_\odot \leq 10^{10.5}$, respectively. Blue and red solid lines indicate the best fits with a broken power law (Equation (12)) and an asymptotic function (Equation (13)). A thick gray dashed line indicates the typical detection limit, accounting for the dust extinction and aperture correction.

correction and dust extinction. The detection limit increases with M_* , mainly because the level of extinction increases on average with M_* (see the lower panel of Figure 28). The observed data points are well above this line across the whole M_* range, indicating that the observed distribution of SFR at fixed M_* is less biased by the detection limit.

The correlation between M_* and SFR is evident. The Spearman’s rank correlation coefficient is $\rho = 0.52$ for all objects with $S/N(H\alpha) \geq 3.0$ shown here. To illustrate the behavior of the observed sequence more clearly, we separated the data points into bins of M_* from $10^{9.4}$ to $10^{11.4} M_\odot$ with a constant interval of 0.2 dex. In Figure 31, we indicate the median values and the central 68th percentiles in each bin. These median points indicate possible bending of the main sequence, as reported by several authors (e.g., Whitaker et al. 2014; Lee et al. 2015; Schreiber et al. 2015).

We parameterize the observed M_* -SFR relation. In doing so, we exclude the objects below $10^{9.5} M_\odot$ and use the individual points, taking into account errors on both $\log M_*$ and \log SFR. We first employ a power-law function to fit the data as follows:

$$\log \text{SFR}/(M_\odot \text{ yr}^{-1}) = \alpha + \beta \log \left[\frac{M_*}{10^{10} M_\odot} \right]. \quad (11)$$

We fit to two subsamples: one contains all 876 galaxies above $M_* \geq 10^{9.5} M_\odot$, and the other is limited to 609 objects in the range $10^{9.5} \leq M_*/M_\odot \leq 10^{10.5}$ to avoid the effect of the possible bending. We summarize the results in Table 9 and indicate the best-fit relations in Figure 31. The best-fit relation for the former ($M_* \geq 10^{9.5} M_\odot$) has a slope of $\beta = 0.500 \pm 0.017$, which is shallower than the slope of $\beta = 0.755 \pm 0.035$

for the latter subsample limited to $10^{9.6} \leq M_*/M_\odot \leq 10^{10.5}$. Hence, it is obvious that the shallower slope is caused by the massive population.

We next account for the bending feature of the M_* -SFR relation at $M_* \sim 10^{10.5} M_\odot$. We employ two functional forms, a broken power law and an asymptotic function, proposed by Whitaker et al. (2014) and Lee et al. (2015), respectively. The broken power law is parameterized as

$$\log \text{SFR}/(M_\odot \text{ yr}^{-1}) = a(\log M_*/M_\odot - 10.2) + b, \quad (12)$$

where the value of a is different above (a_{high}) and below (a_{low}) the characteristic mass of $\log M_*/M_\odot = 10.2$. The characteristic mass is fixed following the original paper (Whitaker et al. 2014), though the best-fit value is $\log M_*/M_\odot = 10.31 \pm 0.04$ if we allow it to vary. The asymptotic function is defined as

$$\log \text{SFR}/(M_\odot \text{ yr}^{-1}) = \mathcal{S}_0 + \log \left[1 + \left(\frac{M_*}{\mathcal{M}_0} \right)^{-\gamma} \right], \quad (13)$$

where \mathcal{S}_0 is the asymptotic value of the \log SFR at high M_* , \mathcal{M}_0 is the characteristic mass for turnover, and γ is a low-mass slope.

Table 9 gives the results of fits to the individual objects with $M_* \geq 10^{9.5} M_\odot$. With the asymptotic relation, the characteristic mass for turnover is constrained to be $\log \mathcal{M}_0/M_\odot = 10.205 \pm 0.068$, which is fully consistent with the fixed characteristic mass ($\log M_*/M_\odot = 10.2$) of the broken power-law fit, as well as the result of Lee et al. (2015), as discussed below. In Figure 31, we show the best fits with the broken power law and asymptotic function. The two functional forms yield almost identical M_* -SFR relations across the M_* range probed, which both well fit the median SFRs.

Table 9
Best-fit Parameters for the M_* -SFR Relation

Parameters	N	Parameters	χ^2 (χ^2/dof) ^a
Power law (Equation (11))		α	
$M_*/M_\odot \geq 10^{9.5}$	876	1.285 ± 0.008	2261 (2.59)
$10^{9.5} \leq M_*/M_\odot \leq 10^{10.5}$	609	1.290 ± 0.009	1187 (1.95)
Broken power law (Equation (12))		a_{low}	
$M_*/M_\odot \geq 10^{9.5}$	876	0.844 ± 0.055	2200 (2.52)
Asymptotic function (Equation (13))		$\log \mathcal{M}_0$	
$M_*/M_\odot \geq 10^{9.5}$	876	1.74 ± 0.033	2206 (2.53)

Note.

^a The χ^2 statistics are computed including errors on both log SFR and log M_* . The dof is $N - n_p$, where n_p is the number of parameters.

The tight constraint on the turnover characteristic mass \mathcal{M}_0 , as well as the significant difference detected between a_{low} and a_{high} , indicate the presence of bending of the sequence at $M_* \approx 10^{10.2}$. This is also supported by the fact that, compared with the simple power law, the resultant χ^2 is reduced by $\Delta\chi^2 \approx 60$ by invoking the bending feature (Table 9). Meanwhile, there is no significant difference between the fits with the broken power law and the asymptotic function.

In Figure 32, we compare our results with the M_* -SFR relations from the literature. The power-law fit to the limited M_* range ($9.5 \leq \log M_*/M_\odot \leq 10.5$) is fully consistent with our previous result (Kashino et al. 2013) and the parameterization from a compilation across a wide redshift range derived by Speagle et al. (2014). On the other hand, fit to the entire M_* range ($\log M_*/M_\odot \geq 9.5$) yields a shallower slope. The difference with Kashino et al. (2013) may be attributed to the increased weight of the massive population and their different sample selection. The broken power-law fit to the FMOS data yields a shallower high-mass slope ($a_{\text{high}} = 0.29$) than the result from Whitaker et al. (2014; $a_{\text{high}} = 0.62$ for a sample at $1.5 < z < 2.0$). In contrast, the best fit with the asymptotic function (Equation (13)) is in good agreement with the result with the same parameterization by Lee et al. (2015) at $\langle z \rangle = 1.19$, with a similar characteristic mass $\log \mathcal{M}_0 (= 10.31)$ for the turnover. Lee et al. (2015) also found a high-mass power-law slope of 0.27 for $M_* > 10^{10} M_\odot$, which is rather similar to our $a_{\text{high}} (= 0.29)$. The steeper high-mass slope found by Whitaker et al. (2014) may be attributed, at least partially, to the fact that the authors derived the total SFR using IR luminosity estimated from *Spitzer*/MIPS 24 μm flux with a luminosity-independent conversion. Lee et al. (2015) showed that total SFRs estimated in this way are overestimated at $\log \text{SFR}/(M_\odot \text{ yr}^{-1}) \gtrsim 2$. This effect is thus more important at high masses and would artificially make the high-mass slope steeper.

10.2. Scatter of the M_* -SFR Relation

In Figure 31, the observed scatter in $\text{SFR}_{\text{H}\alpha}$ appears to increase with M_* . We estimate the intrinsic scatters of the M_* -SFR relation as a function of M_* . For this purpose, we define the offset from the best-fit M_* -SFR relation at fixed M_* as $\log \text{sSFR}/\langle \text{sSFR} \rangle$ and divide the sample into four bins of M_* : $\log M_*/M_\odot = [9.4:9.9]$, $[9.9:10.4]$, $[10.4:10.7]$, and $[10.7:11.5]$. Here we use the best fit with the asymptotic function (Equation (13)), but the use of another fit (i.e., simple or broken power-law fit for $M_* \geq 10^{9.5} M_\odot$) does not change the conclusions.

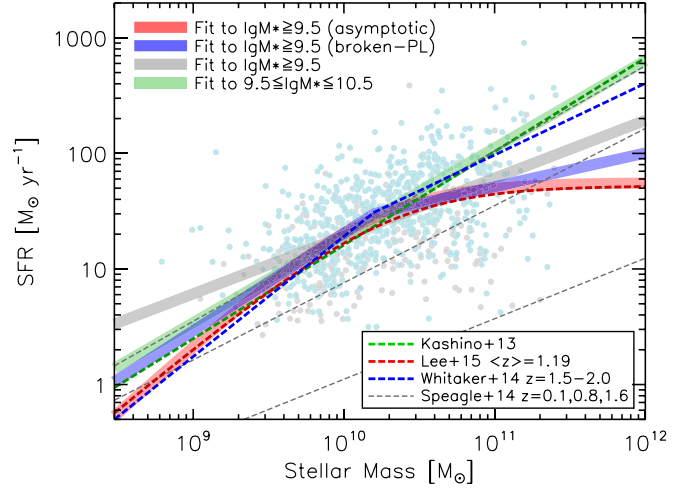


Figure 32. Best-fit M_* vs. SFR relations for the FMOS objects, in comparison to literature measurements. Pale colored circles indicate FMOS objects (same as in Figure 31). Thick solid curves indicate the best-fit relations to the FMOS data: power-law fits to objects with $\log M_*/M_\odot \geq 9.6$ (gray) and $9.6 \leq \log M_*/M_\odot \leq 10.6$ (green), asymptotic function fit (red), and broken power-law fit (blue). Colored dashed lines indicate literature measurements: fit to a subset of the FMOS sample (Kashino et al. 2013; green), broken power-law fit at $1.5 \leq z \leq 2.0$ from Whitaker et al. (2014; blue), and asymptotic function fit at median $\langle z \rangle = 1.19$ from Lee et al. (2015; red). Three dashed gray lines indicate an empirically parameterized relation at $z = 0.1, 0.8,$ and 1.6 (top to bottom) derived by Speagle et al. (2014).

Figure 33 shows the distributions of $\log \text{sSFR}/\langle \text{sSFR} \rangle$ for the entire sample and in the four M_* bins. These distributions are well fit with a lognormal profile (solid blue lines). The standard deviations of these lognormal profiles (σ_{gaus}) and the values directly computed from the sample after 3σ clipping (σ_{std}) are indicated in each panel, which agree with each other.

The intrinsic scatter is then estimated from σ_{std} by accounting for the individual uncertainties on $\log M_*$ and $\log \text{SFR}$. The individual errors were obtained by summing in quadrature the statistical uncertainties on the individual H α -based SFR (the formal errors), $\log M_*$, and a common 0.17 dex for aperture correction. The uncertainty on $\log M_*$ was included by multiplying it by the slope of the relation at a given M_* . Systematic uncertainties and the error on $f_{\text{neb}} = 0.53$ were not included. We also deconvolved the effect of the time evolution of the average sSFR across $1.43 \leq z \leq 1.74$ (≈ 0.04 dex) by using the actual redshift distribution of the sample. We adopted the scaling relation $\text{sSFR} \propto (1+z)^{3.14}$ from Ilbert et al. (2015).

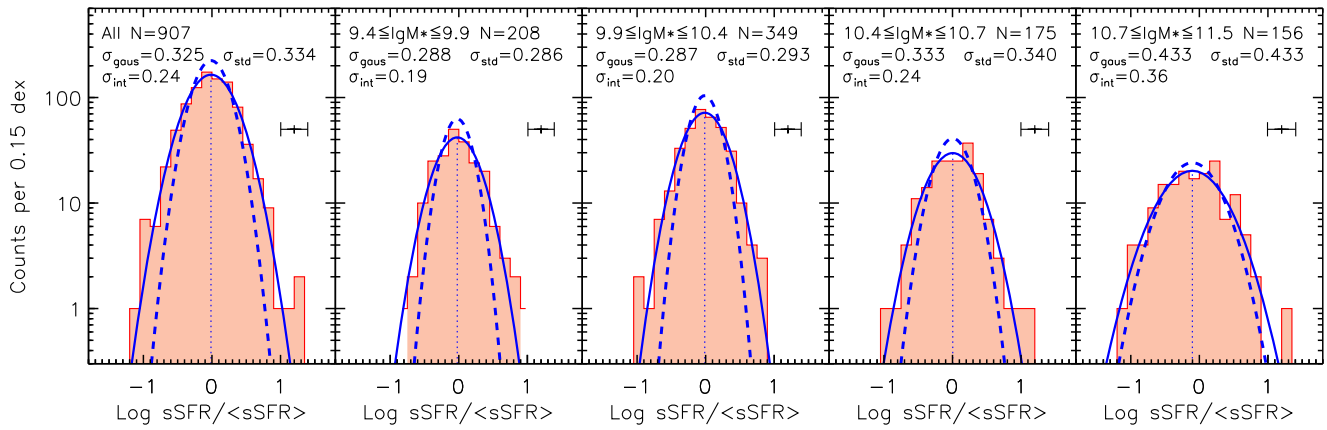


Figure 33. Distribution of $\log s\text{SFR}/\langle s\text{SFR} \rangle$ in bins of stellar mass: the entire M_* range and $\log M_*/M_\odot = [9.4:9.9]$, $[9.9:10.4]$, $[10.4:10.7]$, and $[10.7:11.5]$ (left to right). The average $\langle s\text{SFR} \rangle$ is taken from the best fit with the asymptotic function (Equation (13)) at each M_* . Blue solid lines indicate the best-fit functions assuming a lognormal profile with mean values indicated by vertical dotted lines. Blue dashed lines indicate lognormal functions with the estimated intrinsic scatter (σ_{int}). The median error of $\text{SFR}_{\text{H}\alpha}$ in each bin is indicated by a horizontal error bar in each panel.

We found the intrinsic scatter to be 0.24 dex for the entire sample and found it to increase with M_* from 0.19 to 0.37 dex in the four bins shown in Figure 33. The intrinsic scatter in $s\text{SFR}/\langle s\text{SFR} \rangle$ found at low-to-intermediate masses is in good agreement with previous constraints of the width of the main sequence (≈ 0.2 dex; e.g., Salmi et al. 2012; Speagle et al. 2014). Noeske et al. (2007) obtained an observed value of 0.35 dex and put an upper limit of < 0.30 dex on the intrinsic scatter. It is also argued that the scatter around the main sequence is nearly redshift-independent across a wide redshift range ($0 \leq z \lesssim 4$; e.g., Speagle et al. 2014; Ilbert et al. 2015; Schreiber et al. 2015). Ilbert et al. (2015) parameterized the $s\text{SFR}$ function in the M_* bins with a lognormal function convolved with the measurement uncertainties and found the intrinsic scatter to be ≈ 0.28 – 0.46 dex, increasing with M_* . The M_* dependence they found is qualitatively consistent with our result, while the scatter they found is larger than our findings at all masses.

Ilbert et al. (2015) argued that, as a caveat, the dynamical range of $s\text{SFR}$ covered by the data may be not enough large in many cases to correctly estimate the width of the main sequence. Indeed, in our case, the criterion on the predicted $\text{H}\alpha$ flux in the preselection of the spectroscopic targets reduces the sampling rate, especially of a population with low M_* and SFR (see Section 3.1). Figure 2 shows that this selection bias exists across the whole M_* range, while being mitigated more or less at $M_* \gtrsim 10^{10.7} M_\odot$. Establishing the main sequence based on $\text{H}\alpha$ at high redshifts may require further unbiased deep spectroscopic surveys with high multiplicity, which will finally be achieved by upcoming projects and instruments, such as the Multi-Object Optical and Near-infrared Spectrograph (MOONS).

11. Emission-line Ratio Diagnostics, Revisited

In Kashino et al. (2017b), we extensively investigated the physical conditions of the ionized gas in star-forming galaxies at $z \sim 1.6$ from the FMOS-COSMOS survey. We utilized various commonly used emission-line ratio diagnostics, such as the Baldwin–Phillips–Terlevich (BPT; Baldwin et al. 1981; see also Veilleux & Osterbrock 1987) diagram. Hereafter, we refer to the $[\text{N II}]/\text{H}\alpha$ -versus- $[\text{O III}]/\text{H}\beta$ plot as the N2-BPT diagram and the $[\text{S II}]/[\text{N II}]$ -versus- $[\text{O III}]/\text{H}\beta$ plot as the S2-BPT

diagram. We confirmed that star-forming galaxies at these redshifts have systematically larger $[\text{O III}]/\text{H}\beta$ ratios at both fixed M_* and fixed metallicity than their present-day counterparts, as was indicated by several authors (e.g., Masters et al. 2014; Steidel et al. 2014; Shapley et al. 2015). In this section, we revisit these diagnostic diagrams to confirm the average emission-line properties based on the final FMOS catalog.

11.1. Sample Definition

For the following exercises, we selected galaxies in a similar way to Kashino et al. (2017b), as follows. The sample is limited to having a detection of $\text{H}\alpha$ at $\geq 3\sigma$ in the H -long band and a stellar mass estimate (see Section 9). Any objects, either detected in the X-ray or with the FWHM of $\text{H}\alpha$ greater than 1000 km s^{-1} , are removed from the sample. Furthermore, we removed a fraction of the individual galaxies as possible AGNs by using their observed emission-line ratios, $\text{H}\alpha/[\text{N II}]$, and $[\text{O III}]/\text{H}\beta$. We excluded objects that are located above the theoretical “maximum starburst” line derived by Kewley et al. (2001) or have a line ratio of $\log [\text{N II}] \lambda 6584/\text{H}\alpha \geq -0.1$ or $\log [\text{O III}] \lambda 5007/\text{H}\beta \geq 0.9$.

Finally, we have 907 galaxies, which are referred to as *Sample-H*. Of these, there are 648 galaxies that have both a redshift in the range $1.43 \leq z_{\text{spec}} \leq 1.67$ and J -long coverage, which are referred to as *Sample-HJ*. For *Sample-HJ*, the upper limit of the redshift range is slightly decreased to ensure that all of the key emission lines, including $[\text{S II}] \lambda \lambda 6717, 6731$, fall within the wavelength ranges of the FMOS H -long and J -long windows. In Table 10, we summarize the number of galaxies and line detections in each subsample. We group the galaxies by the S/N of their emission-line detections: high quality (HQ) if $\text{S/N} \geq 5$ for $\text{H}\alpha$ and $\text{S/N} \geq 3$ for other lines, and low quality (LQ) if $3 \leq \text{S/N} < 5$ for $\text{H}\alpha$ and $1.5 \leq \text{S/N} < 3$ for other lines. The typical range of the stellar mass is $\log M_*/M_\odot \approx 9.46$ – 11.17 (the central 95th percentiles). Note that the sizes of *Sample-H* and *Sample-HJ* increase by 265 and 365, respectively, relative to the corresponding samples in Kashino et al. (2017b).

Both individual and stacked measurements were corrected for the Balmer absorption for the $\text{H}\beta$ line as a function of M_*

Table 10Summary of Emission-line Detections for the Samples Used in Section 11^a

Samples	Sample-H ^b	Sample-HJ ^c
z_{spec} range	$1.43 \leq z \leq 1.74$	$1.43 \leq z \leq 1.67$
Median z_{spec}	1.579	1.557
H α	907 (702)	648 (506)
[N II]	551 (347)	419 (272)
[S II]	72 (19)	62 (17)
H β	...	203 (136)
[O III]	...	242 (220)
H α + [N II] ^d	551 (325)	419 (254)
H α + [S II]	72 (18)	62 (16)
[O III] + H β	...	170 (114)
H α + [N II] + [O III] + H β	...	118 (59)
H α + [S II] + [O III] + H β	...	19 (6)

Notes.

^a The threshold S/N is 3 for H α and 1.5 for other lines. In parentheses, the numbers of detections with higher S/N (≥ 5 for H α and ≥ 3 for other lines) are listed.

^b Sample-H consists of 907 galaxies with H α ($\geq 3\sigma$).

^c Sample-HJ consists of 648 galaxies with both H α ($\geq 3\sigma$) and the additional J-long coverage.

^d The numbers of galaxies with multiple emission-line detections are listed in the 8th–12th rows.

and SFR by using a relation as follows (Kashino & Inoue 2018):

$$\frac{F_{\text{H}\beta}^{\text{int}} - F_{\text{H}\beta}^{\text{obs}}}{F_{\text{H}\beta}^{\text{int}}} = \frac{1}{2} [\text{erf}(-0.626(x + 0.248)) + 1], \quad (14)$$

where

$$x = \log \text{SFR} / (M_{\odot} \text{ yr}^{-1}) - 1.32(\log M_{*} / M_{\odot} - 10). \quad (15)$$

For this equation, we used M_{*} from SED fitting and SFR_{UV} (Section 9) and substituted the median values in each bin for stacked measurements. Although the H α fluxes were not corrected for the Balmer absorption following our previous study (Kashino et al. 2017b), the effects ($\lesssim 3\%$) do not alter the conclusions.

For comparison, we extracted a sample of local galaxies from the SDSS. The stellar mass and SFR from the MPA-JHU catalog (Kauffmann et al. 2003b; Brinchmann et al. 2004; Salim et al. 2007) are converted to a Chabrier IMF to match our sample. We divided the galaxies into two categories—star-forming and AGN—by using the Kauffmann et al. (2003a) classification line in the BPT diagram and excluded AGNs from the sample for the following analysis. The SDSS comparison sample consists of 80,003 star-forming galaxies in the range $0.04 \leq z \leq 0.10$. To illustrate the average relation between line ratios and stellar masses of local star-forming galaxies, we split the sample into bins of M_{*} in the range $10^{8.6} \leq M_{*} \leq 10^{11.2}$ with a bin size of 0.2 dex and computed the pseudo-stacked line ratios from the mean line fluxes in each bin (see Kashino et al. 2017b). We refer the reader to Kashino et al. (2017b) for a full description of the sample construction of local galaxies.

11.2. N2-BPT and S2-BPT Diagrams

Figure 34 shows FMOS galaxies in the N2-BPT diagram, in comparison with the SDSS galaxies and average locations of samples at higher redshifts from the literature (Shapley et al. 2015;

Strom et al. 2017). The distribution of the SDSS galaxies is represented by the red contour that encloses 95% of the sample.

As we originally reported in Kashino et al. (2017b), star-forming galaxies at $z \sim 1.6$ in the FMOS sample are located, on average, offset from the sequence of the SDSS galaxies. The N2-BPT locus of our FMOS galaxies can be described empirically using a simple functional form. We fit the individual galaxies with detection of all four lines ($N = 118$; $S/N \geq 3.0$ for H α and ≥ 1.5 for others). The best-fit curve for the locus of the FMOS galaxies (green line in Figure 34) takes the form of

$$\log([\text{O III}]/\text{H}\beta) = \frac{0.61}{\log([\text{N II}]/\text{H}\alpha) - (0.13 \pm 0.03) + (1.09 \pm 0.04)}, \quad (16)$$

where the coefficient is fixed to 0.61 (Kewley et al. 2001). Here we accounted for the errors on both line ratios simultaneously.

The offset is further clearly seen by comparing the stacked line ratios between the FMOS (blue circles) and SDSS (yellow squares) samples. The FMOS stacked points are located along the upper envelope of the red contour and in agreement with the best-fit curve to the individual galaxies.

Figure 35 shows the S2-BPT diagram that replaces the x -axis of the N2-BPT diagram with the [S II]/H α ratio. While the [S II] lines are not detected for the majority of the individual galaxies, it is evident that the stacked measurements certainly differ from the average locus of the local galaxies. The data points of the high- M_{*} bins are located near the left-hand envelope of the red contour that encloses 95% of the SDSS sample.

We previously reported the possible offset of the high- z galaxies toward the left-hand side of the diagram, i.e., lower [S II]/H α at fixed [O III]/H β , and we regarded this offset as a key observational feature to support our hypothesis that an increase in the ionization parameter is the primary origin of the evolution of the observed emission-line ratios (see Figure 12 of Kashino et al. 2017b). Our larger sample in this paper confirmed the offset toward a lower [S II]/H α ratio at $\log [\text{O III}]/\text{H}\beta \sim 0$ in higher M_{*} bins ($M_{*} \gtrsim 10^{10.3} M_{\odot}$).

11.3. Stellar Mass–Excitation Diagram

In Figure 36, we show the [O III] $\lambda 5007/\text{H}\beta$ ratio as a function of M_{*} for both FMOS Sample-HJ and the local SDSS sample. This is known as the mass–excitation (MEx) diagram (Juneau et al. 2011). It is clear that the FMOS galaxies occupy a region distinct from the local galaxies, well above the upper envelope of the red contour enclosing 95% of the local sample. Across the entire M_{*} range probed, the line ratio increases at fixed M_{*} by ≈ 0.5 dex, from $z \sim 0.1$ to 1.6. Similar to the SDSS sample, the FMOS galaxies exhibit an inverse correlation between [O III]/H β and M_{*} . We derived a linear fit to the locus of the FMOS galaxies while limiting to 170 galaxies in Sample-HJ having both H β and [O III] detections ($\geq 1.5\sigma$). The best-fit relation (solid green line in Figure 36) is given as

$$\log([\text{O III}]/\text{H}\beta) = 0.23 - 0.54 \times [\log M_{*} / M_{\odot} - 10]. \quad (17)$$

The stacked measurements in five M_{*} bins are in good agreement with the best-fit relation. With respect to the best-fit linear relation, the intrinsic scatter is found to be $\sigma_{\text{int}} = 0.17$

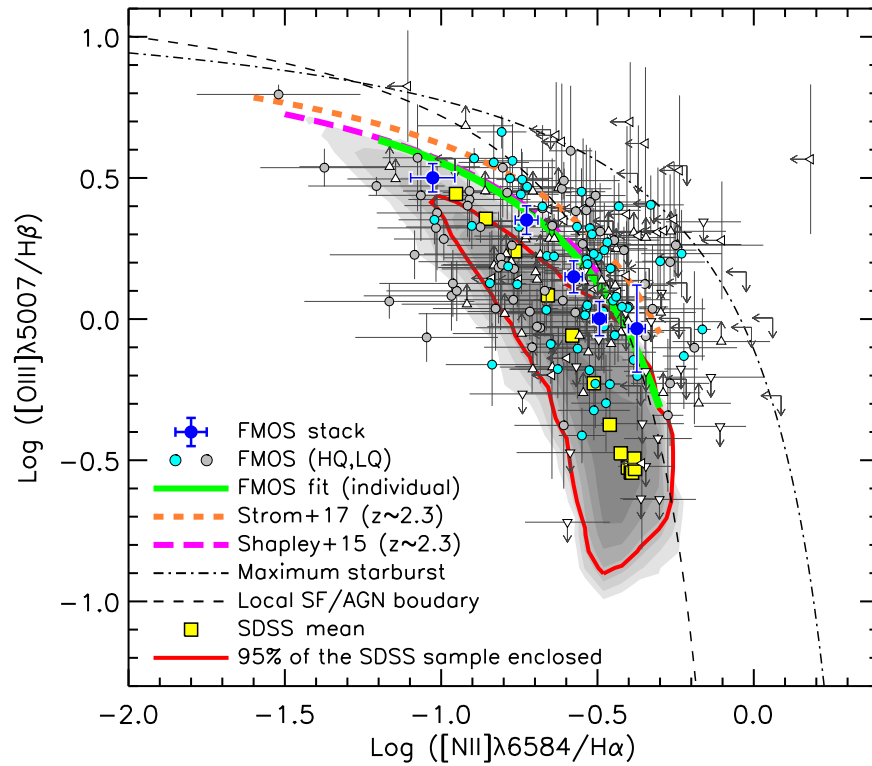


Figure 34. The N2-BPT diagram: $\log [N II] \lambda 6584/H\alpha$ vs. $\log [O III] \lambda 5007/H\beta$. The FMOS galaxies in Sample-HJ are plotted. Objects with detections of all four lines are shown with circles and divided into two groups: HQ (cyan) and LQ (gray). For other objects, the arrows and triangles indicate the 2σ upper and/or lower limits. Large blue circles indicate the FMOS stacked measurements in five mass bins (with the median M_* increasing from left to right). A green line indicates the best-fit curve to the FMOS galaxies (Equation (16)). The shaded contours indicate the distribution of the SDSS sample in log scale, and the red contour encloses 95% of the SDSS galaxies. Yellow squares indicate the stacked line ratios of the SDSS galaxies in bins of M_* in the range $10^{8.6} \leq M_* \leq 10^{11.2}$. Thin dashed and dot-dashed curves indicate the empirical separation between star-forming galaxies and AGNs for the SDSS sample (Kauffmann et al. 2003a) and the theoretical “maximum starburst” limit (Kewley et al. 2001), respectively. In addition, the best-fit relations at $z \sim 2.3$ are shown (orange dashed line, Strom et al. 2017; magenta dashed line, Shapley et al. 2015).

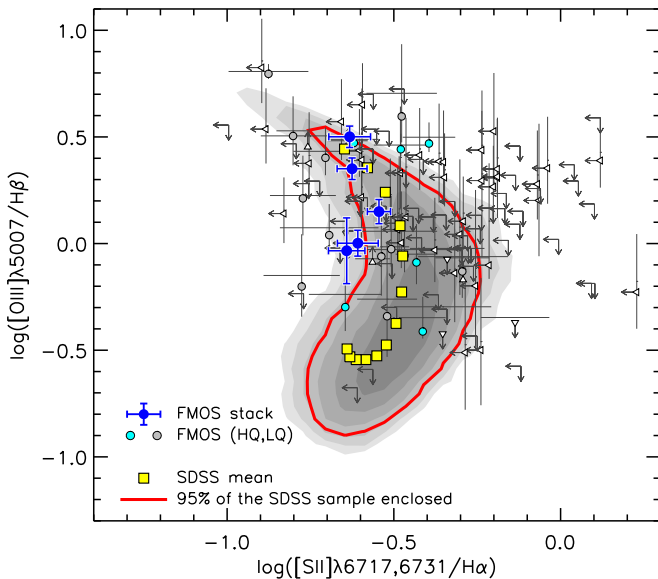


Figure 35. The S2-BPT diagram: $\log [S II] \lambda \lambda 6717, 6731/H\alpha$ vs. $\log [O III] \lambda 5007/H\beta$. The FMOS galaxies in Sample-HJ are plotted in comparison with the SDSS galaxies. Symbols are the same as in Figure 34.

(only for objects with both detections) after accounting for the individual measurements errors on $\log M_*$ and $\log [O III]/H\beta$.

For comparison, we show the best-fit linear relation to the KBSS-MOSFIRE samples at $z \sim 2.3$ (Strom et al. 2017), indicating a further increase in the emission-line ratio at fixed

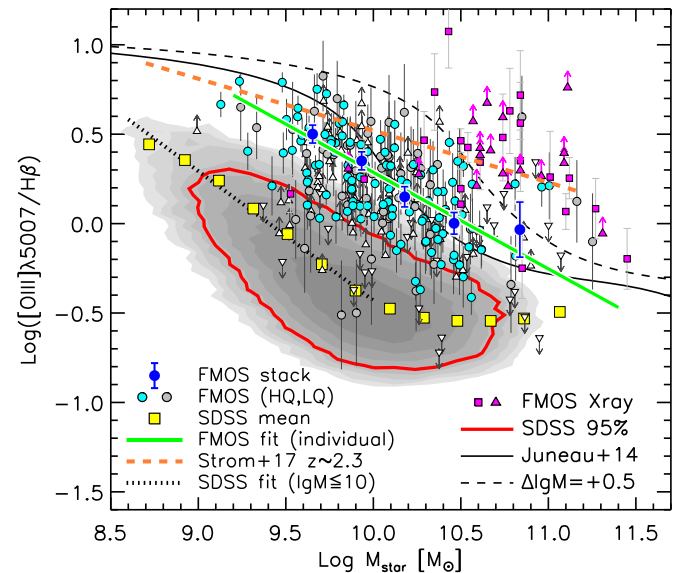


Figure 36. The MEX diagram: M_* vs. $[O III] \lambda 5007/H\beta$. The FMOS galaxies in Sample-HJ are compared with the SDSS sample. Symbols are the same as in Figure 34. The solid green line indicates the best-fit linear relation for the FMOS galaxies, and the orange dashed line is the best-fit relation for the KBSS-MOSFIRE sample at $z \sim 2.3$ (Strom et al. 2017). The thin dashed curves indicate the divisions between star-forming/composite galaxies and AGNs at $z \sim 0$ (Juneau et al. 2014).

M_* . The best-fit relation to the higher-redshift sample has a shallower slope (-0.29) than the FMOS sample at $z \sim 1.6$ due to higher ratios at high M_* . Turning to the SDSS sample, the

stacked points show a further steeper slope at lower masses. Fitting to those at $M_* \leq 10^{10} M_\odot$, we find the slope to be -0.72 . The gradual change of the slope indicates that the $[\text{O III}]/\text{H}\beta$ ratio evolves with redshift in a mass-dependent way: the more massive the systems are, the faster the $[\text{O III}]/\text{H}\beta$ decreases with redshift.

In Figure 36, we overplot the empirically calibrated division line between AGNs and star-forming (or composite) galaxies at $z \sim 0.1$ (solid black line; Juneau et al. 2014). It is clear that the majority of the FMOS galaxies are located above this classification line. For comparison to the star-forming population, Figure 36 shows X-ray AGNs at $z \sim 1.6$ from the full FMOS catalog. For these X-ray-detected objects, we estimated stellar masses using the SED3FIT package (Berta et al. 2013) based on the MAGPHYS software (da Cunha et al. 2008), including the emission from an AGN torus (a full analysis of the SEDs of X-ray sources is presented in D. Kashino et al. 2019, in preparation). These objects tend to have even higher $[\text{O III}]/\text{H}\beta$ ratios than the star-forming population at fixed M_* , while roughly one-third of them are virtually mixed with the star-forming population. We found that shifting the division line in the MEx diagram by $\Delta \log M_* = +0.5$ dex yields a reasonable classification between the star-forming galaxies and X-ray sources (dashed black line in Figure 36). This is in agreement with the luminosity-dependent offset modeled by Juneau et al. (2014; see Appendix B) for the threshold luminosity of the FMOS sample, which is $L_{\text{H}\alpha}^{\text{thresh}} \approx 10^{41.5} \text{ erg s}^{-1}$ (see Figure 15). Coil et al. (2015) found that a shift of $+0.75$ dex in M_* is required to purely distinguish AGNs from star-forming galaxies at $z \sim 2.3$ using the MOSDEF survey (Kriek et al. 2015), while recently, Strom et al. (2017) argued that an even larger shift (~ 1 dex) is needed for the KBSS-MOSFIRE sample.

11.4. Stellar Mass versus $[\text{N II}]/\text{H}\alpha$

In Figure 37, we show the observed $[\text{N II}] \lambda 6584/\text{H}\alpha$ ratios as a function of M_* for the FMOS Sample-H and the local SDSS sample. We plot 557 galaxies with both $\text{H}\alpha$ and $[\text{N II}]$ detections, divided into two groups: HQ objects ($N = 325$; cyan circles) if $S/N(\text{H}\alpha) \geq 5$ and $S/N([\text{N II}]) \geq 3$ and LQ objects ($N = 226$; gray circles) if $S/N(\text{H}\alpha) \geq 3$ and $S/N([\text{N II}]) \geq 1.5$. For others, the upper limits are shown by downward arrows. The region occupied by the FMOS galaxies is largely overlapped with the locus of the SDSS sample, while a number of objects have a lower $[\text{N II}]/\text{H}\alpha$ ratio than the lower envelope of the red contour enclosing 95% of the SDSS sample. The stacked measurements (large blue circles), however, are clearly off from the average locus of the SDSS galaxies. The amount of the offset is a strong function of M_* , from ≥ 0.5 dex at $M_* \sim 10^{9.7} M_\odot$ to < 0.1 dex at the massive end ($M_* \geq 10^{11} M_\odot$).

To analytically describe the average M_* -versus- $[\text{N II}]/\text{H}\alpha$ relation, we used a functional form originally proposed by Zahid et al. (2014a) to parameterize the mass-metallicity relation,

$$N_2(M_*) = \mathcal{R}_0 - \log \left[1 - \exp \left(\left[\frac{M_*}{\mathcal{M}_0} \right]^\gamma \right) \right], \quad (18)$$

where N_2 denotes $\log [\text{N II}] \lambda 6584/\text{H}\alpha$, \mathcal{R}_0 is the asymptotic value of the line ratio in log scale at the high-mass end, \mathcal{M}_0 is the characteristic mass at which the line ratio begins to saturate,

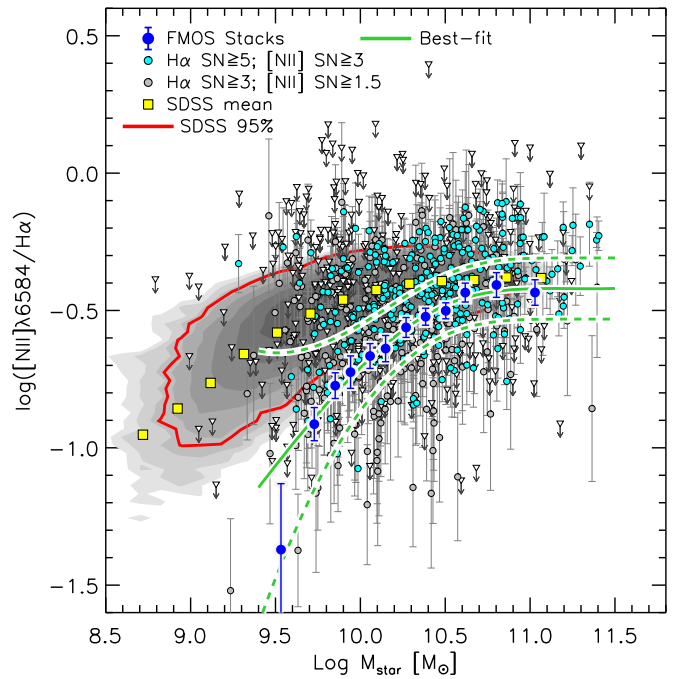


Figure 37. The M_* vs. $[\text{N II}] \lambda 6584/\text{H}\alpha$. The FMOS galaxies in Sample-H are compared with the local SDSS sample. Cyan and gray circles show the HQ ($S/N(\text{H}\alpha) \geq 5$ and $S/N([\text{N II}]) \geq 3$) and LQ ($S/N(\text{H}\alpha) \geq 3$ and $S/N([\text{N II}]) \geq 1.5$) FMOS galaxies. The solid and dashed green curves indicate the best-fit linear relation for the FMOS galaxies with the estimated intrinsic scatter (see Section 11.5).

and γ is the low-mass end slope. The best fit to the stacked line ratios of the FMOS Sample-H takes $\mathcal{R}_0 = -0.42 \pm 0.04$, $\log \mathcal{M}_0/M_\odot = 10.16 \pm 0.09$, and $\gamma = 0.90 \pm 0.14$. The best-fit relation well traces the FMOS stacked points. For the local SDSS sample, we obtained the best-fit parameters of $\mathcal{R}_0 = -0.39$, $\log \mathcal{M}_0/M_\odot = 9.50$, and $\gamma = 0.66$ with the same procedure.

Supposing that the $[\text{N II}]/\text{H}\alpha$ ratio is sensitive to the gas-phase metallicity, the behavior of the stacked points, as well as the best-fit relation, support with higher confidence our past statement that the majority of massive ($M_* \gtrsim 10^{10.6} M_\odot$) galaxies are already chemically mature at $z \sim 1.6$ as much as local galaxies with the same stellar masses (Zahid et al. 2014b; Kashino et al. 2017b). In Figure 37, we also indicate the estimated intrinsic scatter of the FMOS sample around the average best-fit M_* -versus- $[\text{N II}]/\text{H}\alpha$ relation (green dashed lines). Though the derivation of the scatter is described in detail in the next subsection, the sequence is tight for almost the entire M_* range, except the lowest M_* , where the constraint is poor due to the small number of detections. It is seen that the amount of redshift evolution of the average $[\text{N II}]/\text{H}\alpha$ is comparable to twice the intrinsic scatter at $M_* \sim 10^{10} M_\odot$.

11.5. Intrinsic Scatter of the M_* - $[\text{N II}]/\text{H}\alpha$ Relation

Comparing to the local SDSS sample, it seems that the FMOS galaxies show a larger scatter in the $[\text{N II}]/\text{H}\alpha$ ratio at a given M_* . To estimate the intrinsic scatter in the line ratio, we define $\Delta \log [\text{N II}]/\text{H}\alpha$ as the offset of the $[\text{N II}]/\text{H}\alpha$ ratios with respect to $N_2(M_*)$, i.e., the best-fit M_* - $[\text{N II}]/\text{H}\alpha$ relation at a given M_* .

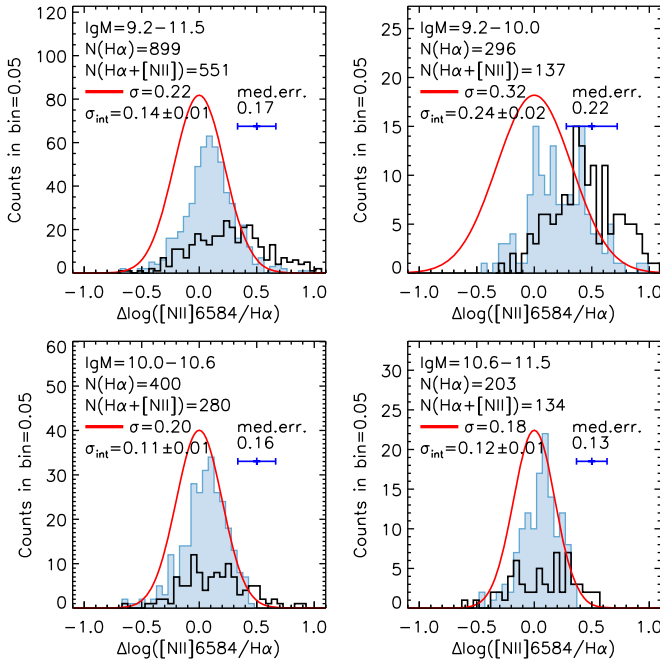


Figure 38. Distribution of the $[\text{N II}] \lambda 6584/\text{H}\alpha$ ratios normalized to the best-fit relation at a given M_* . Objects in the FMOS Sample-H, having both $\text{H}\alpha$ and $[\text{N II}]$ detections, are shown by filled histograms in four ranges of stellar mass: $\log M_*/M_\odot = [9.2:11.5]$ (upper left), $[9.2:10.0]$ (upper right), $[10.0:10.6]$ (lower left), and $[10.6:11.5]$ (lower right). Black open histograms indicate the distribution of upper limits. The numbers of all $\text{H}\alpha$ -detected galaxies (regardless of $[\text{N II}]$ detection; $N(\text{H}\alpha)$) and those with both $\text{H}\alpha$ and $[\text{N II}]$ detections ($N(\text{H}\alpha + [\text{N II}])$) within the mass ranges are given in each panel. The red curve indicates a zero-mean normal function with a broadened standard deviation of $\sigma = \sqrt{\sigma_{\text{int}}^2 + \langle \delta \rangle^2}$. The values of σ , σ_{int} , and the median errors $\langle \delta \rangle$ are given in each panel.

In Figure 38, we show the distribution of the $\Delta \log [\text{N II}]/\text{H}\alpha$ for objects with both $\text{H}\alpha$ and $[\text{N II}]$ detections in different ranges of M_* , as labeled in each panel. The distribution of upper limits for the $[\text{N II}]$ -undetected objects is also shown in each panel. The upper left panel is for almost the entire stellar mass range $10^{9.2} \leq M_*/M_\odot \leq 10^{11.5}$, while the other three panels are for the partial mass bins ($\log M_*/M_\odot = [9.2:10.0]$, $[10.0:10.6]$, and $[10.6:11.5]$). It is clear that the distributions of the $\Delta \log [\text{N II}]/\text{H}\alpha$ values of the $\text{H}\alpha + [\text{N II}]$ -detected objects are skewed toward higher values because the objects with both detections are biased toward having a higher $[\text{N II}]/\text{H}\alpha$ ratio with respect to the best-fit $M_* - [\text{N II}]/\text{H}\alpha$ relation, as seen in Figure 37.

To estimate the true distribution and scatter, we first assumed that the line ratios of all galaxies follow a zero-mean normal distribution with respect to the best-fit $M_* - [\text{N II}]/\text{H}\alpha$ relation. We then estimated the intrinsic scatter in each M_* bin including upper limits. We computed the likelihood $\mathcal{L}(\sigma_{\text{int}})$ for grids of σ_{int} as follows,

$$\mathcal{L}(\sigma_{\text{int}}) \propto \prod_{\text{dec}} F(x_i, \bar{\sigma}_i) \prod_{\text{sup}} (1 - S(c_i, \bar{\sigma}_i)), \quad (19)$$

where x_i and c_i are the detection values and upper limits of $\Delta \log [\text{N II}]/\text{H}\alpha$, respectively. The probability functions F and S are a zero-mean normal distribution function and a zero-mean normal survival function, respectively. The standard deviation $\bar{\sigma}_i$ is computed for each object by summing in quadrature the

uncertainties on $\log [\text{N II}]/\text{H}\alpha$, $\log M_*$, and the intrinsic scatter σ_{int} . The uncertainties on $\log M_*$ were included by multiplying them by the slope of the best-fit $M_* - [\text{N II}]/\text{H}\alpha$ relation at a given M_* .

For the subsamples shown in Figure 38, we obtained a tight constraint on the intrinsic scatter σ_{int} , as indicated in each panel. We found $\sigma_{\text{int}} = 0.14 \pm 0.01$ for the entire M_* range and the largest value ($\sigma_{\text{int}} = 0.24 \pm 0.02$) in the lowest- M_* bin. In the figure, we overplot the normal distribution function (red curves) with a standard deviation convolved with the median error $\langle \delta \rangle$ (including the M_* uncertainties) in each bin (i.e., $\sigma = \sqrt{\sigma_{\text{int}}^2 + \langle \delta \rangle^2}$). These model distribution functions well trace the high-value tail of the histograms of the detected $\log [\text{N II}]/\text{H}\alpha$ values, while there are no upper limits beyond the low-value tail of the model functions. This indicates that our estimates of σ_{int} are robust.

For further investigation of the trend of the intrinsic scatter and comparison with the SDSS galaxies, we repeated the likelihood analysis with narrower overlap binning. In the upper panel of Figure 39, we show the estimated σ_{int} as a function of M_* with the individual $\Delta \log [\text{N II}]/\text{H}\alpha$ values, in comparison with the SDSS sample. For the FMOS and SDSS samples, $\Delta \log [\text{N II}]/\text{H}\alpha$ are computed separately with their own best-fit relation. For the local galaxies, we show the stacked ratios normalized to the best-fit relation and the central 68th percentiles in the M_* bins (black dashed lines). Note that the increase in the scatter due to the individual measurement errors on $[\text{N II}]/\text{H}\alpha$ is negligible ($\lesssim 5\%$) for the SDSS sample. It is clear that the intrinsic scatter of the FMOS galaxies increases with decreasing M_* , while being almost constant $\sigma_{\text{int}} \approx 0.1$ at $M_* \gtrsim 10^{10.3} M_\odot$. A similar trend is seen in the SDSS sample, although the intrinsic scatter of the local sample is smaller than that of the FMOS sample at fixed M_* .

Next, we compare the scatters at fixed $N_2(M_*)$ values, which are taken from the best-fit $M_* - [\text{N II}]/\text{H}\alpha$ relations for the FMOS and SDSS samples, respectively (lower panel in Figure 39). Now the trends of the intrinsic scatter are in rather good agreement between the local and FMOS samples, though the scatter of the FMOS sample is about twice the SDSS sample at the highest $N_2(M_*)$. With respect to this, a caveat is that the local star-forming galaxies are limited to those below the Kauffmann et al. (2003a) division line in the BPT diagram, which is more strict than the maximum starburst limit adopted for the FMOS galaxies, and hence may effectively reduce the scatter, especially at high masses, where the line ratio is nearly saturated.

Comparing the two panels, it seems that the scatter in $[\text{N II}]/\text{H}\alpha$ is more directly related to $N_2(M_*)$ rather than M_* itself, and thus σ_{int} varies more continuously with N_2 across its whole range. We thus parameterized σ_{int} as a function of N_2 by a second-order polynomial,

$$\sigma_{\text{int}} = 0.299 + 0.807N_2(M_*) + 0.856N_2(M_*)^2, \quad (20)$$

which is shown in the lower panel of Figure 39. We used this fit to indicate the estimated intrinsic scatter around the average M_* -versus- $[\text{N II}]/\text{H}\alpha$ relation in Figure 37.

The $[\text{N II}]/\text{H}\alpha$ ratio is known to reflect the gas-phase metallicity of the galaxy (e.g., Pettini & Pagel 2004), though it is also affected by other ISM conditions, such as the ionization parameter, the shape of ionizing spectra (e.g., Kewley et al. 2013), and the intrinsic ratio of N/O (Masters et al. 2014).

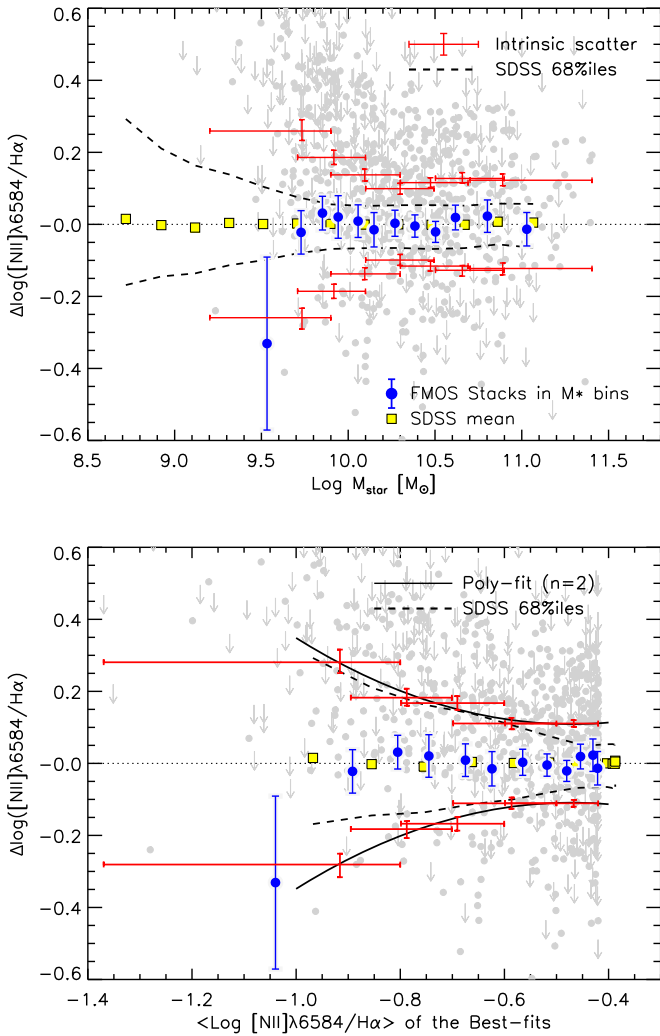


Figure 39. Upper panel: $[\text{N II}]/\text{H}\alpha$ ratio normalized by the best-fit M_* - $[\text{N II}]/\text{H}\alpha$ relation as a function of M_* . The FMOS objects are shown by gray circles and downward arrows (upper limits). Red error bars mark the estimated intrinsic scatter in overlapping M_* bins: the vertical bars indicate the central 68% confidence levels at the median M_* values, and the horizontal bars indicate the widths of the M_* bins. The black dashed lines indicate the central 68th percentiles of the individual SDSS galaxies in bins of M_* . Lower panel: same as upper panel but for $\Delta \log [\text{N II}]/\text{H}\alpha$ as a function of $N_2(M_*)$, i.e., the “best-fit” $[\text{N II}]/\text{H}\alpha$ ratio at given M_* , which is taken from the best-fit relation at a given stellar mass for the FMOS and SDSS samples each. The solid curves indicate a second-order polynomial fit to the σ_{int} estimates of the FMOS sample.

Therefore, interpreting the scatter in $[\text{N II}]/\text{H}\alpha$ as a result of only variation in metallicity may lead to inaccurate insights. However, our result likely indicates that there is not a large difference in the amount of metallicity variation at fixed average metallicity between the local SDSS and $z \sim 1.6$ FMOS samples. We note that the physical time across the redshift range of the FMOS sample ($1.43 \leq z \leq 1.74$; 0.69 Gyr) is similar to that of the local sample ($0.04 \leq z \leq 0.10$; 0.76 Gyr). Therefore, the effects of the time evolution of metallicity within the redshift ranges of the two samples should be small.

12. Comparison between $\text{H}\alpha$ and $[\text{O III}]$ Emitters

The $[\text{O III}] \lambda 5007$ emission line is one of the strongest lines in the rest-frame optical window, being comparable to $\text{H}\alpha$. Therefore, it has been used as a tracer of galaxies (Khostovan et al. 2015; Suzuki et al. 2015). Meanwhile, it is well known

Table 11
Summary of the Subsamples Used in Section 12

Subsamples	N	Note
$\text{H}\alpha$ emitters	682	$\text{H}\alpha$ ($\geq 3\sigma$) and $[\text{O III}]$ coverage
$\text{H}\alpha$ single emitters	439	$\text{H}\alpha$ emitters with no $[\text{O III}]$ detection ^a
$[\text{O III}]$ emitters	270	$[\text{O III}]$ ($\geq 3\sigma$) and $\text{H}\alpha$ coverage
$[\text{O III}]$ single emitters	27	$[\text{O III}]$ emitters with no $\text{H}\alpha$ detection ^a
$\text{H}\alpha$ + $[\text{O III}]$ emitters	243	Both $\text{H}\alpha$ and $[\text{O III}]$ detections ($\geq 3\sigma$)

Note.

^a These two single-emitter samples have spectral coverage for the other emission line. Detections at $1.5 \leq S/N < 3$ are regarded as nondetections throughout this section.

that the intensity of the $[\text{O III}]$ line is sensitive to metallicity at a fixed SFR, as well as more affected by dust extinction than $\text{H}\alpha$. Suzuki et al. (2016) compared the narrowband selected $\text{H}\alpha$ - and $[\text{O III}]$ -emitter samples at $z \sim 2$ and argued that the $[\text{O III}]$ emitters trace almost the same galaxy populations as the $\text{H}\alpha$ emitters. However, the contamination of the remaining AGNs would be not negligible, since there is no way to see the BPT line ratios (i.e., $[\text{N II}]/\text{H}\alpha$ and $[\text{O III}]/\text{H}\beta$) and line profiles with their narrowband observations. Moreover, the contamination of $\text{H}\beta$ emitters misidentified as $[\text{O III}]$ emitters with no $\text{H}\alpha$ detection may lead to inaccurate results. We thus use our FMOS sample to study the population of $[\text{O III}]$ -emitting galaxies in comparison with the $\text{H}\alpha$ -emitting sources and examine their claims.

For our purposes, we define the subsamples of $z \sim 1.6$ galaxies as listed in Table 11. These objects are limited to having secure estimates of M_* and $E_{\text{star}}(B - V)$ (Section 9), and X-ray objects and possible AGNs were excluded in the same way as in Section 10. The $\text{H}\alpha$ -emitter sample contains 682 objects with detection of $\text{H}\alpha$ at $\geq 3\sigma$ and the J -long coverage of the $[\text{O III}]$ emission line (i.e., we have either detection or an estimate of the upper limit of $[\text{O III}]$). Of these, we detected the $[\text{O III}]$ line at $\geq 3\sigma$ for 243 objects, which are referred to as the $\text{H}\alpha$ + $[\text{O III}]$ -emitter sample. The detection failed for the remaining 439 objects ($< 3\sigma$ or upper limit on $[\text{O III}]$ flux), which are categorized as $\text{H}\alpha$ single emitters. We also defined the $[\text{O III}]$ -emitter sample containing 270 objects with a detection of $[\text{O III}]$ ($\geq 3\sigma$) and the H -long coverage and the $[\text{O III}]$ single-emitter ($< 3\sigma$ or upper limit on $\text{H}\alpha$) sample of 27 objects.

12.1. $[\text{O III}]$ Flux versus $\text{H}\alpha$ Flux

In Figure 40, we show the correlation between the $\text{H}\alpha$ and $[\text{O III}] \lambda 5007$ fluxes after correcting for dust extinction and aperture loss. Extinction correction is applied by assuming the Cardelli et al. (1989) extinction law with $f_{\text{neb}} = 0.53$ (Section 9.3). Limiting the $\text{H}\alpha$ + $[\text{O III}]$ -emitter sample, a strong correlation and good agreement exist between these quantities. We found the Spearman’s rank correlation coefficient to be $\rho = 0.63$, excluding the null hypothesis of no correlation. The scatter of $\log [\text{O III}]/\text{H}\alpha$ is found to be 0.28 dex with a small median offset of $\log [\text{O III}]/\text{H}\alpha = -0.004$.

The $[\text{O III}]/\text{H}\alpha$ ratio is expected to depend on stellar mass because metallicity and dust extinction increase, on average, with M_* . In Figure 41, we show the dust-corrected (aperture as well) $[\text{O III}]/\text{H}\alpha$ ratio as a function of M_* for the subsamples. Limiting to the $\text{H}\alpha$ + $[\text{O III}]$ emitters, it is clear that the line ratio

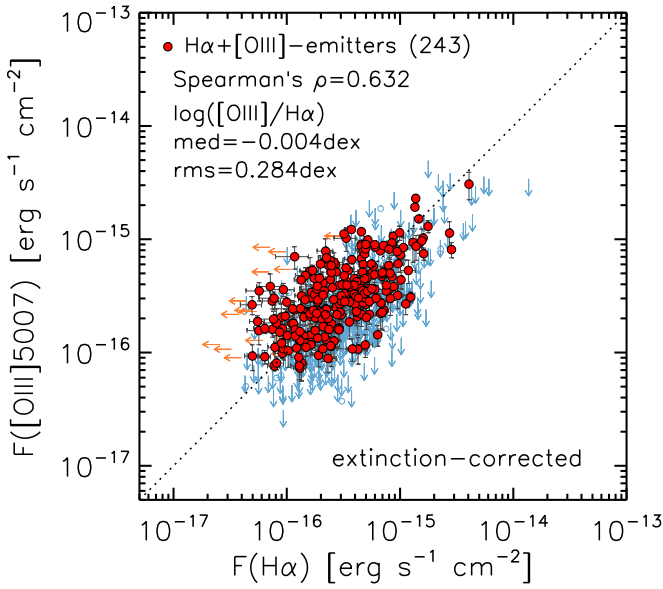


Figure 40. Correlation between $H\alpha$ and $[O\text{ III}]\lambda 5007$ fluxes after correcting for dust extinction (both corrected for aperture loss). Red circles indicate 243 objects in the $H\alpha$ + $[O\text{ III}]$ -emitter sample ($H\alpha$ at $\geq 3\sigma$ and $[O\text{ III}]$ at $\geq 3\sigma$). The $H\alpha$ single emitters are shown with blue circles ($1.5 \leq S/N([O\text{ III}]) < 3$) or downward arrows (2σ upper limits). The $[O\text{ III}]$ single emitters are shown with orange circles ($1.5 \leq S/N(H\alpha) < 3$) or leftward arrows (2σ upper limits). The dotted line indicates a one-to-one relation.

decreases with increasing M_* , and that at high M_* ($> 10^{10.5} M_\odot$), the majority of the $H\alpha$ -detected objects have no significant detection of the $[O\text{ III}]$ line. We note that the extinction-corrected $[O\text{ III}]/H\alpha$ ratio has essentially the same information as the $[O\text{ III}]/H\beta$ ratio (i.e., Figure 36).

12.2. Comparison of the Subsamples

The lack of $[O\text{ III}]$ detection at high M_* indicates possible biases that exist between the $H\alpha$ - and $[O\text{ III}]$ -selected populations. The $[O\text{ III}]$ flux decreases more rapidly with increasing metallicity and the level of dust extinction; thus, the $[O\text{ III}]/H\alpha$ ratio depends significantly on these properties. To indicate biases between the $H\alpha$ - and $[O\text{ III}]$ -emitter subsamples, we separate the objects into different M_* bins and compute the fraction of objects with $[O\text{ III}]$ detection in each bin. We then compare the distribution of the observed $H\alpha$ and $[O\text{ III}]$ fluxes between the subsamples in each bin. In Figure 42, we show the distribution of the aperture-corrected $H\alpha$ fluxes (not corrected for dust) for the $H\alpha$ - and $H\alpha$ + $[O\text{ III}]$ -emitter samples in four bins of stellar mass ($\log M_*/M_\odot < 9.9$, $9.9 \leq \log M_*/M_\odot < 10.3$, $10.3 \leq \log M_*/M_\odot < 10.7$, and $\log M_*/M_\odot \geq 10.7$). For the $H\alpha$ + $[O\text{ III}]$ -emitter sample, we also plot the distribution of observed $[O\text{ III}]$ fluxes. In each panel, we give the number of objects in the $H\alpha$ - and $H\alpha$ + $[O\text{ III}]$ -emitter samples, as well as the median values of the observed $H\alpha$ and $[O\text{ III}]$ fluxes in log scale in units of $10^{-17} \text{ erg s}^{-1} \text{ cm}^{-2}$.

In the lowest- M_* bin (upper left panel in Figure 42), we detected the $[O\text{ III}]$ line ($\geq 3\sigma$) for more than half (55%) the $H\alpha$ -emitter sample. The median $H\alpha$ fluxes of the $H\alpha$ - and $H\alpha$ + $[O\text{ III}]$ -emitter samples are similar to each other. At higher M_* bins, however, the fraction of $H\alpha$ + $[O\text{ III}]$ emitters is lower: 39%, 27%, and 9% in the second, third, and fourth bins, respectively. It is also clear that a difference becomes apparent

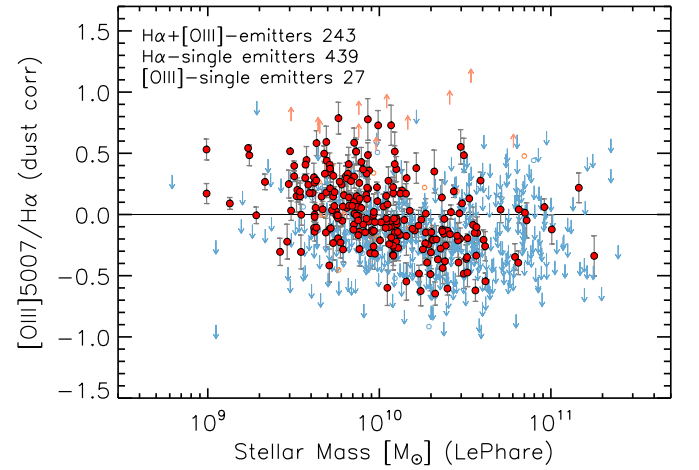


Figure 41. Dust-corrected $[O\text{ III}]\lambda 5007/H\alpha$ ratio as a function of M_* . Red circles indicate 261 objects in the $H\alpha$ + $[O\text{ III}]$ -emitter sample ($H\alpha$ at $\geq 3\sigma$ and $[O\text{ III}]$ at $\geq 1.5\sigma$), and downward arrows indicate the upper limits for 416 $H\alpha$ single emitters ($\geq 3\sigma$, but only upper limits on the $[O\text{ III}]$ flux).

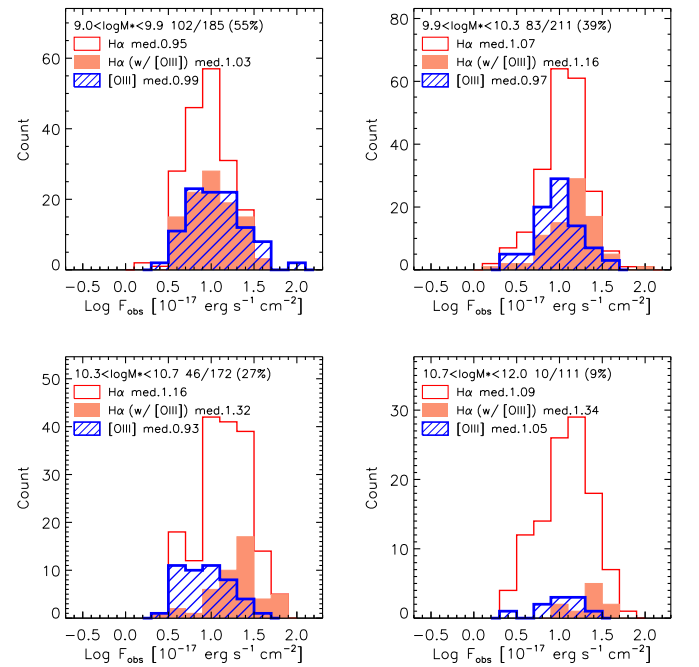


Figure 42. Distribution of $H\alpha$ and $[O\text{ III}]\lambda 5007$ fluxes (corrected for aperture loss but not for dust extinction) in different bins of M_* - $\log M_*/M_\odot = [9.0:9.9]$ (upper left), $[9.9:10.3]$ (upper right), $[10.3:10.7]$ (lower left), and ≥ 10.7 (lower right). Open histograms indicate the $F_{H\alpha}$ distribution for the $H\alpha$ emitters. Red filled and blue hatched histograms indicate distributions of $H\alpha$ and $[O\text{ III}]\lambda 5007$ fluxes, respectively, for the $H\alpha$ + $[O\text{ III}]$ -emitter sample. In each panel, we give the number of $H\alpha$ and $H\alpha$ + $[O\text{ III}]$ emitters (e.g., in the upper left panel, the numbers of $H\alpha$ and $H\alpha$ + $[O\text{ III}]$ emitters within the bin are 185 and 102 (55%), respectively), as well as the median values of the observed $H\alpha$ and $[O\text{ III}]$ fluxes in log scale in units of $10^{-17} \text{ erg s}^{-1} \text{ cm}^{-2}$.

between the median $H\alpha$ fluxes of the $H\alpha$ - and $H\alpha$ + $[O\text{ III}]$ -emitter samples: the $H\alpha$ + $[O\text{ III}]$ emitters are biased toward higher $H\alpha$ flux.

For further insights, we separate the sample into bins of the level of extinction $E_{\text{star}}(B-V)$ estimated from the UV slope (see Section 9.2). In Figure 43, we show the distribution of observed fluxes in four $E_{\text{star}}(B-V)$ bins ($0 \leq \log E_{\text{star}}(B-V) < 0.16$, $0.16 \leq \log E_{\text{star}}(B-V) < 0.23$, $0.23 \leq \log E_{\text{star}}(B-V) < 0.35$, and

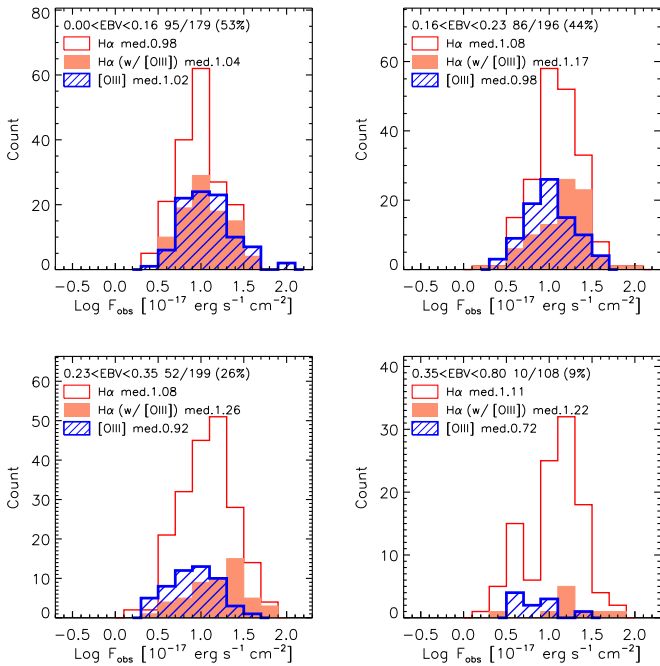


Figure 43. Same as Figure 42 but in bins of extinction: $E_{\text{star}}(B - V) = [0.0:0.16]$ (upper left), $[0.16:0.23]$ (upper right), $[0.23:0.35]$ (lower left), and ≥ 0.35 (lower right).

$E_{\text{star}}(B - V) \geq 0.35$). It is evident that, similar to the trend with M_* , the fraction of $\text{H}\alpha + [\text{O III}]$ emitters decreases with increasing extinction value, from 53% in the lowest bin to 9% in the highest bin.

Our results clearly indicate that the $[\text{O III}]$ emission line traces more preferentially lower M_* galaxies and/or objects less obscured by dust. We note that there is a strong correlation between M_* and $E_{\text{star}}(B - V)$ (Figure 28). In less massive galaxies, the higher $[\text{O III}]$ fluxes are associated with lower metallicities. We thus conclude that the use of $[\text{O III}]$ for the FMOS-COSMOS sample comes with biases toward lower M_* , lower metallicity, and/or less obscured populations than those traced by $\text{H}\alpha$ at the same flux limit. Even so, the $[\text{O III}]$ emission line is a powerful tool for galaxy surveys at high redshifts, since low-mass and low-metallicity galaxies may be a dominant population in the early universe.

Note that the $[\text{O III}]$ - and $[\text{O III}]$ -single-emitter samples are not purely selected by the $[\text{O III}]$ line because we included the criterion on the predicted $\text{H}\alpha$ flux in the preselection of the spectroscopic targets to achieve a high success rate of detecting $\text{H}\alpha$. Indeed, the majority of the $[\text{O III}]$ -emitter sample has a detection of $\text{H}\alpha$; thus, there are a small number of $[\text{O III}]$ single emitters in our FMOS catalog. We do not see any significant trends in either the $\text{H}\alpha$ -detection fraction or the average $[\text{O III}]$ flux of the $\text{H}\alpha + [\text{O III}]$ emitters relative to the $[\text{O III}]$ emitters.

13. Summary

In this paper, we presented our analyses of near-IR spectra collected through the FMOS-COSMOS survey and the basic properties of spectroscopic measurements of star-forming galaxies based on the full catalog that contains 5427 galaxies. The full FMOS-COSMOS catalog contains spectroscopic measurements of redshift and line fluxes for 1931 objects, including 1204 $\text{H}\alpha$ detections at 3σ at $1.43 \leq z \leq 1.74$, down

to the in-fiber flux limit of about $\sim 1 \times 10^{-17} \text{ erg cm}^{-2} \text{ s}^{-1}$. The full sample combines the main population of star-forming galaxies along the main sequence at $z \sim 1.6$ with the stellar mass range of $9.5 \lesssim \log M_*/M_\odot \lesssim 11.5$ and other specific subsamples of infrared-luminous galaxies at $z \sim 0.9$ and 1.6 and *Chandra* X-ray sources. The success rate of the spectroscopic measurement achieves 43% for the primary sample (Section 5.2). The full version of the catalog is publicly available online (see Section 5).

The precision of the redshift measurement is estimated to be $\approx 70 \text{ km s}^{-1}$ in standard deviation (Section 7). Compared to other spectroscopic campaigns, the probability of line misidentification is expected to be less than 10% for $z_{\text{Flag}} \geq 2$. For all objects, we estimated the correction factor for the aperture loss of the observed fluxes. The typical uncertainty in the absolute flux calibration, including aperture correction, is found to be $\approx 0.17 \text{ dex}$. We found that our total aperture-corrected flux measurements are in excellent agreement with the slitless measurements from the 3D-*HST* survey (Section 7).

We used the latest sample to update our past analyses. The enhancement of the extinction toward nebular emission was measured from comparisons between $\text{H}\alpha$ - and UV-based dust-uncorrected SFRs. We found that $f_{\text{neb}} = E_{\text{star}}(B - V)/E_{\text{neb}}(B - V) = 0.53$, which is consistent with our previous result in Kashino et al. (2013) after taking into account the difference of the extinction laws applied (Section 9.3).

In Section 10, the M_* -SFR relation was remeasured using the recomputed stellar masses (based on z_{spec}) and dust-corrected $\text{H}\alpha$ luminosities. The result is in good agreement with an analytical form derived from a compilation of measurements across a wide redshift range. We found that the data are better fit with a parameterization invoking a bending feature of the sequence with a characteristic mass $M_* \approx 10^{10.2} M_\odot$. The estimated scatter in the $\text{H}\alpha$ -based SFRs with respect to the best-fit M_* -SFR relation is found to increase with increasing M_* , though the sample selection including a limit on the predicted $\text{H}\alpha$ fluxes may result in a reduction of the scatter of the spectroscopic sample.

In Section 11, we updated the emission-line diagnostic diagrams and especially found a significant offset in the S2-BPT ($[\text{S II}]/\text{H}\alpha$ versus $[\text{O III}]/\text{H}\beta$) diagram relative to low- z galaxies, as originally reported in our previous study. With this observational feature, we confirmed with higher confidence that the ionization parameter increases in high-redshift star-forming galaxies relative to low- z objects. We redefined the M_* - $[\text{N II}]/\text{H}\alpha$ relation and confirmed that the massive ($\geq 10^{10.6} M_\odot$) galaxies have a level of the line ratio, i.e., the gas-phase metallicity, similar to that of the local galaxies with the same masses. Furthermore, we evaluated the intrinsic scatter of the M_* -versus- $[\text{N II}]/\text{H}\alpha$ relation and found that the scatter is small ($\approx 0.1 \text{ dex}$) at high M_* (or high $[\text{N II}]/\text{H}\alpha$) while increasing to ≈ 0.3 at low M_* (or low $[\text{N II}]/\text{H}\alpha$). The behavior of the intrinsic scatter is similar to that of the local galaxies when comparing them as a function of the average $[\text{N II}]/\text{H}\alpha$ ratio at a given M_* .

Comparing subsamples of $\text{H}\alpha$ and $[\text{O III}]$ emitters, we found that there is little bias in the observed $\text{H}\alpha$ line flux between the $\text{H}\alpha$ single and $\text{H}\alpha + [\text{O III}]$ -detected samples at low masses and/or low extinction ($\lesssim 10^{10} M_\odot$, $E_{\text{star}}(B - V) \lesssim 0.2$). In contrast, it has been shown that, at higher masses/extinction,

the detection of [O III] becomes more biased toward a population having higher H α fluxes (Section 12).

To conclude, our large spectroscopic survey has established a large (on the order of 10^3) sample of star-forming galaxies at $1.4 < z < 1.7$, fully filling the redshift desert. Combining with the rich panchromatic resources in the COSMOS field, the FMOS-COSMOS catalog offers the means to comprehensively learn how galaxies evolve across the cosmic noon era, as well as to elaborate survey strategies with a new generation of multifiber spectrographs, such as MOONS or the Prime Focus Spectrograph.

We are grateful to the referee for careful reading and useful comments; the Subaru telescope staff, especially K. Aoki, for their expertise in the observations; H. J. Zahid for providing data for target selection; and the MPA/JHU team for making their catalog public. This paper is based on data collected at the Subaru Telescope, which is operated by the National Astronomical Observatory of Japan. This work was supported in part by KAKENHI (DK 14J03216; JDS 26400221) through the Japan Society for the Promotion of Science (JSPS), the World Premier International Research Center Initiative (WPI), MEXT, Japan. G.R. and A.R. acknowledge support via grant INAF PRIN-SKA 2017. N.A. is supported by the Brain Pool Program, which is funded by the Ministry of Science and ICT through the National Research Foundation of Korea (2018H1D3A2000902).

Facility: Subaru (FMOS).

ORCID iDs

Daichi Kashino  <https://orcid.org/0000-0001-9044-1747>
 John D. Silverman  <https://orcid.org/0000-0002-0000-6977>
 David Sanders  <https://orcid.org/0000-0002-1233-9998>
 Jeyhan Kartaltepe  <https://orcid.org/0000-0001-9187-3605>
 Emanuele Daddi  <https://orcid.org/0000-0002-3331-9590>
 Alvio Renzini  <https://orcid.org/0000-0002-7093-7355>
 Giulia Rodighiero  <https://orcid.org/0000-0002-9415-2296>
 Annagrazia Puglisi  <https://orcid.org/0000-0001-9369-1805>
 Francesco Valentino  <https://orcid.org/0000-0001-6477-4011>
 Stéphanie Juneau  <https://orcid.org/0000-0002-0000-2394>
 Tohru Nagao  <https://orcid.org/0000-0002-7402-5441>
 Olivier Ilbert  <https://orcid.org/0000-0002-7303-4397>
 Olivier Le Fèvre  <https://orcid.org/0000-0001-5891-2596>
 Anton M. Koekemoer  <https://orcid.org/0000-0002-6610-2048>

References

- Arnouts, S., Moscardini, L., Vanzella, E., et al. 2002, *MNRAS*, **329**, 355
 Baldwin, J. A., Phillips, M. M., & Terlevich, R. 1981, *PASP*, **93**, 5
 Berta, S., Lutz, D., Santini, P., et al. 2013, *A&A*, **551**, A100
 Bertin, E., & Arnouts, S. 1996, *A&AS*, **117**, 393
 Brammer, G. B., van Dokkum, P. G., Franx, M., et al. 2012, *ApJS*, **200**, 13
 Brinchmann, J., Charlot, S., White, S. D. M., et al. 2004, *MNRAS*, **351**, 1151
 Bruzual, G., & Charlot, S. 2003, *MNRAS*, **344**, 1000
 Calzetti, D., Armus, L., Bohlin, R. C., et al. 2000, *ApJ*, **533**, 682
 Capak, P., Aussel, H., Ajiki, M., et al. 2007, *ApJS*, **172**, 99
 Cardelli, J. A., Clayton, G. C., & Mathis, J. S. 1989, *ApJ*, **345**, 245
 Chabrier, G. 2003, *PASP*, **115**, 763
 Civano, F., Marchesi, S., Comastri, A., et al. 2016, *ApJ*, **819**, 62
 Coil, A. L., Aird, J., Reddy, N., et al. 2015, *ApJ*, **801**, 35
 da Cunha, E., Charlot, S., & Elbaz, D. 2008, *MNRAS*, **388**, 1595
 Daddi, E., Cimatti, A., Renzini, A., et al. 2004, *ApJ*, **617**, 746
 Elvis, M., Civano, F., Vignali, C., et al. 2009, *ApJS*, **184**, 158
 Fitzpatrick, E. L. 1999, *PASP*, **111**, 63
 Grogan, N. A., Kocevski, D. D., Faber, S. M., et al. 2011, *ApJS*, **197**, 35
 Harrison, C. M., Alexander, D. M., Mullaney, J. R., et al. 2016, *MNRAS*, **456**, 1195
 Ilbert, O., Arnouts, S., Le Floc'h, E., et al. 2015, *A&A*, **579**, A2
 Ilbert, O., Arnouts, S., McCracken, H. J., et al. 2006, *A&A*, **457**, 841
 Ilbert, O., McCracken, H. J., Le Fèvre, O., et al. 2013, *A&A*, **556**, A55
 Ilbert, O., Salvato, M., Le Floc'h, E., et al. 2010, *ApJ*, **709**, 644
 Iwamuro, F., Moritani, Y., Yabe, K., et al. 2012, *PASJ*, **64**, 59
 Juneau, S., Bournaud, F., Charlot, S., et al. 2014, *ApJ*, **788**, 88
 Juneau, S., Dickinson, M., Alexander, D. M., & Salim, S. 2011, *ApJ*, **736**, 104
 Kaasinen, M., Bian, F., Groves, B., Kewley, L. J., & Gupta, A. 2017, *MNRAS*, **465**, 3220
 Kaasinen, M., Kewley, L., Bian, F., et al. 2018, *MNRAS*, **477**, 5568
 Karim, A., Schinnerer, E., Martínez-Sansigre, A., et al. 2011, *ApJ*, **730**, 61
 Kartaltepe, J. S., Sanders, D. B., Silverman, J. D., et al. 2015, *ApJL*, **806**, L35
 Kashino, D., & Inoue, A. K. 2018, arXiv:1812.06939
 Kashino, D., More, S., Silverman, J. D., et al. 2017a, *ApJ*, **843**, 138
 Kashino, D., Silverman, J. D., Rodighiero, G., et al. 2013, *ApJL*, **777**, L8
 Kashino, D., Silverman, J. D., Sanders, D., et al. 2017b, *ApJ*, **835**, 88
 Kauffmann, G., Heckman, T. M., Tremonti, C., et al. 2003a, *MNRAS*, **346**, 1055
 Kauffmann, G., Heckman, T. M., White, S. D. M., et al. 2003b, *MNRAS*, **341**, 33
 Kennicutt, R. C., Jr. 1998, *ARA&A*, **36**, 189
 Kewley, L. J., Dopita, M. A., Leitherer, C., et al. 2013, *ApJ*, **774**, 100
 Kewley, L. J., Dopita, M. A., Sutherland, R. S., Heisler, C. A., & Trevena, J. 2001, *ApJ*, **556**, 121
 Khostovan, A. A., Sobral, D., Mobasher, B., et al. 2015, *MNRAS*, **452**, 3948
 Kimura, M., Maihara, T., Iwamuro, F., et al. 2010, *PASJ*, **62**, 1135
 Koekemoer, A. M., Aussel, H., Calzetti, D., et al. 2007, *ApJS*, **172**, 196
 Koekemoer, A. M., Faber, S. M., Ferguson, H. C., et al. 2011, *ApJS*, **197**, 36
 Kriek, M., Shapley, A. E., Reddy, N. A., et al. 2015, *ApJS*, **218**, 15
 Laigle, C., McCracken, H. J., Ilbert, O., et al. 2016, *ApJS*, **224**, 24
 Lee, N., Sanders, D. B., Casey, C. M., et al. 2015, *ApJ*, **801**, 80
 Le Fèvre, O., Tasca, L. A. M., Cassata, P., et al. 2015, *A&A*, **576**, A79
 Lilly, S. J., Le Fèvre, O., Renzini, A., et al. 2007, *ApJS*, **172**, 70
 Lutz, D., Poglitsch, A., Altieri, B., et al. 2011, *A&A*, **532**, A90
 Markwardt, C. B. 2009, in ASP Conf. Ser. 411, *Astronomical Data Analysis Software and Systems XVIII*, ed. D. A. Bohlender, D. Durand, & P. Dowler (San Francisco, CA: ASP), 251
 Massey, R., Stoughton, C., Leauthaud, A., et al. 2010, *MNRAS*, **401**, 371
 Masters, D., & Capak, P. 2011, *PASP*, **123**, 638
 Masters, D., McCarthy, P., Siana, B., et al. 2014, *ApJ*, **785**, 153
 Matsuoka, K., Silverman, J. D., Schramm, M., et al. 2013, *ApJ*, **771**, 64
 McCracken, H. J., Capak, P., Salvato, M., et al. 2010, *ApJ*, **708**, 202
 McCracken, H. J., Milvang-Jensen, B., Dunlop, J., et al. 2012, *A&A*, **544**, A156
 Meurer, G. R., Heckman, T. M., & Calzetti, D. 1999, *ApJ*, **521**, 64
 Momcheva, I. G., Brammer, G. B., van Dokkum, P. G., et al. 2016, *ApJS*, **225**, 27
 Noeske, K. G., Weiner, B. J., Faber, S. M., et al. 2007, *ApJL*, **660**, L43
 Oliver, S. J., Bock, J., Altieri, B., et al. 2012, *MNRAS*, **424**, 1614
 Pettini, M., & Pagel, B. E. J. 2004, *MNRAS*, **348**, L59
 Price, S. H., Kriek, M., Brammer, G. B., et al. 2014, *ApJ*, **788**, 86
 Puglisi, A., Daddi, E., Renzini, A., et al. 2017, *ApJL*, **838**, L18
 Rodighiero, G., Daddi, E., Baronchelli, I., et al. 2011, *ApJL*, **739**, L40
 Rodighiero, G., Renzini, A., Daddi, E., et al. 2014, *MNRAS*, **443**, 19
 Salim, S., Rich, R. M., Charlot, S., et al. 2007, *ApJS*, **173**, 267
 Salmi, F., Daddi, E., Elbaz, D., et al. 2012, *ApJL*, **754**, L14
 Salpeter, E. E. 1955, *ApJ*, **121**, 161
 Salvato, M., Ilbert, O., Hasinger, G., et al. 2011, *ApJ*, **742**, 61
 Sanders, D. B., & Mirabel, I. F. 1996, *ARA&A*, **34**, 749
 Sanders, D. B., Salvato, M., Aussel, H., et al. 2007, *ApJS*, **172**, 86
 Schreiber, C., Pannella, M., Elbaz, D., et al. 2015, *A&A*, **575**, A74
 Schulze, A., Silverman, J. D., Kashino, D., et al. 2018, *ApJS*, **239**, 22
 Shapley, A. E., Reddy, N. A., Kriek, M., et al. 2015, *ApJ*, **801**, 88
 Silverman, J., Daddi, E., Rujopakarn, W., et al. 2018a, *ApJ*, **868**, 75
 Silverman, J., Rujopakarn, W., Daddi, E., et al. 2018b, *ApJ*, **867**, 92
 Silverman, J. D., Daddi, E., Rodighiero, G., et al. 2015a, *ApJL*, **812**, L23
 Silverman, J. D., Kashino, D., Sanders, D., et al. 2015b, *ApJS*, **220**, 12
 Skelton, R. E., Whitaker, K. E., Momcheva, I. G., et al. 2014, *ApJS*, **214**, 24
 Speagle, J. S., Steinhart, C. L., Capak, P. L., & Silverman, J. D. 2014, *ApJS*, **214**, 15
 Steidel, C. C., Rudie, G. C., Strom, A. L., et al. 2014, *ApJ*, **795**, 165
 Storey, P. J., & Zeppen, C. J. 2000, *MNRAS*, **312**, 813
 Strom, A. L., Steidel, C. C., Rudie, G. C., et al. 2017, *ApJ*, **836**, 164

Suzuki, T. L., Kodama, T., Sobral, D., et al. 2016, [MNRAS](#), 462, 181
Suzuki, T. L., Kodama, T., Tadaki, K.-i., et al. 2015, [ApJ](#), 806, 208
Valentino, F., Daddi, E., Silverman, J. D., et al. 2017, [MNRAS](#), 472, 4878
Veilleux, S., & Osterbrock, D. E. 1987, [ApJS](#), 63, 295

Whitaker, K. E., Franx, M., Leja, J., et al. 2014, [ApJ](#), 795, 104
Wisnioski, E., Förster Schreiber, N. M., Wuyts, S., et al. 2015, [ApJ](#), 799, 209
Zahid, H. J., Dima, G. I., Kudritzki, R.-P., et al. 2014a, [ApJ](#), 791, 130
Zahid, H. J., Kashino, D., Silverman, J. D., et al. 2014b, [ApJ](#), 792, 75